Argonne
NATIONAL LABORATORY

ANL-07/24

A Physical Description of Fission Product Behavior in Fuels for Advanced Power Reactors

Nuclear Engineering Division

About Argonne National Laboratory

Argonne is a U.S. Department of Energy laboratory managed by UChicago Argonne, LLC under contract DE-AC02-06CH11357. The Laboratory's main facility is outside Chicago, at 9700 South Cass Avenue, Argonne, Illinois 60439. For information about Argonne, see www.anl.gov.

Availability of This Report

This report is available, at no cost, at http://www.osti.gov/bridge. It is also available on paper to the U.S. Department of Energy and its contractors, for a processing fee, from:

U.S. Department of Energy
Office of Scientific and Technical Information
P.O. Box 62
Oak Ridge, TN 37831-0062
phone (865) 576-8401
fax (865) 576-5728
reports@adonis.osti.gov

ANL-07/24

A Physical Description of Fission Product Behavior in Fuels for Advanced Power Reactors

by
G. Kagana
Florida International Univeristy

J. Rest
Nuclear Engineering Division, Argonne National Laboratory

September 4, 2007

A physical description of fission product behavior in fuels for advanced power reactors

G. Kaganas[1], J. Rest[2]

September 4, 2007

[1]Argonne National Laboratory, Summer Internship, 2007
[2]Argonne National Laboratory, Nuclear Engineering 208, 9700 S. Cass Avenue, Argonne, IL 60439, USA

Contents

List of Figures

List of Tables

Abstract

The Global Nuclear Energy Partnership (GNEP) is considering a list of reactors and nuclear fuels as part of its chartered initiative. Because many of the candidate materials have not been explored experimentally under the conditions of interest, and in order to economize on program costs, analytical support in the form of combined first principle and mechanistic modeling is highly desirable. The present work is a compilation of mechanistic models developed in order to describe the fission product behavior of irradiated nuclear fuel. The mechanistic nature of the model development allows for the possibility of describing a range of nuclear fuels under varying operating conditions. Key sources include the *FASTGRASS* code with an application to UO_2 power reactor fuel and the Dispersion Analysis Research Tool (*DART*) with an application to uranium-silicide and uranium-molybdenum research reactor fuel. Described behavior mechanisms are divided into subdivisions treating fundamental materials processes under normal operation as well as the effect of transient heating conditions on these processes. Model topics discussed include intra- and intergranular gas-atom and bubble diffusion, bubble nucleation and growth, gas-atom re-solution, fuel swelling and fission gas release. In addition, the effect of an evolving microstructure on these processes (e.g., irradiation-induced recrystallization) is considered. The uranium-alloy fuel, U-xPu-Zr, is investigated and behavior mechanisms are proposed for swelling in the α-, intermediate- and γ-uranium zones of this fuel. The work reviews the *FASTGRASS* kinetic/mechanistic description of volatile fission products and, separately, the basis for the *DART* calculation of bubble behavior in amorphous fuels. Development areas and applications for physical nuclear fuel models are identified.

Chapter 1

Introduction

A controlled nuclear reaction, such as is witnessed daily within a power reactor, is a highly complex interaction. Within this active medium, energy is constantly being transferred by one incident event into several linked mechanisms, which, due to the nature and relative proximity of these reactions within a compact fuel element, tend to continually influence the original reaction.

This cyclical, or coupled, aspect of nuclear reactions is one of the many difficulties facing the researcher. One of the biggest challenges, however, lies in the proper interpretation of the observed data. In a system rich in variation, proposing a particular mechanism to describe a hypothesized behavior can be trying.

In the field of fuel performance modeling, this difficulty is often surmounted by employing the use of empirical models. This modeling approach is less concerned with the physical interpretation of what is being observed, but rather attempts to model the mathematical variation of the system. Thus by careful consideration of the data and by constant manipulation of the input parameters, a numerical, predictive code is arrived at. Although these models may accurately predict the run of an experiment, they are only effective in a narrow set of situations. Being tied to the data, as opposed to the underlying physical processes, minor changes introduced to the experiment may have significant consequences on the reliability of the model.

Ideally, a descriptive model should exist completely independent of any one set of data. In this model, its predictive faculties are entirely grounded on the physical interpretation of phenomena it attempts to describe. Often there are hundreds of simultaneous processes that form the shape of the experimental data. That is why the modeler must judiciously select the key forces that dominate a particular process.

This highly intellectual, if not intuitive, process places very high demands on the modeler. It is therefore not a surprise that there is an overabundance of highly-specific empirical models, while the more robust physical, or analytical, models are much less common.

Jeffrey Rest is at the forefront of a handful of researchers who employ their research efforts in understanding the physical underpinnings that define nuclear fuel behavior. In his more than 30 years in the field, his work has served to illuminate some of the more subtle processes that govern nuclear fuel behavior under irradiation.

At the nucleus of Rest's work is a consistent interpretation of fission product behavior. A discussion of fission product behavior in nuclear fuels is vital to an accurate description of fuel performance under irradiation. A complete understanding of these mechanisms necessarily requires investigation into other aspects of the fuel element such as the materials properties of the fuel and its changing crystal microstructure under varying conditions, the chemical kinetics of the fission products, the role of bubble nucleation and coalescence, etc. The complexity of the model, while difficult to synthesize, provides the important advantage of offering a physically based theory of the behavior of nuclear fuels in fission reactions.

1.1 Purpose

This report constitutes a compilation of the major theories developed and organized by Jeffrey Rest. (From this point forward, these works will be referred to as the Rest Models.) This collection is a response to the rising need of broad-ranging predictive nuclear fuel behavior models that can be used to evaluate fuel performance. Complete, up to date models that can be adapted to evaluate the performance of a number of fuels under a range of operating conditions are scarce, primarily, due to the absence of analytical, physically based theories, as explained above.

The models included in this work have been used to describe the fission-product behavior of uranium-oxide fuels and uranium-silicide dispersion fuels. There also models that employ the available understanding of uranium-alloy fuels and significant work has been done to describe U-xMo and U-xPu-Zr fuels. This broad range of experience affords the theories great portability and the flexibility to be retrofitted to describe the behavior of similar-structured fuels. The Rest Models provide mechanistic and/or kinetic theories that can be extrapolated to descrive a number of existing and candidate nuclear fuels.

1.2 Structure and sources

The paper will follow a thematic description of fission product behavior concentrating of on three main areas: a description of fission product behavior in normal operating conditions; a review of the Dispersion Analysis Research Tool; the prediction of swelling in U-Pu-Zr fuels; a description of fission product behavior in off-normal, transient, operating conditions; a model of volatile fission product (VFP) behavior; and a description of fission product behavior in amorphous nuclear fuels.

1.2.1 Chapter organization

Some of the important characteristics of nuclear fuel behavior during normal operating conditions can be described by understanding how bubble nucleation and the migration of single gas-atoms and bubbles takes place within this regime. In the first section of Chapter 2, these mechanisms are looked at in detail and are followed by a discussion of bubble interlinkage. Fuel element swelling behaviors are treated at high and low burnups and a description of how solid fission gases affect swelling is included. Major gas release mechanisms are presented and a section is devoted to the influence of fuel microstructure on fission product behavior.

The Dispersion Analysis Research Tool (*DART*) is a comprehensive dispersion fuel analysis code that contains mechanistically-based fuel and reaction-product swelling models, a one dimensional heat transfer analysis and mechanical deformation models. Chapter 3 provides a summary of the key mechanistic components of the model.

Studies of the uranium-alloy fuel, U-xPu-Zr, provide a traditional model of uranium-alloy behavior under irradiation. A treatment of the observed cavitational swelling in the α-uranium zone and a proposed theory for he amorphous-like plastic flow of the γ-uranium zone is presented in Chapter 4. A brief discussion on the parallels between the *intermediate* zone and the recrystallized rim zones in LWR fuel is included here, as well.

Chapter 5 assesses some of the major issues present in off-normal operating conditions. These deal with the phenomenon known as *microcracking* as well as enhanced swelling and fission gas release mechanisms.

Nuclear reactor safety is a continuing concern that has been highlighted by the incidents of Three Mile Island and, more emphatically, the Chernobyl meltdown of 1986. At the fuel element level the majority of these concerns are addressed through an understanding of VFPs. VFPs are gaseous fission products, such as cesium, iodine and strontium, that may disrupt proper reactor opera-

tion and pose a health risk if not adequately contained. Having a precise idea of the location and interaction of these gases is essential to safe and efficient nuclear design and operation. Thus, Chapter 6 will investigate the behavior of VFPs during steady-state as well as transient operating conditions.

Important work has been done on fuels that turn amorphous under irradiation. This phenomenon has been observed, and subsequently described, in the Rest Models, in uranium-silicide fuels. The model is reviewed, complete with validation data, in Chapter 7.

Chapter 8 provides provides a brief outline of possible development areas within the field related to the work collected in this report.

1.2.2 Major sources

The majority of the models presented in this paper are based on the analytical theories developed by Rest in *GRASS-SST* and later modified and expanded in *FASTGRASS* . A chapter is dedicated to a review of the Dispersion Analysis Research Tool (*DART*) model and the principles touched upon are used for the description of amorphous fuels in Chapter 7. Additionally, several separate effects discussed in individual publications by Rest are included.

GRASS-SST is a mechanistic model for the behavior of fission gas products in steady-state and transient conditions. Essentially, *FASTGRASS* is a fast-running alternative to *GRASS-SST* , the main difference being in the way algorithms are used to calculate the densities of bubbles in each of a number of bubble size classes. In *GRASS-SST* , each bubble size class is characterized by an average number of atoms per bubble, the value of which differs from that of the preceding size class by a constant multiplier. The number of size classes is a variable that is determined dynamically during a computer run. Changes in the bubble size distribution, caused by bubble coalescence and irradiation-induced re-solution, for example, are determined by solving a large number of integral/differential equations for each time-step. An iterative solution of a large number of coupled equations is a major contributor to the computer running times of *GRASS-SST* . In contrast to the multiclass description of the bubble size distribution in *GRASS-SST* , *FASTGRASS* calculates the evolution of the average size bubble.

Chapter 2

Behavior of gaseous fission products in normal reactor environments

The analytical models designed by Jeff Rest present a theoretical foundation for the description of fission products in irradiated fuel. Gaseous fission products are responsible for many of the observable and performance characteristics of these fuels. Understanding the interaction of these products and the fuel form the basis for developing predictive, physical models. One application of these models, for example, is to calculate fuel swelling as a result of fission product behavior or the evolution of gaseous fission products that are released from the fuel element to the fuel-cladding gap and plenum. The results derived from such calculations highlight the importance that understanding the rates of emission of fission gases can have on fuel-rod and reactor design consequences.

To appreciate the dynamics of this highly active system, this chapter will strive to develop a description of how gaseous and fission products behave in irradiated nuclear fuels. The models described in the following sections will lay the groundwork to understand how these products influence fuel swelling, fission gas release and their relationship to the evolving fuel microstructure.

The sections covered in this chapter treat with the concentration and distribution of gaseous fission products within the fuel, from within the grain to the grain boundary and the so called triple-points. Once this foundation is established, models are presented to account for fuel element swelling. Swelling is a complex process. To clearly explain the underlying mechanisms that lead to the swelling of the fuel, the subject that has been divided into several subsections. Each subsection deals with an individual aspect of fuel swelling, and the

different operating environments that lead to swelling. In the final section of this chapter, the salient features of fission gas release are reviewed and a validation of the *FASTGRASS* code with respect to fission gas release is provided.

2.1 Gaseous fission product behavior

There are two basic forms of fission products. The two forms, solid or gaseous, are distinguished by the gaseous product's tendency to organize itself into bubbles within the fuel. Completely soluble fission products that can replace heavy-metal atoms in the matrix, and do not nucleate into bubbles, are considered solid fission products[1].

The calculation of how solid fission products contribute to the description of the fuel is, compared to the gaseous products, relatively straight forward. For that reason this section will concentrate on gaseous fission product behavior. Solid fission products, however, will be discussed in §2.2.1. Here, a description of bubble behavior particular to its distribution in the matrix, e.g. within the grain or on the grain face, will be forwarded. This will lead into a discussion of bubble interlinkage.

2.1.1 Nucleation and growth of intragranular fission gas bubbles

The concentration of gas atoms, C_g, is determined by solving the equation

$$\begin{aligned}\frac{dC_g}{dt} &= -16\pi F_N r_g D_g C_g^2 - 4\pi \left(D_g + D_b\right)\left(r_g + r_b\right) C_g C_b \\ &\quad - \pi \left|V_b - V_g\right| \left(r_g + r_b\right)^2 C_g C_b - S_v^{\alpha\alpha} V_g C_g + \frac{6D_g}{d_g}\frac{\partial C_g}{\partial r}\Big|_{r=d_g/2} \\ &\quad - \frac{3C_g d_g(t) V_{gb}}{d_v^g} + \kappa \dot{f} + bN_b C_b + \delta b N_f C_f + \delta b N_e C_e \quad .\end{aligned} \tag{2.1.1}$$

In Eq. (2.1.1), r_g, r_b, D_g, D_b and V_g, V_b are the radii of the intragranular gas atom and gas bubble diffusion coefficients and velocities, respectively. F_N is the bubble nucleation factor, i.e. the probability that two gas atoms that have come together actually stick. The term, $S_v^{\alpha\alpha}$ is the grain boundary area per unit volume; d_g, the grain diameter; $\dot{f}$, the fission rate (fissions $\cdot$ cm^{-3} $\cdot$ s^{-1}); and κ, the number of gas atoms produced per fission.

The successive terms on the right-hand-side (RHS) of Eq. (2.1.1) represent,

respectively, 1) the loss of gas atoms in dynamic solution due to bubble nucleation; the 2) random and 3) biased capture of gas atoms by bubbles; 4) biased and 5) random diffusion of gas atoms to grain boundaries; 6) loss of gas atoms due to grain-boundary sweeping; 7) gas atom generation due to fission; 8-10) the gain of gas atoms due to gas atom re-solution from intragranular, grain face and grain edge bubbles.

The fifth term on the RHS of Eq. (2.1.1), the flux of gas atoms diffusing to the grain boundaries in a concentration gradient, is obtained by solving for the concentration of gas atoms, C_g, within a spherical grain satisfying the equation

$$\frac{\partial C_g}{\partial t} = \frac{1}{r^2}\frac{\partial}{\partial r}\left(D_g r^2 \frac{\partial C_g}{\partial r}\right) + \kappa \dot{f} \quad , \tag{2.1.2}$$

where r is a radial coordinate on the sphere.

In general, Eq. (2.1.2) is solved with the boundary conditions

$$C_g = 0 \text{ at } t = 0 \qquad \text{for } 0 \le r \le d_g/2 \quad , \tag{2.1.2a}$$

$$C_g = 0 \text{ at } r = d_g/2 \qquad \text{for } t_0 \le t \le t_0 + \Delta t \quad , \tag{2.1.2b}$$

$$\frac{\partial C_g}{\partial t} = 0 \qquad \text{at } r = 0 \text{ for } t_0 \le t \le t_0 + \Delta t \quad , \tag{2.1.2c}$$

where Δt is an increment of time.

The concentration of gas atoms in a spherical grain described in 2.1.2 is

$$\frac{1}{r^2}\frac{\mathrm{d}}{\mathrm{d}r}\left(D_g r^2 \frac{\mathrm{d}C_g}{\mathrm{d}r}\right) - \frac{C_g}{\delta t} + \frac{C_g^0}{\delta t} + \kappa \dot{f} = 0 \quad . \tag{2.1.3}$$

Euler's theorem may now be used to obtain a variational principle equivalent to Eq. (2.1.3):

$$\delta \int_0^{1/2d_g} 4\pi \left[\frac{D_g}{2} \left(\frac{\mathrm{d}C_g}{\mathrm{d}r} \right)^2 + \frac{C_g^2}{2\delta t} - \left(\frac{C_g^0}{\delta t} + \kappa \dot{f} \right) C_g \right] r^2 \mathrm{d}r = 0 \quad , \qquad (2.1.4)$$

which assumes that Dirichlet boundary conditions are to be applied. An approximate solution to the problem may now be obtained by choosing a trial function that satisfies the boundary conditions and minimizes the integral in Eq. (2.1.4) in terms of free parameters in the function. Many types of trial functions could be chosen, but piecewise functions are easier to handle than global functions. Quadratic functions are attractive because they allow an exact representation of Eq. (2.1.2) for long times. To meet the objective of a realistic level of accuracy with a minimum of calculating time, the spherical grain is split into two concentric regions of approximately equal volume, Fig. 2.1. In each region, the gas concentration is represented by a quadratic function constrained to have $\mathrm{d}C_g/\mathrm{d}r = 0$ at $r = 0$. In the outer Region II, Fig. 2.1, the concentration function is constrained to a value of $C_g = 0$ at $r = d_g/2$. The two functions are also constrained to be continuous at the common boundary of the two regions. This leaves three free parameters. Mathews and Wood[2] chose these to be the concentrations C_1^g, C_2^g, and C_3^g, respectively, for the radius ratios $\rho_1 = 0.4$, $\rho_2 = 0.8$, and $\rho_3 = 0.9$, where $\rho = 2r/d_g$ These positions are the midpoint radius of Region I, the boundary between the regions and the midpoint radius of Region II, respectively. Thus the trial functions are as follows:

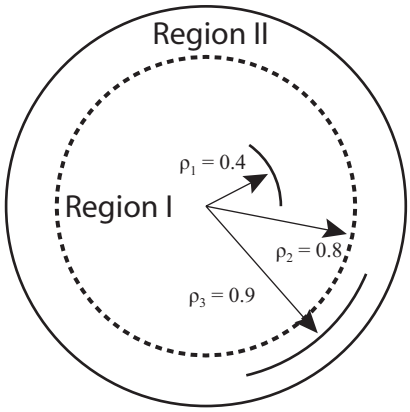

Figure 2.1: Configuration of the two zone model.

For Region I,

$$C_g = C_1^g \left(0.64 - \rho^2\right)/0.48 + \left(\rho^2 - 0.16\right)/0.48 \quad . \tag{2.1.4a}$$

For Region II

$$C_g = 5C_2^g \left(10\rho^2 - 19\rho + 9\right) + 10C_3^g \left(18\rho - 10\rho^2 - 8\right) \quad . \tag{2.1.4b}$$

Eqs. (2.1.4a) and (2.1.4b) are substituted for C_g in Eq. (2.1.4) and an extremum is found by differentiating with respect to C_1^g, C_2^g and C_3^g in turn. The following three linear equations are thus obtained:

$$\left(q_1 D_g/d_g^2 + q_2/\delta t\right) C_1^g + \left(q_3 D_g/d_g^2 + q_4/\delta t\right) C_2^g = K_g q_5 + \left(C_1^0 q_2 + C_2^0 q_4\right)/\delta t \quad , \tag{2.1.4c}$$

$$\left(q_3 D_g/d_g^2 + q_4/\delta t\right) C_1^g + \left(q_2 D_g/d_g^2 + q_7/\delta t\right) C_2^g + \left(q_8 D_g/d_g^2 + q_9/\delta t\right) C_3^g = K_g q_{10} + \left(C_1^0 q_4 + C_2^0 q_7 + C_3^0 q_9\right)/\delta t \quad , \tag{2.1.4d}$$

$$\left(q_9 D_g/d_g^2 + q_9/\delta t\right) C_2^g + \left(q_{11} D_g/d_g^2 + q_{12}/\delta t\right) C_3^g = K_g q_{13} + \left(C_2^0 q_9 + C_3^0 q_{12}\right)/\delta t \quad , \tag{2.1.4e}$$

where C_1^0, C_2^0 and C_3^0 are the values of the concentrations at the evaluation points at the start of the time increment. The various q coefficients are integrals, which, when directly evaluated, are, to four figures,

$$\begin{array}{lll} q_1 = 4.552, & q_2 = 0.06935, & q_3 = -4.552, \\ q_4 = 0.02167, & q_5 = 0.09102, & q_6 = 37.78, \\ q_7 = 0.07614, & q_8 = -38.72, & q_9 = 0.008456, \\ q_{10} = 87.04, & q_{11} = 0.08656, & q_{12} = 0.01008, \\ q_{13} = 0.1083. & & \end{array}$$

Equations (2.1.4c) - (2.1.4e) can be directly solved to obtain the concentrations C_1, C_2 and C_3 as follows:

$$C_1^g = \frac{X_1 - F_2 C_2^g}{F_1} \quad , \tag{2.1.4f}$$

$$C_2^g = \frac{\frac{F_2}{F_1} X_1 + \frac{F_4}{F_5} X_3 - X_2}{\frac{F_2}{F_1} F_2 + \frac{F_4}{F_5} F_4 - F_3} \quad , \tag{2.1.4g}$$

and

$$C_3^g = \frac{X_3 - F_5 C_2^g}{F_5} \quad , \tag{2.1.4h}$$

where

$$F_1 = q_1 D_g / d_g^2 + q_2 / \delta t, \qquad F_2 = q_3 D_g / d_g^2 + q_4 / \delta t,$$

$$X_1 = K_g q_s + \left(C_1 q_2 + C_2 q_4\right) / \delta t,$$

$$F_3 = q_5 D_g / d_g^2 + q_6 / \delta t, \qquad F_4 = q_7 D_g / d_g^2 + q_8 / \delta t,$$

$$X_2 = K_g q_{10} + \left(C_1^0 q_4 + C_2^0 q_6 + C_3^0 q_8\right) / \delta t,$$

$$F_5 = q_9 D_g / d_g^2 + q_{10} / \delta t, \text{ and}$$

$$X_3 = K_g q_{13} + \left(C_2^0 q_8 + C_3^0 q_{10}\right) / \delta t \quad .$$

The flux of gas atoms to the boundary (in units of atoms $\cdot$ cm^{-3} $\cdot$ s^{-1}) is given by

$$J = \frac{6 D_g}{d_g} \frac{\partial C}{\partial r}\Big|_{r = d_g/2} \quad , \tag{2.1.4i}$$

$$J = \frac{D_g}{d_g^2} \left(-60 C_2^g + 240 C_3^g\right) \quad . \tag{2.1.4j}$$

For proper coupling of the diffusive flow process to other processes that affect fission gas behavior, (e.g. gas atom re-solution, gas atom trapping by bubbles,

and gas bubble nucleation and coalescence) information is required on the average concentration of fission gas within the grain.

Matthews and Woods[2] determined that the best expression for the average concentration within the grain, $\overline{C}_g$, is given by

$$\overline{C}_g = 0.2876C_1^g + 0.2176C_2^g + 0.4216C_3^g \quad . \tag{2.1.4k}$$

At the end of the iteration, the concentrations C_1, C_2, and C_3 in Eq. (2.1.4k) are scaled by imposing the condition that the average concentration calculated by use of Eq. (2.1.4k) is equal to the average concentration calculated by use of Eq. (2.1.1), i.e., that

$$\overline{C}_g = C \quad . \tag{2.1.4l}$$

The modified C_1^g, C_2^g, and C_3^g then become the initial values of these concentrations (i.e., C_1^0, C_2^0, and C_3^0) to be used in the next iteration. The diffusive flow of fission-gas bubbles is treated in a manner analogous to that for the fission-gas atoms, but with $\dot{f} = 0$ in Eq. (2.1.2). This method of coupling diffusive flow to other processes that affect fission-gas behavior (e.g., gas atom re-solution, gas atom trapping by gas bubbles, gas nucleation and coalescence) is computationally efficient and have been benchmarked against various analytical solutions[2].

The last three terms on the RHS of Eq. (2.1.1), which account for the effects of fission-induced gas atom re-solution depend on the rate, b, at which gas atoms are ejected from the bubble. The rate b is calculated under the assumption that gas atom re-solution from a spherical bubble is isotropic and proceeds by the knocking out of single gas atoms. Thus,

$$b = \frac{3b_0\dot{f}}{r_b^3} \int_{r_b-\lambda}^{r_b} \left(\frac{1+\cos\theta}{2}\right) r^2 \mathrm{d}r \quad , \tag{2.1.5}$$

where $\cos\theta = \left(r_b^2 - \lambda^2 - r^2\right)/2r\lambda$. A straightforward integration of Eq. (2.1.5) results in

$$b = \frac{3b_0\dot{f}}{r_b^3}\left(G_2 - G_1\right) \quad , \tag{2.1.5a}$$

where

$$G_2 = r_b^2 \left[\frac{r_b}{6} + \frac{r_b^2}{16\lambda} + \frac{1}{8}\left(\lambda - \frac{r_b}{\lambda}\right) \right] \quad , \tag{2.1.5b}$$

$$G_1 = (r_b - \lambda)^2 \left[\frac{r_b - \lambda}{6} + \frac{(r_b - \lambda)^2}{16\lambda} + \frac{1}{8}\left(\lambda - \frac{r_b}{\lambda}\right) \right] \quad , \tag{2.1.5c}$$

where λ is the average distance an ejected atom travels and b_0 is a measurable property of the material.

The last two terms of Eq. (2.1.1) contain the variable δ, which is a measure of the "strength" of gas atom re-solution from grain boundary bubbles. The magnitude of δ is closely related to what is formally known as backward flux[3]. This concept will be investigated in detail in §2.1.2.

To solve for C_g with Eq. (2.1.1), a number of terms on the RHS must be determined. RHS Terms 2, 3, 6 and 8 depend on C_b. The equation for C_b, the concentration of intragranular bubbles, is given by

$$\begin{aligned} \frac{\mathrm{d}C_b}{\mathrm{d}t} &= -16\pi F_N r_g D_g C_g^2/N_b + 4\pi \left(D_g + D_b\right)\left(r_g + r_b\right) C_g C_b/N_b \\ &\quad + \pi \left|V_b - V_g\right| \left(r_g + r_b\right)^2 C_g C_b/N_b - S_v^{\alpha\alpha} V_b C_b + \frac{6D_g}{dg}\frac{\partial C_b}{\partial r}\Big|_{r=d_g/2} \\ &\quad - \frac{3C_b}{d_g} V_{gb} - bC_b + \frac{3V_{gb}}{d_g} N_b \left(\frac{K_f}{N_f} C_f + \frac{K_e}{N_e} C_3\right) \quad . \end{aligned} \tag{2.1.6}$$

The interpretation of the first six terms on the RHS of Eq. (2.1.6) are analogous to those given for Eq. (2.1.1). The last term accounts for the introduction of grain face and grain edge bubbles into the lattice due to bubble pull-off (if the bubbles are bigger than a given critical size K_f and/or $K_e = 1$; otherwise they are equal to zero) from a moving grain boundary, and/or the presence of large temperature gradients.

2.1.2 Intergranular Fission Gas: Grain Faces and Edges

Six basic quantities must still be determined before Eqs. (2.1.1) and (2.1.6) can be solved. C_f, C_e will be discussed in this section. The next section provides

a representation of how N_b, N_f, and N_e are calculated. The velocity of the moving grain boundary, V_{gb}, is defined in §5.2.

The equation for C_f, the concentration of gas bubbles on the grain faces (assuming that the grains have an approximate tetrakeidecahedral structure) is given by

$$\begin{aligned}\frac{\mathrm{d}C_f}{\mathrm{d}t} =& -\delta b C_f - \frac{3V_{gb}}{d_g} K_f C_f - \varkappa V_f C_f - \frac{V_f \Phi_\chi}{d_g C_f} - \frac{P_A C_f}{t} \\ &+ S_v^{\alpha\alpha}\left(\frac{V_g C_g}{N_f} + \frac{V_b C_b N_b}{N_f}\right) - \frac{6}{d_g}\left[\frac{D_g}{N_f}\frac{\partial C_g}{\partial r}\Big|_{R=d_g/2} + \frac{D_b N_b}{N_f}\frac{\partial C_b}{\partial r}\Big|_{R=d_g/2}\right] \\ &+ 3d(t)V_{gb}\left(\frac{C_g}{N_f} + \frac{C_b N_b}{N_f}\right)/d_g \quad . \end{aligned} \tag{2.1.7}$$

The first and second terms on the RHS of Eq. (2.1.7) are loss terms due to bubble destruction by gas atom re-solution and bubble pull-off, respectively. The third term on the RHS of Eq. (2.1.7) is the loss of grain-face bubbles due to biased migration out of the node (where V_f is the velocity of a bubble on the grain face and $\varkappa =$ area/vol and area = cross-sectional area of node boundary, while vol = volume on node; in general, for solid fuel, a node has the shape of a cylindrical annulus). The fourth and fifth terms represent the biased grain-face bubble migration, and migration of grain-face gas through grain-face channels to the grain edges. Φ_χ is the average number of grain faces per grain. Similar to the terms found in Eq. (2.1.1), the remaining three terms give the biased diffusion of fission-gas atoms and bubbles from the lattice, the random diffusion of fission-gas atoms and bubble from the lattice, and the gain of fission-gas atoms and bubbles by the mechanism of grain-boundary sweeping, respectively.

The equation for C_e, the grain edge bubble concentration, is given by

$$\begin{aligned}\frac{\mathrm{d}C_e}{\mathrm{d}t} =& -\delta b C_e - \frac{3V_{gb}K_e C_e}{d_g} + V_f \frac{\Phi_\chi}{d_g}\frac{N_e}{N_f}\left(1 - P_I\right)C_f \\ &+ P_A \frac{N_e}{N_f}\left(1 - P_I\right)\frac{C_f}{t} - \frac{\mathrm{d}P_I}{\mathrm{d}t}C_e \quad . \end{aligned} \tag{2.1.8}$$

In Eq. (2.1.8), the last term on the RHS represents the loss of gas due to release through long range interconnection of grain edge porosity to a free surface. The *FASTGRASS* model for calculating the probability of long-range grain interconnection is based on the assumption that the long-range interconnection is a function of the swelling of grain-edge bubbles. This assumption is supported by experiment[4] as well as theory[5]. To account for the local fluctuations in

fuel microstructure and gas bubble morphology, the grain-edge/porosity interlinkage fraction, P_I, is assumed to be a statistical distribution around an average value of the grain-edge swelling, B_{vedge}:

$$P_I = \frac{1}{\sigma_e\sqrt{2\pi}} \int\limits_{x=B_{crit}} exp\left[\frac{-\left(x - B_{vedge} - B_{vpor}\right)^2}{2\sigma_e^2}\right] \mathrm{d}x \quad , \tag{2.1.9}$$

where $B_{vedge} = 4/3\pi R_e^3 \sigma_e C_e$, and σ_e is a geometrical factor that accounts for the ellipsoidal shape of grain-edge bubbles. $B_{vcrit} = 0.05$ is the value of the grain edge swelling at which long-range interconnection would take place if the fuel microstructure and gas bubble morphology were homogeneous; $B_{vpor} = 0.0$ for $\rho \geq 92\%$ of the theoretical density. In the absence of microcracking, the fission gas that would have been vented via the cracks remains on the grain boundaries. (*FASTGRASS* contains a model for intergranular microcracking due to overpressurized fission-gas bubbles. This model has been discussed in a previous paper[4] and will be reviewed in §5.1.1.) The effects of microcracking on interlinkage are included by redefining P_I as $P_I = \max\left(P_I, M_c\right)$, where M_c is the fraction of the grain-boundary area/volume which has opened up due to microcracking. Retained grain-edge fission gas causes the deformation of the grain edges (i.e., gain-edge fission-gas-bubble swelling), and the subsequent increased long-range interconnections of grain-edge tunnels. This interconnection of grain-edge tunnels provides the pathways for enhanced fission-gas release. The *FASTGRASS* intergranular swelling model have been benchmarked against experimental results[6].

Gas atoms that are knocked out of grain boundary bubbles are evenly dispersed within an annulus of thickness λ adjacent to the grain boundary. This backward flux of gas atoms affects the concentration gradient of gas atoms from the matrix to the boundary, and thus the overall flux of gas atoms to the boundary. Thus, this backward flux of gas atoms, in atoms $\cdot$ m^{-2} $\cdot$ s^{-1}, can be thought of as an additional matrix gas-atom generation mechanism and is given by

$$\dot{f}(\lambda)_{boundary} = \frac{3bN_b n(t)}{d_g}\frac{V}{V_\lambda} \quad , \tag{2.1.10}$$

where V is the volume of the grain and V_λ is the volume of the annulus of thickness λ within which the backward flux of gas atoms from the boundary bubbles is deposited. The term $n(t)$ is the number of gas atoms in a grain boundary bubble, i.e.

$$n(t) = \sum_{\delta t} \left(\frac{f_c J(t)}{N_b} + z\,(1 - f_c)\, D_g C_g^b - bn(t) \right) \delta t \quad , \tag{2.1.11}$$

where b is the gas-atom re-solution rate, $f_c \approx \pi R_b N_b$ is the fractional coverage of the grain boundary by bubbles, z is the grain-boundary diffusion enhancement factor, N_b is the total number of bubbles on the boundary (bubbles $\cdot$ m^{-2}), and C_g^b is the gas-atom concentration on grain boundaries (atoms $\cdot$ m^{-2}), given by

$$C_g^b = \sum_{\delta t} \left((1 - f_c)\, J(t) + z D_g C_g^b N_b \right) \delta t \quad . \tag{2.1.12}$$

When f_c is small (e.g., during the initial stages of boundary-bubble growth) most of the gas reaching the boundary exists as single gas atoms and diffuses by random walk to the boundary bubbles. This is analogous to gas atom accumulation by bubbles in the grain interior. When f_c is large, the majority of the gas reaching the boundary flows directly into boundary bubbles. The grain-boundary enhancement factor, z, accounts for the general view that gas atom diffusion on the boundary is more rapid than in the matrix due to the existence of more space and sites (e.g., ledges) from which and to which the gas atoms can hop.

In Eq. (2.1.10), the first ratio on the right hand side represents the backward flux of gas (atoms $\cdot$ m^{-2} $\cdot$ s^{-1}) and the second ratio the fraction of the intragranular volume within which this gas is deposited. This value is independent of λ. Thus, as λ decreases V_λ becomes smaller and $\dot{f}(\lambda)_{boundary}$ increases.

Calculation of N_b, N_f and N_e

Equations (2.1.1), (2.1.6), (2.1.7), and (2.1.8) express mass balance and are solved by assuming that the average number of atoms per bubble does not change over the integration time step, i.e., $\dot{N}_b = \dot{N}_f = \dot{N}_e = 0$. Subsequent to the calculation of the C_is, changes in N_i are calculated by examining the bubble growth and shrinkage fluxes that influence the average size bubble. For example, changes in N_b are calculated by evaluating

$$\dot{N}_b \propto \frac{1}{C_b}\left[16\pi r_b D_b C_b^2 + \pi r_b^2 \alpha_b V_b C_b^2 + 4\pi\left(D_g + D_b\right)\left(r_g + r_b\right)\frac{C_g C_b}{N_b} - bC_b - 16\pi F_N r_g D_g C_g^2 + \frac{3V_{gb}N_b}{d_g}\left(\frac{K_f}{N_f}C_f + \frac{K_e}{N_e}C_e\right)\right] \quad . \tag{2.1.13}$$

In Eq. (2.1.13), the first three terms on the RHS correspond to the growth of the average size bubble due to random and biased coalescence of these bubbles with each other, and the growth of these bubbles due to accumulation of gas atoms. The 4^{th} and 5^{th} terms on the RHS of (2.1.13) represent the shrinkage of the average size bubble due to bubble destruction by fission-induced gas atom re-solution, and due to the generation of very small bubbles by gas-atom nucleation (i.e., the introduction of small bubbles will tend to weight the average size bubble toward smaller sizes). The last two terms represent the growth of the average size bubble by introducing into the lattice larger grain-face and grain-edge bubbles which have become detached from the moving grain boundary. The proportionality sign in (2.1.13) indicates that the changes in N_b are computed using a numerical algorithm which evaluates (2.1.13) and increments or decrements N_b by an amount proportional to this value. When N_b is calculated in this fashion, it agrees very well with results of calculations for the evolution of the bubble size distribution made with the *GRASS-SST* mechanistic model[7]. The equations for $\dot{N}_f$ and $\dot{N}_e$ are obtained in an analogous fashion to Eq. (2.1.13).

2.1.3 Bubble interlinkage

Fission gas can migrate from the grain faces to the grain edges by diffusion (random or biased) via-short circuit paths created by grain-face channel formation (i.e. interlinkage of grain-face bubbles). Channel formation on the faces is a function of the amount of gas on the faces. The method of calculating grain-face saturation by fission gas in *FASTGRASS* is by directly addressing the calculated distribution of fission-gas bubble sizes. The projected areal coverage of the grain face by these bubbles, per unit volume, is given by

$$A_F = \pi R_f^2 C_f f_f(\theta) \quad , \tag{2.1.14}$$

where R_f is the average radius of grain-face bubbles and $f_f(\theta)$ is a geometrical factor that accounts for the lenticular shape of the these bubbles. If the gas is assumed to be made up of equal, closely packed, touching bubbles, the

Parameter	Value	Reference
D_g	$2 \times 10^{-19}\mathrm{m}^2/\mathrm{s}$	[8]
$b_0\dot{f}$	$2 \times 10^{-4}\mathrm{s}^{-1}$	[9]
λ	$5 \times 10^{-8}\mathrm{m}$	[1]
N_b	$1 \times 10^{12}\mathrm{m}^{-2}$	[10]
z	10	[3]
d_g	$2 \times 10^{-6}\mathrm{m}^2/$	
T	373 K	

Table 2.1: Nominal values of key parameters used in the calculation

maximum areal coverage per unit area of grain-face is $A_F^* = 0.907$. (Under conditions where this assumption is not valid, $A_F^* < 0.907$, the *FASTGRASS* code utilizes a nominal value of $A_F^* = 0.50$). Grain-face saturation (i.e. the initiation of gas channel formation) occurs when

$$A_F \geq A_F^* S_v^{\alpha\alpha} \quad , \tag{2.1.15}$$

where $S_v^{\alpha\alpha}$ is the grain-face area per unit volume.

Equations (2.1.14) and (2.1.15) do not account for local variations in fuel microstructure. To include these effects in the calculations of grain-face channel formation, it is assumed that the local variations in fuel microstructure can be represented by the width, σ_f, of a distribution of A, Eq. (2.1.14), such that the fraction of grain-face channel interlinkage is given by

$$P_A = \frac{1}{\sigma_f\sqrt{2\pi}} \int\limits_{x=A_F^* S_v^{\alpha\alpha}} exp\left[\frac{(-x-A)^2}{2\sigma_f^2}\right] \mathrm{d}x \quad . \tag{2.1.16}$$

The width of the distribution in Eq. (2.1.16) is a function of erratic structural parameters, depending on local fuel condition and heterogeneity; in principle, it can be determined experimentally.

With larger grains the grain-face area per unit volume is smaller, so that for a given distribution of fission gas, the grain faces of larger grains reach their saturation limit quicker than those of small grains (see Eq. (2.1.16)), and thus vent their content to of fission gas to the grain edges sooner. At higher temperatures, increased coalescence rates lead to larger bubbles on the faces; these larger bubbles link up more easily to vent gas to the grain edges. Therefore, a combination of high temperatures and large grain size results in more rapid

and extensive channel formation, an hence, in quicker gas transport from the grain faces to the edges.

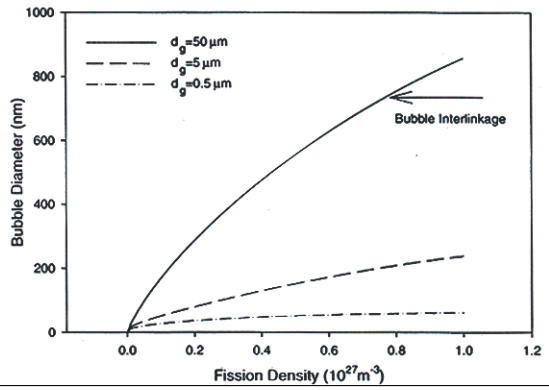

Figure 2.2: Calculated bubble diameter vs. fission density for three values of grain size. The arrow shows the point at which the grain-boundary bubbles interlink.

Fig. 2.2 shows the calculated bubble diameter vs. fission density for three values of grain size. The nominal values of key parameters used in the calculation of Fig. 2.2 are listed in Table 2.1. The severity of irradiation-induced resolution of gas atoms from the boundary to the matrix on the intergranular bubble growth is dependent on the ratio λ/d_g: smaller values of λ/d_g lead to larger values for the flux J. As shown in Fig. 2.2, the calculated intergranular bubble sizes are larger for larger grain diameters (i.e., smaller values of λ/d_g). The arrow in Fig. 2.2 shows the point at which the grain-boundary bubbles interlink as given by Eq. (2.1.15). The effect of calculated grain-boundary bubble diameter on the value of λ/d_g for a fixed grain size and variable λ is demonstrated in Fig. 2.3, where calculated bubble diameter vs. fission density is shown for three values of gas-atom knock-out distance. Decreasing the value of λ (i.e., smaller values of λ/d_g) leads to larger fluxes and a commensurate increase in the calculated bubble size.

The effect of the back flux of gas atoms can also be seen in Fig. 2.4, which shows the calculated fractional gas release to grain boundary vs. fission density for three values of gas-atom re-solution rate. For re-solution rates in Fig. 2.4 of 2×10^{-4} and 2×10^{-3} s^{-1} the fractional gas release decreases after an initial increase. This behavior is due to the growing strength of the backward flux of gas atoms as the number of gas atoms in boundary bubbles increases (e.g., see last term in Eq. (2.1.11)).

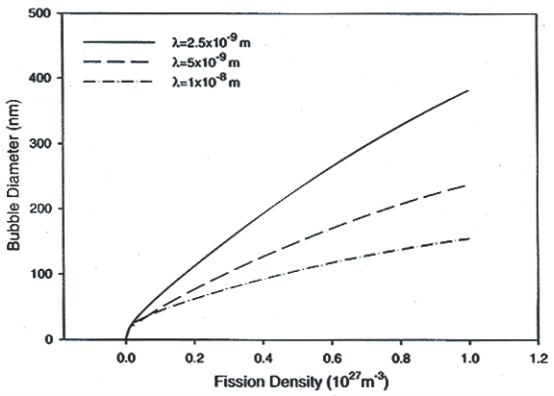

Figure 2.3: Calculated bubble diameter vs. fission density for three values of grain size for three values of gas-atom knock-out distance.

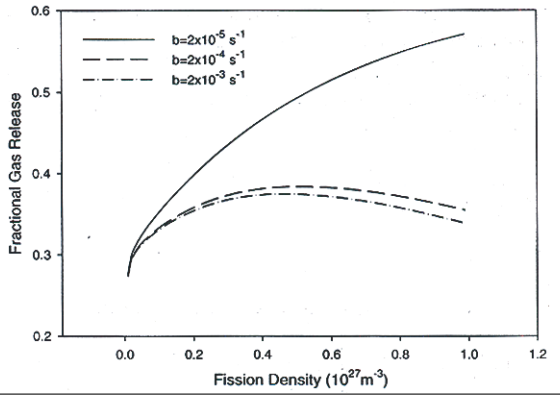

Figure 2.4: Calculated fractional gas release to grain boundary vs. fission density for three values of gas-atom re-solution rate.

2.1.4 Intra- and Intergranular bubble swelling

Intragranular bubble swelling is very straight-forward and is proportional to the bubble density, as follows.

$$\frac{\Delta V}{V} = \frac{4}{3}\pi r_b^3 C_b \quad . \tag{2.1.17}$$

Gas bubble swelling in the boundary evolves somewhat diffrently as fission gas can migrate from the grain faces to the grain edges by diffusion (random and biased) and via short-circuit paths created by grain-face channel formation

(i.e., interlinkage of grain-face bubbles). Channel formation on the faces is a function of the areal coverage of the face by the fission gas. A realistic approach for calculating grain-face saturation by fission gas is to deal directly with the calculated fission-gas bubble distributions. Previous analysis[2, 4, 11, 12] have been based on the swelling of spherical bubbles. However, because $\cos\theta = \gamma_{gb}/2\gamma \neq 0$ ($\gamma = UO_2$ surface energy, γ_{gb} = grain boundary energy), it is more reasonable to assume that the bubbles are lenticular shaped pores containing m gas atoms and having a radius of curvature ρ, which are joined in the plane of the boundary with dihedral angles, $2\theta = 100^\circ$ (see Ref. [13]). The fractional swelling due to these bubbles is given by the expression

$$\frac{\Delta V}{V} = \frac{4\pi\rho^3 f(\theta)}{3Y} \quad , \tag{2.1.18}$$

where $f(\theta) = 1 - \frac{3}{2}\cos\theta + \frac{1}{2}\cos^3\theta$, and

$$\rho = \left(\frac{3mkT}{4\pi f(\theta)\gamma}\right)^{1/2} \quad . \tag{2.1.19}$$

m is the number of gas atoms in the bubble, and Y is the number of bubbles on the grain face per unit volume.

Eq. (2.1.19) was derived by assuming equilibrium and using the ideal gas law. The projected area coverage of the grain face by these bubbles per unit volume is given by

$$A = \pi\left(\rho\sin\theta\right)^2 Y \quad . \tag{2.1.20}$$

For fixed values of m and Y, Eqs. (2.1.18) - (2.1.20) result in values of $\Delta V/V$ and A which are ~ 0.86 smaller and ~ 1.74 larger, respectively, than those calculated assuming spherical bubbles.

2.2 Fuel element swelling

Fuel swelling is a multifaceted process that strongly depends on as-fabricated properties as well as in-pile conditions. The critical definition of swelling is understood as the positive change in volume of the fuel element. Volume growth

can be caused as a result of solid fission products, gaseous fission products, and often, a combination of the two. The volume of the fuel is also dependent on burn-up and temperature. How these factors affect fuel swelling will be discussed in this section.

2.2.1 Solid fission products

Solid fission products precipitate as metal inclusions (Mo, Ru, Tc, Rh, Pd), alkaline earth oxides ($BaZrO_3$) or the following associated compounds, Cs(Rb)I, $Cs(Rb)_2Te$, and $Cs(Rb)_2O$[14]. A common method to estimate solid fission product swelling as a result of irradiation is by using Anselin's calculation[15]. Olander[1] summarized it as follows

$$\left(\frac{\Delta V}{V}\right)_{\text{solid}} = \left(\sum_{\text{solid fp}} Y_i \frac{v_i}{v_U} - 1\right)\beta \quad , \tag{2.2.1}$$

where v_i is known as the *partial volume* of a solid fission product, Y_i is the elemental yield of a solid fission product and v_U is the partial volume of uranium, and β is the fractional burn-up. In (U,Pu)O_2 fuels, $v_{Pu} \approx v_U$, and only v_U is used.

Evaluating Eq. (2.2.1) for UO_2 and (U,Pu)O_2 fuels shows that, for every fission event, solid fission products are produced that demand 1.324 times as much volume as the uranium base[1, 15]. In terms of swelling rate, a measure of 0.32% volume increase per 10 GWd/tM, can be directly backed out. Due to several different factors, such as the distribution of the fission products along the fuel radius and the uncertainty over the chemical states of some of the precipitates (e.g., the likelyhood that the cesium, iodine, rubidium, and tellurium products are actually gaseous) the calculated rate may vary by about $\pm.15\%$[14, 15].

2.2.2 Low temperature | Low burn-up

There are three distinguishable state regimes that affect fuel swelling. These regimes are defined by the operating temperature and the degree of burn-up the fuel has undergone. Although both inexorable as well as intergranular bubble swelling always contribute to the total element swelling, within a particular regime, one type of mechanism tends to dominate the swelling rate.

An analytical approach to fuel element swelling was developed in a paper by

Rest in Ref. [14]. The theory avoids having to solve coupled sets of nonlinear equations by addressing gaseous fission product swelling in the following way. The gas-induced swelling rate is handled as a function of the amount of gas in bubbles and lattice size in the matrix. To calculate these values the theory tracks the evolution of the bubble population with respect to burn-up.

The rate of change of the density of gas in intragranular bubbles can be represented as the sum of two equations representing the time rate of change of the gas bubble density, c_b, and the quantity of gas atoms, n_b, in the bubble, i.e.,

$$\frac{\mathrm{d}c_b}{\mathrm{d}t} = \frac{16\pi F_N D_g r_g c_g(t) c_g(t)}{n_b(t)} - \frac{b}{2} c_b(t) \quad , \tag{2.2.2}$$

$$\frac{\mathrm{d}n_b}{\mathrm{d}t} = 4\pi r_b(t) D_g c_g(t) - \frac{b}{2} n_b(t) \quad . \tag{2.2.3}$$

In the low temperature regime ($T < 1200$ K), diffusion is athermal, but dependent on the fission rate $\dot{f}$ as follows,

$$D_g = D_0 \dot{f} \quad . \tag{2.2.4}$$

Bubble re-solution can also be considered to be proportional to the fission rate and is given by

$$b = b_0 \dot{f} \quad . \tag{2.2.5}$$

The gas-atom concentration and radius are given by c_g and r_g, respectively. The bubble nucleation factor, F_N, is assumed to be less than one and since nucleation is assumed to occur mainly along fission tracks, F_N has a value that is approximately the fractional volume of these fission tracks ($\approx 10^{-4}$)[16].

The first term on the RHS of Eq. (2.2.3) represents the formation rate of bubbles with size r_b. For every 2-atom bubble that is nucleated, $2/n_b$ of a bubble radius r_b is formed. That is, nucleation of n_b two-atom clusters leads to the gain of one bubble of radius r_b. This 'average sized' bubble is in the peak region of the bubble size distribution[17, 18].

The last term on Eq. (2.2.2) represents a loss due to *whole* bubble destruction, while the re-solution term on Eq. (2.2.3) is a loss term due to gas-atom *chipping*

from bubbles. Both these terms are included to adequately characterize the full range of the distribution as an "averaged size;' bubble. Additionally, the term $\frac{b}{2}c_b(t)$ is necessary to ensure that the density of bubbles decreases with irradiation, while $\frac{b}{2}n_b(t)$ is required to allow the number of gas atoms in bubbles to decrease. It should be noted that the use of the re-solution parameter, b, in both Eqs. (2.2.2) and (2.2.3), implies that both mechanisms contribute equally to re-solution. This assumption has not been experimentally tested.

It is assumed that the increase of bubble concentrations occurs at a significantly reduced rate after a long time has transpired and the LHS of Eq. (2.2.2) can be set to zero. Therefore, based on this assumption, the following solution for c_b, in terms of c_g and n_b, can be derived

$$c_b = \frac{16\pi F_N r_g D_0 c_g^2}{b_0 n_b(t)} \quad . \tag{2.2.6}$$

In general, r_b is related to n_b through the gas law and the capillarity relation. Using a modified van der Waals gas law,

$$\frac{2\gamma}{r_b}\left(\frac{4}{3}\pi r_b^3 - h_s b_v n_b\right) = n_b kT \quad , \tag{2.2.7}$$

where γ is the surface tension, b_v is the van der Waals constant for Xe, k is Boltzmann's constant, and T is the absolute temperature. Using h_s as a fitting parameter, this equation acts like the hard-sphere equation of state for certain values of T[19].

An approximate solution to Eq. (2.2.7) can be derived for bubbles in the nanometer size,

$$r_b(t) = \left(\frac{3h_s b_v n_b(t)}{4\pi}\right)^{1/3} \quad . \tag{2.2.8}$$

Setting the LHS of Eq. (2.2.3) to zero with an assumption similar to that used for Eq. (2.2.6) and using Eq. (2.2.8) the steady-state solution to Eq. (2.2.3) is

$$n_b(t) = \left(\frac{3h_s b_v}{4\pi}\right)^{1/2}\left(\frac{4\pi D_0 c_g(t)}{b_0}\right)^{3/2} \quad . \tag{2.2.9}$$

The fraction of gas, f_s, that diffuses to the grain boundary of grains with a diameter d_g can be approximated by

$$f_s = \frac{8}{d_g}\left(\frac{D_g t}{d_g^2}\right)^{1/2} - \frac{6}{d_g^2} D_g t \; ; \quad 4\pi^2 D_g t/d_g^2 \leq 1 \quad , \tag{2.2.10}$$

$$f_s = 1 - \frac{d_g^2}{60 D_g t} + \frac{3 d_g^2}{2 D_g t} \exp\left(-\frac{4\pi^2 D_g t}{d_g^2}\right) \; ; \quad 4\pi^2 D_g t/d_g^2 > 1 \quad , \tag{2.2.11}$$

according to Speight[20]. Assuming no gas is lost to the exterior and that all gas in solution, in intergranular bubbles, and on the grain boundary equals the amount of gas created by fission, the concentration of gas, $c_g(t)$, is given by

$$c_g(t) = \frac{-(1+f_s) + \left[(1+f_s)^2 + 64\pi f_n r_g D_g \dot{f} \beta t/b\right]^{1/2}}{32\pi f_n r_g D_g / b} \quad , \tag{2.2.12}$$

where β is the number of gas atoms produced per fission event.

According to Wood and Kear[21], bubbles in the grain boundary will initially nucleate into bubbles of radius R_b, as it is more likely for atoms to collide into other atoms than formed bubbles. As the bubble population continues to grow, single atoms will eventually have a higher likelihood of being captured into an existing nucleus rather than meeting another single atom. The grain boundary concentration per unit volume can be approximated by

$$C_b^V = \left(\frac{8 z a K}{12^{1/3} \pi^2 \zeta D_g \delta}\right)^{1/2} \quad , \tag{2.2.13}$$

where $\frac{a^3}{12}$ is the average atomic volume in UO_2 [22], a is the lattice constant, z is the number of sites visited per gas-atom jump, δ is the width of the boundary, ζ is a grain boundary diffusion factor and K is the flux of gas-atoms per unit area of grain boundary.

Rest[3] determined that the re-solution rate at the grain boundary is not negligible. However, the grain boundary acts like a very strong sink and the majority of atoms that are knocked out of the bubble get recaptured. The intergranular bubble nucleation and growth calculation incorporated into the estimation

of grain boundary bubble concentration can therefore safely ignore the effects of re-solution while providing a fairly accurate approximation.

Considering the above, the flux, K, of atoms at the grain boundary is given by

$$K = \frac{d_g}{3}\frac{\mathrm{d}c_g}{\mathrm{d}t}\frac{\mathrm{d}\left(f_s t\right)}{\mathrm{d}t} \quad . \tag{2.2.14}$$

Differentiating Eq. (2.2.12)

$$\frac{\mathrm{d}c_g}{\mathrm{d}t} = \frac{\beta\dot{f} - c_g\frac{\mathrm{d}f_s}{\mathrm{d}t}}{(1 + f_s + 32\pi f_n r_g D_g c_g/b)} \quad , \tag{2.2.15}$$

where, using Eq. (2.2.10),

$$\frac{\mathrm{d}(f_s t)}{\mathrm{d}t} = \frac{12}{d_g}\left(\sqrt{\frac{D_g t}{\pi}} - \frac{D_g t}{d_g}\right) \quad . \tag{2.2.16}$$

The concentration of gas on the grain boundaries, C_g, is given by

$$C_g = \frac{d_g}{3} f_s(t) c_g(t) \quad , \tag{2.2.17}$$

and the average number of gas atoms in a grain-boundary bubble is

$$N_b(t) = \frac{C_g(t)}{C_b^V(t)} \quad . \tag{2.2.18}$$

The radius, R_b, of a grain-boundary bubble can be derived from the solution to Eq. (2.2.7) as follows

$$\begin{aligned} R_b = &\left[\frac{3h_s b_v N_b}{8\pi} + \sqrt{\left(\frac{3h_s b_v N_b}{8\pi}\right)^2 - \left(\frac{N_b kT}{8\pi\gamma}\right)^3}\right]^{1/3} \\ &+ \left[\frac{3h_s b_v N_b}{8\pi} - \sqrt{\left(\frac{3h_s b_v N_b}{8\pi}\right)^2 - \left(\frac{N_b kT}{8\pi\gamma}\right)^3}\right]^{1/3} \end{aligned} \tag{2.2.19}$$

The fractional swelling due to fission gas is thus given by

$$\frac{\Delta V}{V} = \frac{c_g a^3}{4} + \frac{4\pi}{3}\left(r_b^3 c_b + \frac{3R_b^2 C_b^V}{d_g}\right) \quad . \tag{2.2.20}$$

In Eq. (2.2.20) the first RHS term accounts for the swelling caused by gas atoms in dynamic solution and the second term tracks the contribution of intragranular and intergranular bubbles[1], respectively.

2.2.3 Low temperature | High burn-up

As shown by Rest[14], at low temperatures, the fuel will continue to swell with higher burn-up. The swelling is mostly driven by fission-gas products (although inexorable swelling due to solid fission products should be considered as well). A novel behavior, first noticed on the radial periphery of LWR fuels, has been observed on fuels that have undergone long periods of irradiation. The surface of these fuels display a highly refined microstructure. Because of its initial sighting on the "rim" of LWR fuel rods this behavior has come to be known as the "rim effect", and more formally recrystallization.

What follows is a discussion of recrystallization in general, and how this process significantly affects swelling in low temperature, high burn-up conditions.

Onset of irradiation-induced recrystallization

Recrystallization was first used as a theory to account for the observation of a distinct swelling-rate spike that shifts to a higher fission density with increased fission rate. Fig. 2.5 shows this behavior for U_3Si_2, which is characteristic of many other oxide fuels and dispersion (while not in the amorphous phase) fuels. Calculations[23] with *GRASS-SST* [7] have interpreted the swelling as due to the combined effects of a population of bubbles below the limits of experimental resolution and a distribution of larger, visible bubbles attached to dislocations. The position of a peak in the bubble size distribution is determined by the offset between the growth of the bubbles due to diffusion of gas atoms and shrinkage due to fission-fragment-induced re-solution. Both, irradiation-enhanced diffusion and gas-atom re-solution have an approximately linear dependence on fission rate. Therefore, an increase in the rate

[1]The bubbles here are represented as spherical bubbles in accordance to van der Waals gas conditions. In §2.1.4, a lenticular bubble shape was used, however, and the conditions were approximated by the ideal gas law. Equation (2.2.20) is valid for the low temperature regime and most applications. However, care should be taken as it may be inadequate in some situations.

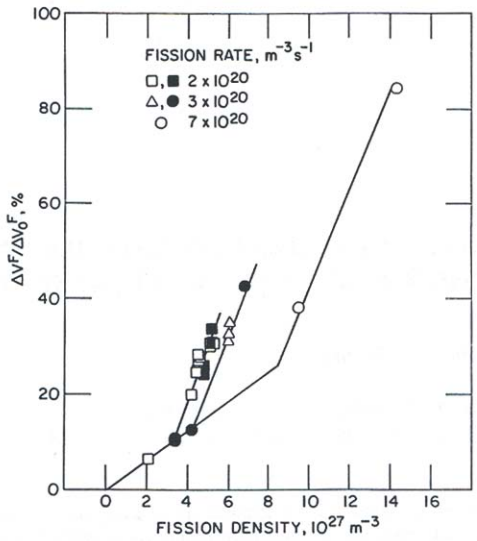

Figure 2.5: Calculated fractional gas release to grain boundary vs. fission density for three values of gas-atom re-solution rate.

alone would not significantly affect the position of a bubble peak and thus gas-bubble swelling. Sensitivity studies have also indicated that a large change (hypothetically many orders of magnitude instead of approximately linear) in bubble nucleation rate at higher doses would not affect fuel swelling appreciably.

A bubble population with an observed bubble diameter can only be calculated if microstructural features such as grain boundaries or dislocation networks are introduced. The driving force for recrystallization is the production of interstitial loops due to irradiation. The continued generation of interstitial loops induces an internal stress in the material which leads to strain in the form of lattice displacement. The initiation of recrystallization has been observed to occur predominately along the preexisting grain boundaries[24]. Subsequently, the recrystallization front moves toward the grain center eventually consuming the entire grain. Thus, the volume fraction of recrystallized material is a function of irradiation time as well as the initial grain size. As gas-bubble swelling is higher in the recrystallized material than in the unrecrystallized fuel, the swelling due to fission gas is a function of the recrystallization kinetics.

Analytical models for the progression of recrystallization, and for fuel swelling due to fission gas as a function of burn-up have been developed. The fission density F_d dependent concentration of viable recrystallization nuclei C_{rx} was determined as a function of the dislocation density ρ_d based on the concept of node pinning by irradiation-induced precipitates associated with fission-gas

bubbles[25] as

$$C_{rx} = \frac{9\left(f(v)\rho_d\right)^{7/2}}{8\pi^6\left(C_A C_\rho\right)^7 F_d^{5/2}}\left(\frac{\alpha_p}{\phi\gamma}\right)^2\sqrt{\frac{2\lambda}{3\pi b_v B_0\beta}} \quad , \tag{2.2.21}$$

where $\alpha_p/\phi\gamma$ is a factor composed of terms related to the production of precipitates and and sub-grain growth in the presence of precipitates, b_v is the van der Waals constant, λ is the atom knock-off distance, $f(v) = (1 - v/2)\,/\,(1 - v)$, v is Poisson's ratio, C_A is 3 for cubic cells, and C_ρ is within a factor of unity, β is the number of gas atoms produced per fission, and where, at the relatively low temperatures where irradiation-induced recrystallization occurs, the gas atom diffusivity is athermal and can be expressed as $D_g = D_0\dot{f}$. The temperature dependence of C_{rx} in Eq. (2.2.21) is contained in the interstitial and vacancy diffusivities. In general, these diffusivities are expressed as $D_i = D_i^0 \exp\left[-\varepsilon_i/kT\right]$ and $D_v = D_v^0 \exp\left[-\varepsilon_v/kT\right]$ where ε_i and ε_v are the interstitial and vacancy migration enthalpies, respectively.

The trigger point for recrystallization is defined as the point where the kinetically derived concentration of nuclei given by Eq. (2.2.21) becomes equal to the equilibrium number of nuclei, n_i^*, determined from thermodynamic considerations, i.e.

$$n_i^* = n_i^0 \exp\left[-\Delta G^*/kT\right] \quad , \tag{2.2.22}$$

where ΔG^* is the critical standard free energy that a node must acquire in order to recrystallize and, as the basic unit out of which the cellular dislocation network is composed is the interstitial loop, n_i^0 is taken to be the athermal component in the expression for the interstitial loop density

$$\begin{aligned} n_i^0 &= \left(\frac{\rho_1}{\pi d_1}\right)_{\text{Athermal}} \\ &= \frac{\rho^{3/2}}{\pi^{3/2} C_A C_\rho \sqrt{f(v)}} \exp\left[+\left(\varepsilon_v/2 - \varepsilon_i\right)/2kT\right] \quad . \end{aligned} \tag{2.2.23}$$

Equating Eqs. (2.2.21) and (2.2.22), using Eq. (2.2.23), and solving for F_d results in an expression for the critical fission density at which recrystallization will occur, F_{dx}

$$F_{dx} = \left(\frac{\alpha_p \rho_d}{\phi\gamma}\right)^{4/5} \left(\frac{2\lambda}{3b_v D_0 \beta}\right)^{1/5} \times \frac{f(v)^{6/5} \exp\left[4\left(\varepsilon_v/3 - \varepsilon_i\right)/15kT\right]}{\pi^{9/5}\left(C_A C_\rho\right)^{12/5}} \quad . \quad (2.2.24)$$

The fission density at which recrystallization is predicted to initiate as given by Eq. (2.2.24) is athermal and very weakly dependent on fission rate. As such, F_{dx} is independent of ε_v and ε_i and depends, primarily on the collision related parameters λ, D_g and $\alpha_p/\phi\gamma$.

Substituting nominal values of the parameters[25] in Eq. (2.2.24) leads to the simplified expression[2] for F_{dx}(m^{-3}):

$$F_{dx} = 4 \times 10^{24} (\dot{f})^{2/15} \quad , \quad (2.2.25a)$$

$$F_{dx} = 6 \times 10^{24} (\dot{f})^{2/15} \quad , \quad (2.2.25b)$$

where Eq. (2.2.25a) corresponds to UO_2 and Eq. (2.2.25b) to U-10Mo.

Progression of irradiation-induced recrystallization

A model for the progression of recrystallization as a function of burn-up has been developed based on the following assumptions: (1) recrystallization initiates at preexisting grain boundaries; (2) annuli of width δ, located initially adjacent to the original grain boundary, transform to defect-free regions via the creation of the new recrystallized surface when the volumetric strain energy exceeds that necessary to create the new surface; and, (3) the rate at which the defect front moves through the newly created defect-free annulus is proportional to the strain rate, which, in analogy with fission-induced creep, is proportional to stress and fission rate. The microscopic stress is a function of the lattice displacement, which is related to the generation rate of interstitial loops.

The original grain boundaries act as nucleation sites for the recrystallization transformation. Upon the initiation of recrystallization given by Eq. (2.2.24),

[2]Eqs. (2.2.23) - (2.2.25) are the corrected versions of Eqs. (32)-(34) in Ref. [25].

and the creation of the defect-free annulus adjacent to the ring of newly recrystallized material, the defects interior to the annulus are considered to be in a 'superheated' condition. These defects must travel through the denuded annulus in order to find appropriate nucleation sites required for the recrystallization transformation. The defects in the region interior to the defect-free annulus consist of a cellular dislocation network.

When dislocation loops are large enough relative to the inter-atomic distances, but small relative to the crystal dimensions, they produce a measurable lattice distortion that can be expressed as

$$\Delta a(t)/a_0 = \pi b_v n_1(t) d_1^2(t)/12 \quad . \tag{2.2.25}$$

The increase in the lattice parameter is the driving force for irradiation-induced recrystallization. Recrystallization occurs when the strain energy density, ΔU, in an annulus of width δ is greater than the energy required to create a new surface, i.e.

$$4\pi r^2 \delta \Delta U = 4\pi r^2 \gamma_{gb} \quad , \tag{2.2.26}$$

and

$$\Delta U = \frac{1}{2}\left(\frac{\Delta a}{a_0}\right)^2 E \quad , \tag{2.2.27}$$

where E is the bulk modulus of the material. Thus,

$$\delta = \frac{2\gamma_s \theta}{E\left(\Delta a/a_0\right)^2} \quad , \tag{2.2.28}$$

where γ_s is the surface energy and θ is the boundary dihedral angle which is given by

$$\theta = 2\tan^{-1}\left[b_v\sqrt{\rho_d/2}\right] \approx 2b_v\sqrt{\rho_d/2} \quad , \tag{2.2.29}$$

where ρ_d is the dislocation density. The progression of recrystallization is assumed to occur in the following sequence of events: (1) subsequent to the formation of the new surface the annulus is cleared of defects; (2) the defect front

interior to the annulus is driven through the cleared annulus by stress generated by defect-induced lattice displacement; (3) the strain rate is proportional to stress and fission rate (analogous to fission-induced radiation creep).

The time for the recrystallization front to move a distance $d_g/2 - r(t)$ from the surface of a spherical grain of diameter d_g is given by

$$t_r = \frac{[d_g/2 - r(t)]}{v_{df}} \quad , \tag{2.2.30}$$

where v_{df} is the speed of the defect front through the annulus. The volume fraction of recrystallized fuel as a function of time can be expressed as

$$V_r = 1 - \left(\frac{2r(t)}{d_g}\right)^3 \quad , \tag{2.2.31}$$

and using Eq. (2.2.30)

$$V_r = 1 - \left[1 - \frac{2v_{df}t}{d_g}\right]^3 \quad . \tag{2.2.32}$$

It is here assumed that v_{df} is proportional to the strain rate, i.e.

$$v_{df} = \delta\dot{\varepsilon} \quad , \tag{2.2.33}$$

where the strain is given by

$$\dot{\varepsilon} = B_2\dot{f}\sigma \quad , \tag{2.2.34}$$

and the stress is a function of the lattice displacement

$$\sigma = E\frac{\Delta a}{a_0} \quad . \tag{2.2.35}$$

The progression of recrystallization occurs after the cellular dislocation network has formed. Thus, from Eq. (2.2.25)

$$\Delta a/a_0 = \frac{b_v C_a C_\rho}{12}\sqrt{\frac{\pi}{f(v)}}\rho_d^{1/2} \quad , \tag{2.2.36}$$

where

$$\rho_d = \pi n_1 d_1 \quad , \tag{2.2.37}$$

and the lowest energy configuration is a cellular dislocation network with cell size given by[26, 27]

$$d_1 = C_A C_\rho \sqrt{\frac{\pi}{\rho_d f(v)}} \quad . \tag{2.2.38}$$

Using Eqs. (2.2.33) and (2.2.34) and solving for v_{df}

$$v_{df} = \delta\dot{\varepsilon} = \delta B_2 \dot{f}\sigma \quad . \tag{2.2.39}$$

Using Eqs. (2.2.28) and (2.2.35),

$$v_{df} = \frac{2\gamma_s\theta}{E\left(\Delta a/a_0\right)^2} B_2 E \frac{\Delta a}{a_0}\dot{f} = \frac{2\gamma_s 2b_v\sqrt{\rho_d/2}}{\Delta a/a_0} B_2 \dot{f} \quad , \tag{2.2.40}$$

and using Eq. (2.2.36)

$$v_{df} = \frac{2\gamma_s 2b_v\sqrt{\rho_d/2}}{\frac{b_v C_a C_\rho}{12}\sqrt{\frac{\pi}{f(v)}}\rho_d^{1/2}} B_2\dot{f} = \frac{48\gamma_s B_2}{C_A C_\rho}\sqrt{\frac{f(v)}{2\pi}}\dot{f} \quad . \tag{2.2.41}$$

The volume fraction of recrystallized fuel as a function of fission density is then given by

$$V_r = 1 - \left[1 - \frac{2v_{df}t}{d_g}\right]^3 \quad , \tag{2.2.42}$$

or after substituting Eq. (2.2.41) for v_{df}

$$V_r = 1 - \left[1 - \frac{96\gamma_s B_2 \left(F_d - F_{dx}\right)}{d_g C_A C_\rho}\sqrt{\frac{f(v)}{2\pi}}\right]^3 \quad , \tag{2.2.43}$$

and can be approximated to

$$V_r \approx \frac{288\gamma_s B_2 \left(F_d - F_{dx}\right)}{d_g C_A C_\rho}\sqrt{\frac{f(v)}{2\pi}} \ , \ F_d \ll F_d^{\max} \quad , \tag{2.2.44}$$

where

$$F_d = \dot{f}t \ ; \quad F_{dx} = \dot{f}t_x \quad , \tag{2.2.45}$$

and t_x is the time at which recrystallization is initiated.

Thus, from Eq. (2.2.44), for $F_d \ll F_d^{\max}$ the volume fraction of recrystallized fuel is proportional to the fission density and inversely proportional to the grain size. In addition. $V_r(t)$ is independent of fuel temperature.

Effect of recrystallization on fuel swelling

Prior to the onset of recrystallization, the fractional swelling is due to the accumulated fission gas given by Eq. (2.2.20), reprinted here

$$\frac{\Delta V}{V} = \frac{c_g a^3}{4} + \frac{4\pi}{3}\left(r_b^3 c_b + \frac{3R_b^2 C_b^V}{d_g}\right) \quad .$$

Once recrystallization has been initiated, i.e. using Eq. (2.2.24), fuel swelling consists of two components,

$$\left(\frac{\Delta V}{V}\right)_T = (1 - V_r)\left(\frac{\Delta V}{V}\right)_g + V_r\left(\frac{\Delta V}{V}\right)_{gx} \quad , \tag{2.2.46}$$

where $\left(\frac{\Delta V}{V}\right)_g$ is given by Eq. (2.2.20), and $\left(\frac{\Delta V}{V}\right)_{gx}$ is given by

$$\left(\frac{\Delta V}{V}\right)_{gx} = 4\pi R_{bx}^3\left(\frac{C_b^V}{d_g} + \frac{C_{bx}^V}{d_{gx}} + \frac{1}{3d_{gx}^3}\right) \quad . \tag{2.2.47}$$

In Eq. (2.2.47) it has been assumed that upon recrystallization the preexisting density of bubbles on the boundaries, C_b^V, remains relatively unchanged. A new population of bubbles, C_{bx}^V is formed and is given by Eq. (2.2.13) with the as-fabricated grain size, d_g, replaced by the recrystallized grain size, d_{gx}. The term $1/d_{gx}^3$ represents the density of triple points per unit volume. The triple point nodes are considered very efficient sinks an as such it assumed that a gas bubble will form at each node. It has also been assumed in Eq. (2.2.47) that the radius, R_{bx} of the preexisting grain boundary bubbles, the newly formed bubbles and triple point bubbles are approximately the same.

R_{bx} is given by Eq. (2.2.19) with N_b replaced by N_{bx} where

$$N_{bx} = \frac{V_r\beta\dot{f}t}{3\left(\frac{C_b^V}{d_g} + \frac{C_{bx}^V}{d_{gx}} + \frac{1}{3d_{gx}^3}\right)} \quad . \tag{2.2.48}$$

In Eq. (2.2.48), it has been assumed that in the recrystallized region of the fuel the majority of the generated gas is on the grain boundaries. This assumption is consistent with the fractional gas release calculated using Eq. (2.2.11) for $4\pi^2 D_g t/d_g^2 > 1$.

2.2.4 High temperature

The high temperature operating regime can be described with the same set of expressions used in the low temperature regime. The mechanisms described in the previous sections for low temperatures (e.g. irradiation-induced re-solution, gas-atom diffusion, bubble nucleation) operate in a fundamentally similar way at high temperatures. However, some mechanisms will be very weak, or non-existent at the higher temperatures (e.g. irradiation-induced re-crystallization). Others, which are not observed in the low-temperature regime

will dominate the way the fuel behaves at higher temperatures (e.g. biased bubble motion in a temperature gradient, grain-growth/grain-boundary sweeping). Therefore, to account for the phenomenological differences in these two regimes, it is necessary to understand the temperature dependence of the full complex of bubble behavioral mechanisms.

High temperatures are generally defined as any temperature higher than half the melting temperature, T_m, of the fuel under discussion. At this temperature higher atomic and bubble mobilities due to thermal diffusion (as compared to athermal diffusion) take on a more prominent role, while grain-growth and grain-boundary sweeping are also stimulated in a high temperature environment. Increased swelling at high temperatures is primarily due to increased bubble mobilities leading to enhanced bubble coalescence. On the other hand, in fuels that experience enhanced pore interconnection at higher temperatures, the gas-driven fuel swelling will be limited due to higher fractional gas release.

Thermal diffusion is an important contribution to fuel swelling at higher temperatures. Diffusion is responsible for the mobility of atoms and assists in bubble nucleation and coalescence. Similarly, at higher temperature/temperature-gradient conditions, fission gas bubbles gain the ability to move and migrate to the boundaries where lower re-solution rates enhance bubble coalescence.

For general conditions, within the Rest Models, the gas-atom diffusion coefficient is generally given by the conventional Arrhenius relation

$$D_g = D_0 \exp\left[\frac{\Delta H}{kT}\right] \quad , \tag{2.2.49}$$

where D_0 is a preexponential term (in $\text{cm}^2 \cdot \text{s}^{-1}$), ΔH is the activation enthalpy, k is Boltzmann's constant and T is the absolute temperature. In particular, the *FASTGRASS* model uses a diffusion coefficient given by

$$D_g = 2.1 \times 10^{-4} \exp\left[\frac{-91,000}{kT}\right] \ \text{cm}^2 \cdot \text{s}^{-1} \quad , \tag{2.2.50}$$

where k is given in cal/K.

Surface diffusion provides an upper limit for bubble mobility. Observations (out-of-pile experiments) reveal bubble mobilities substantially lower than that given by the surface diffusion mechanism. Bubble diffusivities lower than those calculated with a surface diffusion mechanism may be due to factors such as facet nucleation and interaction of the jumping ad-atoms with the gas

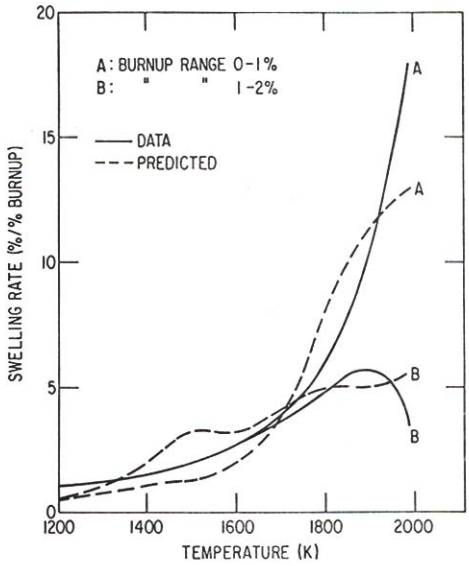

Figure 2.6: Predicted swelling rates as a function of fuel temperature, compared with the data of Zimmerman[28] for burnups of 0-1% and 1-2%.

atoms in the bubble. Therefore, an empirical bubble diffusion coefficient is used and is given by

$$D_b = \frac{1.468 \times 10^{-11} \exp\left[\dfrac{-108,000}{kT}\right]}{R_b^{2.09}} \ \mathrm{cm}^2 \cdot \mathrm{s}^{-1} \quad . \tag{2.2.51}$$

Figures 2.6 and 2.7 show predicted rates of swelling due to retained fission gas as a function of irradiation temperature using *FASTGRASS* , compared with the results obtained by Zimmerman[28], for UO_2 fuel irradiated over the burn-up ranges of 0-1, 1-2, 2-3 3-4 and 4-5 at.%. Zimmerman[28] obtained the swelling results shown in Figs. 2.6 and 2.7 by comparing the external volume changes of the UO_2 fuel with calculated values for UO_2 densification (i.e., irradiation-enhanced sintering of oxide fuel). In general, the predicted swelling rates obtained with *FASTGRASS* agree reasonably well with the results obtained by Zimmerman[28].

Figure 2.6 shows a very strong temperature dependence of the swelling at low burnups. However, with increasing burn-up (Fig. 2.7), the swelling rate and temperature dependence diminish, owing to saturation of the fission-gas swelling rate caused by the enhanced release of fission gas at increased values

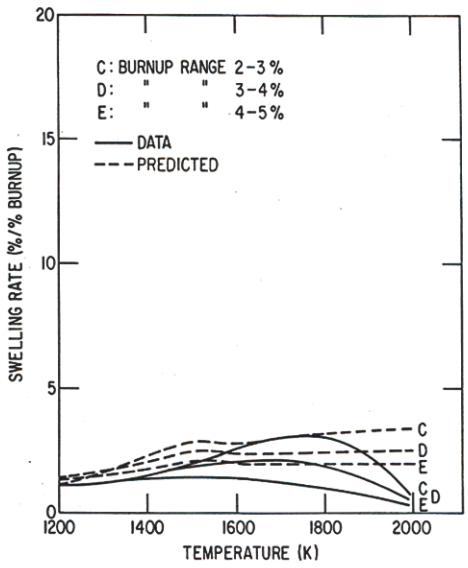

Figure 2.7: Predicted swelling rates as a function of fuel temperature, compared with the data of Zimmerman[28] for burnups of 2-3%, 3-4% and 4-5%.

of fuel burn-up.

As mentioned above, fuel behaviors such as grain-growth/grain-boundary sweeping and microcracking tend to influence swelling at higher temperatures. However, these mechanisms are generally observed as a result of sharp temperature spikes common to transient, or off-normal, operating conditions. For that reason, their effects on the fuel element, including swelling, will be discussed in Chapter 5.

2.3 Fission gas release

An important part of nuclear reactor design relies on a sound understanding of fission gas release from the irradiated nuclear fuel. Fission gas release is a measure that not only takes into account gas released into the fuel–cladding gap, but also gas that travels to the central void and open porosity sites (e.g., cracks and interlinked gas bubbles) within the fuel[1]. Gaseous fission products can be grouped into two major categories consisting of the noble gases xenon (Xe) and krypton (Kr) (although Xe is generated in much larger proportions than Kr) and volatile fission products (VFP) such as cesium (Cs), iodine (I), tellurium (Te), barium (Ba) and strontium (Sr).

The mechanism for fission gas release has been covered throughout the present work. The mechanisms that drive the release of fission gases are similar to those responsible for swelling. Generally, the swelling process continues until grain boundary bubble interlinkage forms on the grain faces (cf. §2.1.3) leading to short-circuit paths for gas atom venting to the grain edge. At the grain edge, extensive bubble interlinkage can form long tunnels that channel fission gases to the surface or other free volumes in the fuel. In *FASTGRASS* the model for calculating the probability of long-range grain-edge bubble interconnection is a function of grain-edge bubble swelling. To account for local fluctuations in fuel microstructure and gas-bubble morphology, the grain-edge-porosity interlinkage fraction, F, is assumed to be a statistical distribution around an average value of the grain-edge swelling, B_{vedge} given by Eq. (2.1.9) in §(2.1.2).

At low temperatures ($\ll 0.5\mathrm{T}_m$) gas atom diffusion is athermal and mobility is minimal making migration to the surface or porosity unlikely. In this regime, most of the vented gas occurs close to the surface as a result of recoil or fission fragment knockout[1]. Gas release by either of these processes is nominal.

High temperature gas release can be divided into two primary temperature ranges. At temperatures between 1300 and $\sim 1900^{\circ}$K in UO_2 , for example, gas release is determined by thermal diffusion of gas atoms to the surface and although the temperature gradient is generally not strong enough for gas bubbles to move, long-range bubble interlinkage may occur and provide another venting channel. When temperatures increase above 1900°K gas bubbles and closed pores can move through the fuel along the temperature gradient and vent directly to the surface or other free volume spaces[1].

The total contribution to fission gas release, g, is calculated in *FASTGRASS* by the following expression

$$\frac{\mathrm{d}g}{\mathrm{d}t} = \left(\frac{V_f \sqrt{14}}{d_g} C_f + \frac{P_A C_f}{t} \right) P_I + C_e \frac{\mathrm{d}P_I}{\mathrm{d}t} + V_f \varkappa C_f \quad . \tag{2.3.1}$$

For a multinode calculation, the various gas release contributions from each individual node, given by Eq. (2.3.1), are summed up to obtain the total gas released during time t. The total contribution of gas released due to long-range migration of fission gas bubbles up the temperature gradient depends on the cross-sectional area of the inner or outer node depending on the direction of the gradient which bounds a free surface. The velocity of the grain-face bubbles is given by V_f

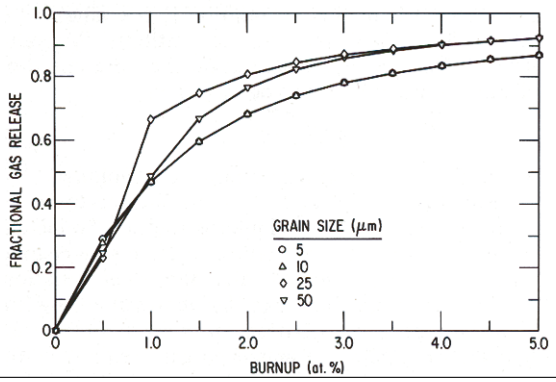

Figure 2.8: The *FASTGRASS* predictions of fission-gas release vs. burn-up for various grain sizes with an average irradiation temperature and temperature gradient of 2000 K and 1000 K/cm, respectively.

2.3.1 Grain size effects on gas release

With larger grains, it is topologically easier to find a path to the plenum from the fuel interior via the edge tunnels, and gas release from the grain edges is therefore greater. At higher temperatures, the grain-edge gas-bubble swelling increases; as the grain-edge interconnection probability, Eq. (2.1.9), is a function of the edge-bubble swelling, this leads to increased edge-tunnel interlinkage and fission-gas release.

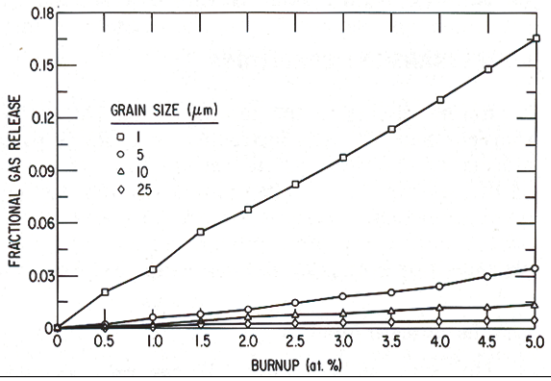

Figure 2.9: The *FASTGRASS* predictions of fission-gas release vs. burn-up for various grain sizes with an average irradiation temperature and temperature gradient of 1200 K and 1000 K/cm, respectively.

Figure 2.8 shows *FASTGRASS* -predicted gas release at 2000 K as a function of burn-up and grain size. In general, *FASTGRASS* predicts an increase in gas release at this temperature with increasing grain size and burn-up. Evidently,

the effect of longer intragranular diffusion times for larger grains is overridden at 2000 K by the intergranular factors mentioned above. Note that *FASTGRASS* results tend to indicate grain-size-independent gas release at high burn-up, as would be expected once equilibrium release has been established. Figure 2.9 is a *FASTGRASS* plot of release versus burn-up at 1200 K as a function of grain size. Generally, gas release decreases with increasing grain size because intragranular diffusion is rate controlling at this lower temperature.

Figure 2.10 summarizes the effects of varying grain size on gas release in the temperature range from 1200 to 2400 K. Gas release is plotted as a function of temperature and grain size at 3 at.% burn-up. Around 1800 K (as predicted by *FASTGRASS*), there is a change in the relative importance of the mechanisms determining gas release. Below this range, lattice diffusion times are comparatively small, transport from the faces and edges is the dominant factor, and gas release increases with increasing grain size.

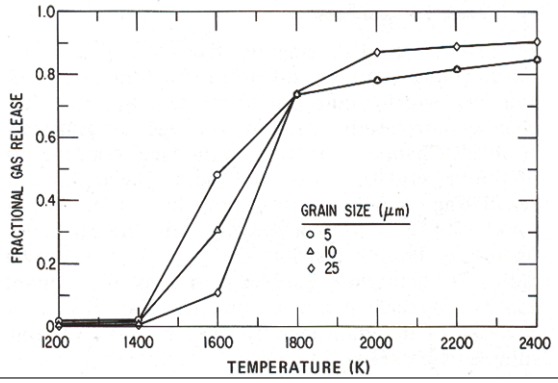

Figure 2.10: The *FASTGRASS* predictions of fission-gas release vs. fuel temperature for various grain sizes with a fuel burn-up and average temperature gradient of 3 and 1000 K/cm, respectively.

2.3.2 Validation of the *FASTGRASS* model for fission-gas release

Figure 2.11 shows predicted fractional release of the stable fission-gases as a function of time and compares it with the isothermal release data for ^{133}Xe from Ref. [29]. The three predicted curves reflect the ± 40 K uncertainty in irradiation temperature. The agreement between prediction and data is good. It should be noted that *FASTGRASS* currently calculates the behavior of fission-gases, and a comparison between the predicted fractional releases of stable gases and data for ^{133}Xe (with a 5.25-day half-life) may be affected by qualitative and quantitative differences in behavior between the stable gases and

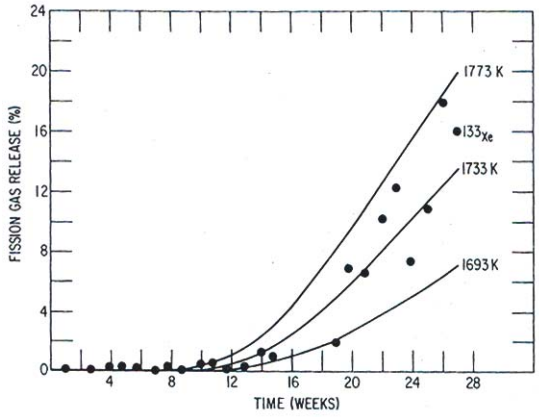

Figure 2.11: Predicted fractional release of the total stable noble gases at 1733 ± 40 K (solid curves), compared with ^{133}Xe data of Turnbull and Friskney[29] (symbols).

^{133}Xe. The fact that the data for ^{133}Xe release follow the predicted release of the stable gases supports the proposition that the stable fission-gases play a major role in establishing the interconnection of escape routes from the interior to the exterior of the nuclear fuel. (These escape routes are also essential channels for VFP transport and venting. The detailed workings of this mechanism will be discussed in Chapter 6.) After steady-state concentrations of ^{133}Xe have been achieved (presumably within the first 10-12 weeks of irradiation and prior to any substantial bubble interlinkage), the ^{133}Xe follows any pathway to the fuel exterior that have been created by the stable gases and is released.

The theory accurately describes fission-gas saturation effects in that very little gas release is predicted (and observed) to occur prior to $\sim$12 weeks of irradiation. At $\sim$12 weeks of irradiation, the grain faces are saturated with fission-gas, leading to interconnection and release. Subsequent to gas release the face channels 'heal' and the accumulation of gas on the boundaries begins anew. This physical picture of gas behavior on the grain faces is consistent with experimental observations[30].

Figure 2.12 shows predicted fission-gas release as a function of fuel burn-up, and compares these results with the data of Zimmermann[28]. Uranium dioxide fuel with a fission rate of 10^{14} fissions $\cdot$ cm$^{-3} \cdot$ s^{-1} was used in these experiments. A temperature gradient of $1000°$C $\cdot$ s^{-1} and grain diameters between 1 and 10-μm were used for the calculation. Four different sets of calculated curves were generated using average fuel temperatures of 1250, 1500, 1750 and 2000 K. The use of relatively small grain diameters for the calculation of the low-temperature Zimmerman data agrees with the results obtained by other authors[31]. Presumably the use of relatively small "effective" grain diameters

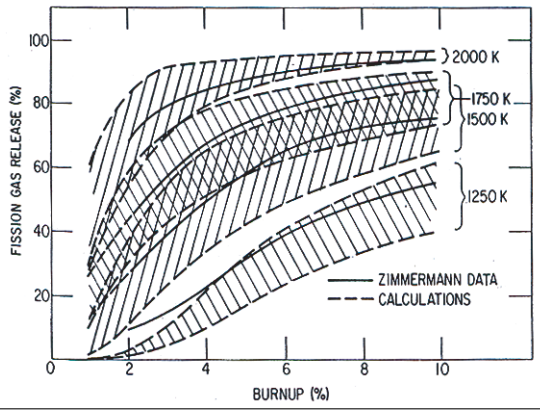

Figure 2.12: Predicted fractional fission-gas release at 1250, 1500, 1750 and 2000 K (dashed curves), compared with the data of Zimmerman[28] (solid curves).

is required in order to simulate, to some degree, subgrain-boundary formation which may have occurred in this fuel[32]. The 1250 and 1500 K data are bracketed by predictions based on 2.5 and 5-μm, and 5 and 10-μm grain sizes, respectively. Again, agreement between theory and data is reasonable.

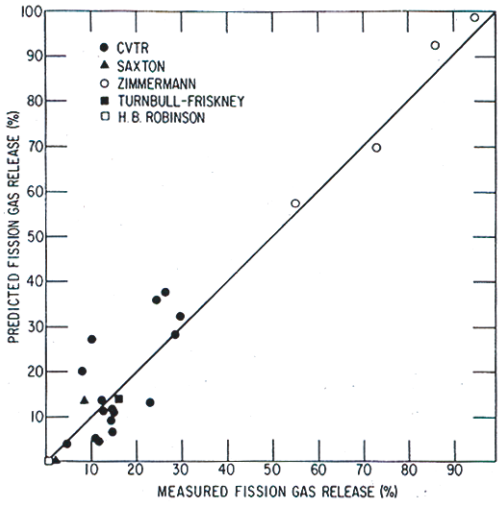

Figure 2.13: Comparison of theoretical predictions with end-of-life gas release.

Figure 2.13 shows calculated end-of-life gas release for fuel irradiated in the Carolinas-Virginia Tube Reactor (CVTR), the H.B. Robinson (HBR) No. 2 Reactor and the Saxton Reactor, compared with the measured values. Also shown in Fig. 2.13 are the predicted and measured end-of-life releases for the Turnbull[29] and Zimmerman[28] experiments. The diagonal line indicates perfect agree-

ment between theory and experiment. To supply *FASTGRASS* with the proper operating conditions for the CVTR, HBR and Saxton irradiations, *FASTGRASS* was coupled to and experimental LWR fuel behavior code generated by making suitable modifications[33] to the LIFE fuel performance code. As is evident from Fig. 2.13, the theory predicts the data reasonably well for fission-gas release between 0.2 and $\sim 100\%$ and for burnups between 0.7 and 10 at.$\%$ ($\sim 7000-100000$ MWd/tM). The largest differences between predictions and measurements occur for the CVTR irradiations. These differences are attributed to uncertainties in power history and to uncertainties in the LIFE calculation of fuel temperatures.

Chapter 3

DART: Dispersion Analysis Research Tool

The Dispersion Analysis Research Tool (*DART*) code is a dispersion fuel analysis code that contains mechanistically-based fuel and reaction-product swelling models, a one dimensional heat transfer analysis and mechanical deformation models. *DART* has been used to simulate the irradiation behavior of uranium oxide, uranium silicide and uranium molybdenum aluminum dispersion fuels, as well as their monolithic counterparts.

One of the main uses of *DART* is that of a research tool that can be used to extract information on the fundamental properties (under irradiation) of the dispersion/monolithic fuels. Based on the theoretical foundation underlying *DART* , application of the code to the interpretation of detailed experimental information (e.g., bubble-size distributions) can yield commensurate materials properties (e.g., diffusion coefficients, viscosity of fuel and/or reaction product) due to the direct connection between the "calibration parameters" and the physical properties of the material.

The thermal-mechanical *DART* code has been validated against RERTR tests performed in the ATR for irradiation data on interaction thickness, fuel, matrix and reaction-product volume fractions, and plate thickness changes. The *DART* fission gas behavior model has been validated against UO_2 fission-gas release data as well as measured fission-gas-bubble distributions.

DART contains models for irradiation-induced recrystallization and the effect of such phenomena on swelling and gas release at high burnup.

The *DART* mechanical model includes the constraining effects of the aluminide

shell that is formed by the interdiffusion of the fuel and the matrix aluminum. The *DART* mechanical (stress) model consists of a fuel sphere that deforms because of swelling of both the solid fission products and the fission gas bubbles. An aluminum matrix shell that is assumed to behave in a perfectly plastic manner and which deforms by yielding to expansion of fuel particle volume surrounds the fuel sphere.

DART can account for the formation of amorphous reaction products and/or fuel (e.g., irradiation-induced amorphization) and for the calculation of gas-bubble swelling in the amorphous material.

The previous chapter dealt with models calculated within the formality of *FASTGRASS* . As discussed in §1.2.2, *FASTGRASS* uses a fast-processing algorithm that tracks the evolution of the density peaks of the average size bubble. At this point we make a transition, as the *DART* code is modeled after the *GRASS-SST* calculation scheme, where the size and concentration of a distribution of bubbles is considered. This type of formalism demands a higher processing payload, but for materials where the bubble size distributions have been measured, this code has a higher validation accuracy; in other words, the viability of the models describing the underlying physics can be more stringently tested. The details of the distribution algorithm are found in §3.2.

3.1 Mechanical model

The *DART* mechanical analysis addresses the deformation behavior of dispersion fuel plates, tubes and fuel rods. The elastic stress and strain distributions are relatively simple to obtain, particularly since the loading is usually reasonably symmetric. The solution in the elasto-plastic range, however, become complicated, so simplifying assumptions of various types are made. These involve assuming the material incompressible in both the elastic and plastic ranges and assuming it perfectly plastic in the plastic range. With these assumptions, closed-form solutions can be obtained[34, 35]. The model employs a system of spherical fuel particles surrounded by a large spherical shell of matrix material that is bonded to an outer shell of aluminum cladding. The *DART* swelling models provide the driving force for mechanical deformation. The model used to calculate the stress gradient across the fuel particle is derived directly from the equations of equilibrium, compatibility, strain displacement and the constitutive equations (stress-strain relationships), coupled with the assumption of incompressibility of plastic strain. The boundary conditions assume finite radial stresses at the center of the inner sphere, no discontinuity in the radial stress at the fuel/matrix interface, and no pressure on the outer surface of the spherical shell. It is also assumed that swelling of the matrix aluminum is not a function of radial position and that the outer radius of the

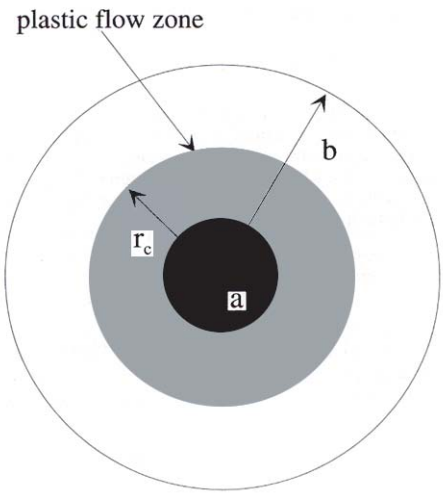

Figure 3.1: The model consists of the stress analysis of a hard sphere of radius a assumed to behave in an elastic manner, surrounded by a spherical shell with outer radius b of a softer material that is assumed to behave in a perfectly plastic manner ($b \gg a$).

spherical shell approaches infinity. This approach is based on calculations that indicate temperature changes across the fuel particles are small.

The model consists of the stress analysis of a "hard" sphere of radius a assumed to behave in an elastic manner, surrounded by a spherical shell with outer radius b of a "softer" material that is assumed to behave in a perfectly plastic manner ($b \gg a$).

This plastic behavior is assumed to extend out to a plastic radius r_c such that $a < r_c < b$. This procedure yields an equation for the interfacial pressure (radial stress) at the fuel/matrix interface in terms of fuel particle swelling and plastic deformation in the matrix. As the interfacial pressure increases, plastic flow is induced in the matrix out to some radius beyond which only elastic deformation occurs (Fig. 3.1).

3.1.1 Mechanical model in the presence of aluminide formation

As discussed above, the *DART* mechanical (stress) model consists of a fuel sphere that deforms because of swelling of both solid fission product and fis-

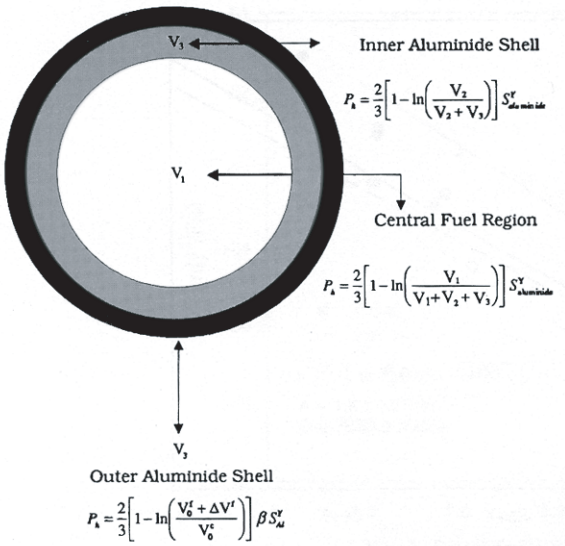

Figure 3.2: Cross-sectional schematic representation of fuel particle nodalization.

sion gas bubbles. An aluminum matrix shell surrounds the fuel sphere, which is assumed to behave in a perfectly elastic manner and which deforms (yields) when fuel particle volume expands. The effects of cladding are included by a suitable adjustment of the effective aluminum volume fraction. Currently, the effects of creep are not explicitly included; instead, lowering the aluminum yield stress to an effective value approximates the stress relaxation. Deformation of the matrix and cladding material generates stresses within the expanding fuel particles, which affect the swelling rate of the fission gas bubbles. The swelling fuel particles push the matrix aluminum into as-fabricated porosity and simultaneously cause cladding deformation.

The interaction between the matrix aluminum and the fuel particle discussed in Section IV of Ref. [36] leads to the formation of an aluminide shell that surrounds the fuel particle that grows with time. The aluminide shell acts as an additional restraint against fuel particle swelling for the following reasons. For the case where the fuel is amorphous (e.g., irradiated U_3Si_2), the aluminide shell formed by interaction of the fuel with the matrix aluminum is crystalline and swells at a much lower rate[37] than the amorphous material that is encompassed by the shell. In addition, the crystalline aluminide is intrinsically stronger than the softer amorphous material. For the case of U_3Si where the fuel has undergone recrystallization[38], the aluminide shell deforms at a lower rate than the recrystallized material that it surrounds. Furthermore, uranium aluminide may be intrinsically stronger than uranium silicide.

The fuel particle is nodalized as shown schematically in Fig. 3.2. A balance between the level of calculational accuracy and *DART* code running time determines the selection of the number of particle nodes. Initially, before the outer node becomes an aluminide, the stress within the fuel particle is determined by solving the following expression[36]

$$P_h = \frac{2}{3}\left[1 - \ln\left(\frac{V_0^f + \Delta V^f}{V_0^c}\right)\right]\beta S_{\text{Al}}^Y \quad , \tag{3.1.1}$$

where P_h is the hydrostatic stress within the fuel particle, V_0^f/V_0^c is the as-fabricated fuel volume fraction in the core, $\Delta V^f/V_0^c$ is the increase in fuel volume fraction due to processes such as closure of as-fabricated pores and fuel particle swelling, β is a phenomological factor that has been introduced to account for the effects of irradiation (e.g. irradiation induced creep and hardening) and finally, S_{Al}^Y is the aluminum matrix yield stress. The depth, y, of the reaction layer as given by Ref. [36] is

$$y = \sqrt{[D_{\text{rad}} + D_{\text{thermal}}]\, t} \quad , \tag{3.1.2}$$

where D_{rad} is the irradiation enhanced diffusion coefficient found in Section IV of Ref. [36], and D_{thermal} is the thermal coefficient. When the value of y is greater than or equal to the thickness of the outermost fuel node, that node is considered an aluminide, and the fuel particle swelling and total fuel meat swelling are updated accordingly. The fuel particle swelling is used to determine the evolution of the fuel, matrix and as-fabricated pore volume fractions. Subsequent to the conversion of the outermost node to an aluminide structure, the stress in this node is still determined by solving Eq. (3.1.1). To calculate the stress in the inner nodes, an assumption is made that this stress can be estimated by solving Eq. (3.1.1), but with the fuel volume fraction replaced by the ratio $vfma$ of the volume of unreacted fuel to the total fuel particle volume, and with the effective matrix aluminum yield stress replaced with the effective yield stress $S_{\text{aluminide}}^Y$ of the aluminide; i.e.,

$$P_h = \frac{2}{3}\left[1 - \ln\left(vfma\right)\right] S_{\text{aluminide}}^Y \quad . \tag{3.1.3}$$

The effective aluminide yield stress concept gives a strain that is proportional to stress (and proportional to dose), a result that is characteristic of irradiation-enhanced creep processes in the steady-state creep regime.

When y is greater than or equal to the thickness of the two outermost fuel nodes, the stress in the inner of these two outermost nodes is calculated by utilizing the effective yield stress concept as given by Eq. (3.1.3), but with $vfma$ equal to the ratio of the volume of the innermost aluminide node to the total volume of the two aluminide nodes. More generally, as more nodes are converted to an aluminide, the stress in an interior aluminide node k is given by Eq. (3.1.3) with $vfma$ equal to the ratio of the volume of the k^{th} aluminide node to total volume of the aluminide within the particle.

The stress in the inner fuel region (i.e., fuel that has not been converted to an aluminide) is given by Eq. (3.1.3), with $vfma$ equal to the ratio of the volume of the unreacted fuel to the total volume of the fuel particle.

It is clear that the correct implementation of this algorithm for calculating stresses within the fuel particle is dependent on the maintenance of the constraining relationship given by

$$\frac{r_c^3}{b^3} \ll 1 \quad , \tag{3.1.4}$$

where r_c is the radius that originates at the center of the fuel particle and stretches to the end of the plastic zone and b is the radius of the perfectly plastic outer shell of the fuel particle discussed in the above. Equation (3.1.4) can be satisfied by assuming that the plastic radius extends only a relatively short distance into the aluminide shell so that most of the aluminide shell deforms elastically.

3.2 *DART* calculational algorithms

The *DART* code predicts atomic and bubble behavior of fission gas in aluminum dispersion fuels under steady-state and transient conditions. Included are models that assess the effects of fission-product generation, gas-atom migration, bubble nucleation and re-solution, bubble migration and coalescence, channel formation on the grain faces, porosity interlinkage on grain edges, the existence of a fixed density of nodes that are identified as grain-edge corners or triple points, and fission-gas-bubble behavior in irradiated amorphous materials on both the amount of released fission products and on their distribution within the fuel. *DART* solves a set of coupled nonlinear differential equations for the intra and intergranular concentrations of fission-product atoms and gas bubbles. These equations are of the form

$$\frac{\mathrm{d}C_i^\alpha}{\mathrm{d}t} = - a_i^\alpha C_i^\alpha C_i^\alpha - b_i^\alpha C_i^\alpha + e_i^\alpha$$
$$(i = 1, \ldots, N;\ \alpha = 1, 2, 3, 4) \quad , \tag{3.2.1}$$

where C_i^α is the number of α-type bubbles in the i^{th}-size class per unit volume; $\alpha = 1, 2, 3, 4$ represents the lattice, dislocation, grain-face, and grain-edge distributions, respectively; and the coefficients a_i^α, b_i^α and e_i^α obey functional relationships of the form

$$a_i^\alpha = a_i^\alpha \left(C_i^\beta \right)$$

and

$$b_i^\alpha = b_i^\alpha \left(C_i^\beta, \ldots, C_{i-1}^\beta, C_{i+1}^\beta, \ldots, C_N^\beta \right) \quad . \tag{3.2.2}$$

The variables in Eq. (3.2.1) are defined in Table 3.1. The quantity a_i^α represents the rate at which α-type bubbles are lost from (grow out of) the i^{th}-sized class because of coalescence with bubbles in that class; b_i^α represents the rate at which α-type bubbles are lost from the i^{th}-sized class because of coalescence with bubbles in other size classes, migration out of the structural region, change in bubble type (i.e., by acquiring a different value of α) due to bubble migration processes and re-solution; and e_i^α represents the rate at which bubbles are being added to to the i^{th}-sized class because of fission gas generation, bubble nucleation, and bubble growth that is a result of bubble coalescence, migration processes, and bubble shrinkage due to gas-atom re-solution.

The fuel plate, rod or tube geometry is nodalized across the two dimensions (l, j) to characterize temperature and fission rate gradients. Within a particular fuel plate, rod or tube node (l, j), and within a particular fuel particle node (l, j, k), the sequence of *DART* calculations is illustrated in Fig. 3.3. As shown in Fig. 3.3, the calculation of stress is only "weakly" coupled to the swelling calculation. The primary advantage to adopting the effective aluminide yield stress concept is the implementation of a weak coupling approach to the swelling strain calculations. This procedure avoids the much more complicated and CPU intensive time-dependent deformation analysis. The philosophy adopted here is that the currently available data support the use of the effective-aluminide-yield stress concept. In addition, the basis of this concept is physical in that its implementation gives a strain that is proportional to stress (and proportional to dose), which is characteristic of irradiation-induced creep processes in the steady-state regime.

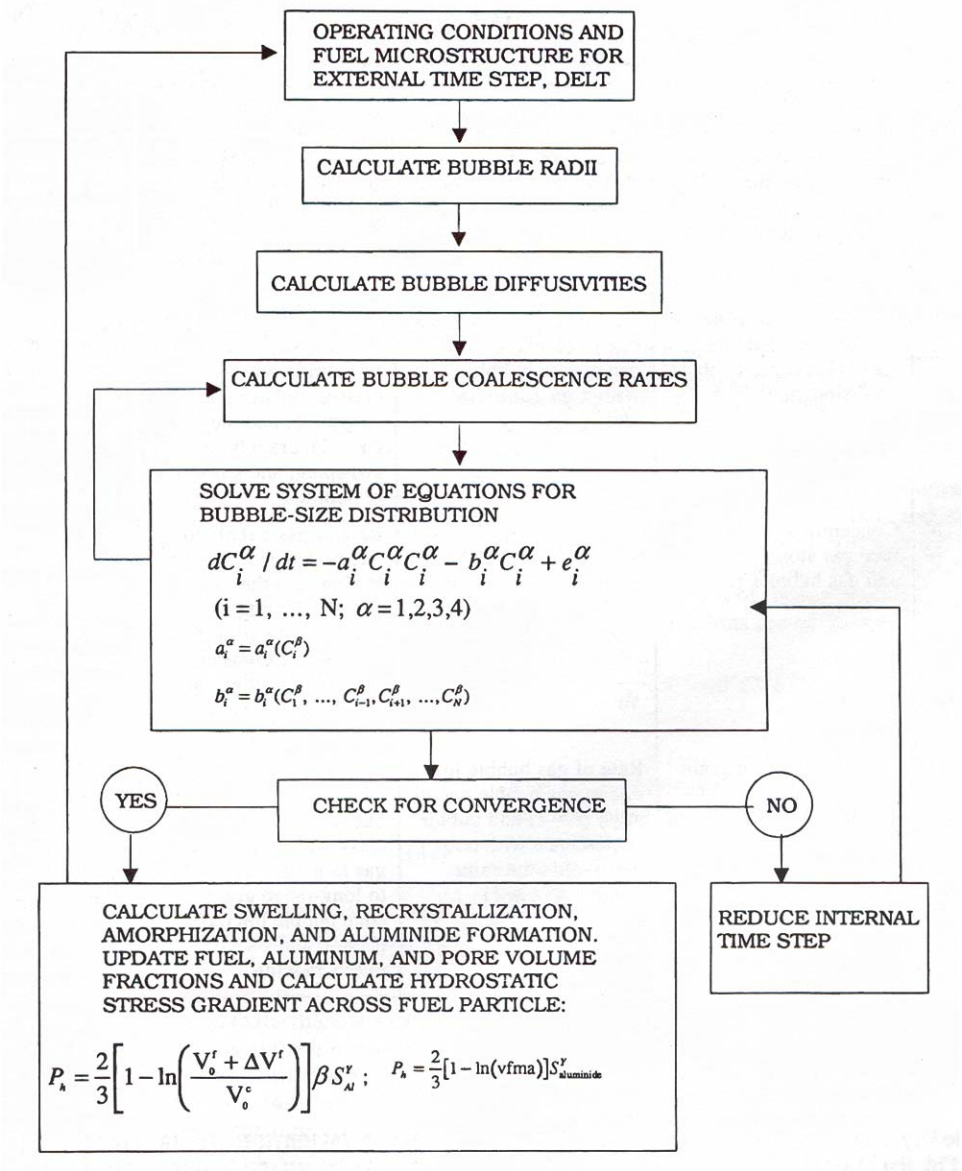

Figure 3.3: *DART* flowchart for node (l, j, k)

α	i	C_i^α	$a_i^\alpha C_i^\alpha C_i^\alpha$	$b_i^\alpha C_i^\alpha$	e_i^α
$1,2$	1	Concentration of intragranular gas atoms ($\alpha = 1$) and gas atoms on dislocations ($\alpha = 2$)	Rate of gas atom loss due to gas bubble nucleation	Rate of gas atom loss due to diffusive flow to grain boundaries, grain boundary sweeping, and diffusion into gas bubbles	Rate of gas atom gain due to atom re-solution and fission of uranium nuclei
$1,2$	$2,\ldots,N$	Concentration of intragranular gas bubbles ($\alpha = 1$) and gas bubbles on dislocations ($\alpha = 2$)	Rate of gas bubble loss due to bubble coalescence with bubbles within the same size class	Rate of gas bubble loss due to coalescence with bubbles in other size classes, diffusive flow to grain boundaries ($\alpha = 1$), grain-boundary sweeping, and gas atom re-solution	Rate of gas bubble gain due to bubble nucleation and coalescence, and diffusion of gas atoms into bubbles
3	$1,\ldots,N$	Concentration of grain-face gas atoms ($i = 1$) and gas bubbles ($i > 2$)	Rate of gas bubble loss due to gas bubble nucleation ($i = 1$) and bubble coalescence with bubbles within the same size class ($i > 1$)	Rate of gas bubble loss due to coalescence with bubbles in other size classes, venting to grain edges due to grain-face bubble interconnection, and venting of gas to grain corners due to microcracking	Rate of gas bubble gain due to bubble nucleation and coalescence, diffusion of gas atoms into bubbles, and intragranular migration to grain faces
4	$1,\ldots,N$	Concentration of grain-edge gas atoms ($i = 1$) and gas bubbles ($i > 2$)	Rate of gas bubble loss due to gas bubble nucleation ($i = 1$) and bubble coalescence with bubbles within the same size class ($i > 1$)	Rate of gas bubble loss due to coalescence with bubbles in other size classes and venting of gas to grain corners due to long-range grain-edge bubble interconnection and microcracking	Rate of gas bubble gain due to bubble nucleation and coalescence, diffusion of gas atoms into bubbles, and the venting of gas from the grain faces

Table 3.1: Definition of Variables in Eq. (3.2.1)

3.3 *DART* Validation

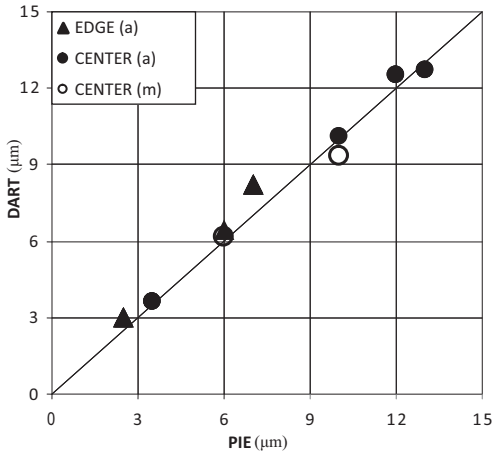

Figure 3.4: DART calculated reaction product thickness compared with data from RERTR-3 (a = atomized, m=ground).

As of the date of this publication, a complex of new models have been recently incorporated into the latest version of the *DART* code (e.g., fission gas bubble behavior in an amorphous reaction product). As a result, the thermal-mechanical code *DART* was revalidated against RERTR-3 and RERTR-5 irradiation data on interaction thickness, fuel, matrix, and reaction-product volume fractions, and plate thickness changes. In addition the effect of external pressure on the calculated plate thickness changes has been evaluated. Figure 3.4 shows*DART* calculated reaction product thickness compared with data from RERTR-3 (a=atomized fuel, m= ground fuel). The results that are shown in Fig. 3.4 support the validity of the *DART* temperature calculation. Figure 3.5 shows the *DART* calculated fuel, matrix, and reaction product volume fractions compared with data from RERTR-3.

The trend shown in Fig. 3.5 is for the *DART* calculation to overpredict the matrix and underpredict the reaction-product volume fraction, while at the same time following the trends of the fuel volume-fraction data. The calculations shown in Figs. 3.4-3.5 were performed assuming that the interaction product composition is UAl_7 with a density of 4.5 gm·cm^{-3}. Thus, given the good agreement between model predictions and measured quantities demonstrated for the interaction-product thickness shown in Fig. 3.4, the discrepancy illustrated in Fig. 3.5 suggests that the chemistry incorporated in the model is not physically realistic. Currently the composition of the U-Mo-Al interaction product is not known. However it is reasonable to expect that not only is there a gradient in composition across the fuel plate during irradiation, but that the composition changes with irradiation time. In principle, *DART* can

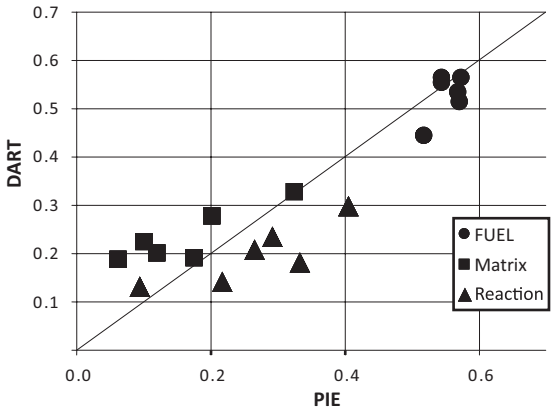

Figure 3.5: DART-calculated fuel, matrix, and reaction product volume fractions compared with data from RERTR-3.

be utilized to explore differing assumptions on the nature of the interaction-product chemistry and to rank the assumptions in order of physically viability. Eventually this ranking can be tested experimentally.

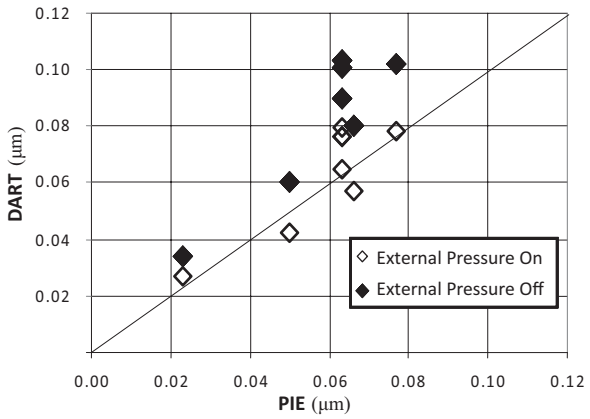

Figure 3.6: DART-calculated plate thickness changes with and without the effects of external pressure compared with measured data from RERTR-3.

Figure 3.6 shows the calculated plate thickness changes with and without the effects of external pressure compared with measured data from RERTR-3. The results shown in Fig. 3.6 demonstrate that including the effects of stress are important in fully describing the irradiation behavior of U-Mo dispersion fuel.

Chapter 4

Swelling predictions for U-Pu-Zr fuels

The Rest Models for U-Pu-Zr fuels primarily focus on the swelling behavior of the separate fuel zones. Uranium alloy fuels demonstrate three distinct annular regions under irradiation. The outermost region is termed the α-uranium zone and is characterized by a dimensional instability in the form of anisotropic growth and swelling[39]. The stresses created by the proliferation of mismatched strains lead to enhanced porosity resulting in cavitational void swelling in this region. In between the α-uranium zone and the innermost γ-uranium zone there is an 'intermediate' zone in which a high density of fine grain structures have been observed. Although, observations in this zone are limited, it has been postulated that a process analogous to recrystallization (see §2.2.3) occurs, promoting swelling from increased bubble nucleation and growth. The γ-uranium zone behaves in a way similar to fuels in the amorphous phase. The plastic flow environment in this zone allows for enhanced diffusivities that improve fission gas mobility.

4.1 U-Pu-Zr swelling in the α-, *intermediate*- and γ-uranium zone

4.1.1 α-uranium zone: Cavitational swelling

The construction of a mechanistic model for a gas-bubble-nucleated cavitational-void swelling of the α-uranium zone is presented in this section. The physics

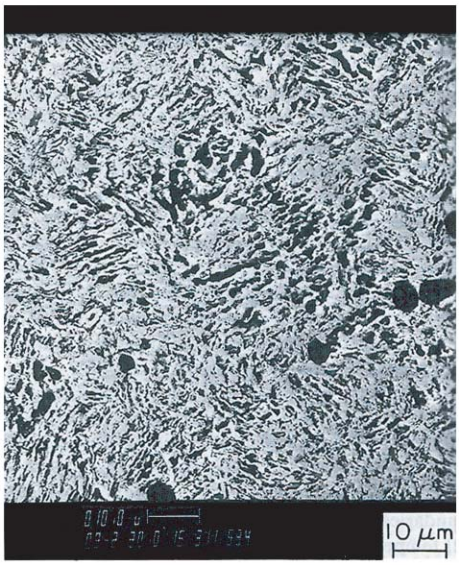

Figure 4.1: Example of porosity development at boundaries between lamellae of high-Zr phase and low-Zr phase.

of the model is based on bias-driven growth (by adsorption of excess vacancies produced by irradiation damage) of phase-boundary cavities that initially evolve as fission-gas bubbles. The description of fission-gas release from α-uranium is supported by photomicrographs (see Fig 4.1) obtained by scanning electron microscopy of post-irradiation U-xPu-Zr fuel specimens that portray this zone as a laminar structure with a high degree of interconnected porosity. Based on examination of the α-uranium microstructure, the thin fuel lamina is approximated by a spherical grain with a 1 μm radius. Gas generated within the fuel lamina diffuses to the phase boundaries and is released if a network of long-range interconnected porosity has been established. Growth of cavities within the α-uranium lamina is not predicted to occur because the effect of irradiation-induced gas atom re-solution is strong and prevents these gas bubbles from growing to the critical size required for bias-driven growth. In addition, the reduced effect of re-solution of phase-boundary bubbles (i.e., the boundaries act as an efficient sink for gas atoms) allows gas bubbles that nucleate on the phase boundaries to grow to critical size, depending on the temperature.

In the following discussion it is assumed that the gas-bubble/-cavity distribution within the lamina and on the phase boundaries can each be represented by an appropriate density of average-size cavities. Here, a cavity can either be a gas bubble or a void. The problem is to calculate the evolution of the intra-

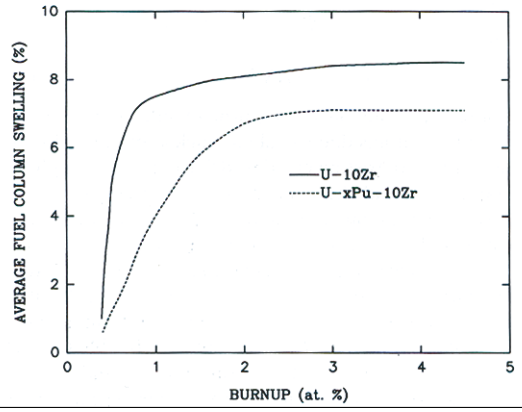

Figure 4.2: Axial fuel swelling of U-10Zr and U-xPu-10Zr alloy fuel.

and interphase cavities and to provide a criterion for evaluating bias-driven growth of cavities as compared to gas-driven growth. Fission gas generated within the matrix of the U-Pu-Zr alloy fuel evolves according to the equation

$$\frac{\mathrm{d}C_g^b}{\mathrm{d}t} = -16\pi F_n^b R_c^b D_g^b C_g^b C_g^b - 4\pi R_c^b D_g^b C_g^b C_c^b - \dot{g}_0(t) + \beta\dot{f} + BN_c^b C_c^b \quad , \quad (4.1.1)$$

where the terms on the right hand side represent the loss of gas atoms due to bubble nucleation, diffusion of fission gas to existing cavities, diffusion of gas to phase boundaries and the gain of gas due to generation by fissioning uranium atoms and gas-atom re-solution from gas bubbles, respectively (the superscript b denotes quantities located in the fuel bulk, i.e., within the fuel lamina). F_n^b is the nucleation factor (i.e., probability that when two atoms come together they form a stable gas-bubble nucleus). R_c^b is the bulk gas-bubble (cavity) radius, D_g^b is the gas atom diffusivity, C_g^b and C_c^b are the gas-atom and gas-bubble (cavity) concentrations, B is the irradiation-induced gas-atom re-solution rate from bubbles, N_c^b the number of gas atoms in a cavity, $\beta\dot{f}$ is the gas-atom generation rate, and the loss rate of gas-atoms to the phase boundaries, $\dot{g}_0(t)$, is given by

$$\dot{g}_0(t) = -\frac{6}{d}\frac{D_g^b \partial C_g^b}{\partial r}\bigg|_{r=d/2} \quad , \quad (4.1.2)$$

where r is the radial coordinate, and d is the diameter of the equivalent spherical grain. Eq (4.1.2) is solved by splitting the grain into two concentric regions

of approximately equal volume. In each region, the gas concentration is represented by a quadratic function of radial coordinate. The gas-filled cavities within the bulk material evolve according to the equation

$$\frac{\mathrm{d}C_c^b}{\mathrm{d}t} = 16\pi \frac{F_n^b R_c^b D_g^b C_g^b C_g^b}{N_c^b} \quad . \tag{4.1.3}$$

The term on the RHS of Eq. (4.1.3) represents the increase in bulk cavities due to cavity nucleation.

Conservation of gas atoms requires that

$$N_c^b C_c^b + C_g^b + \int_0^t \dot{g}_0(t)\mathrm{d}t = \int_0^t \beta \dot{f} \mathrm{d}t \quad . \tag{4.1.4}$$

Differentiating Eq. (4.1.4) and substituting Eq. (4.1.1) and Eq. (4.1.3) results in an expression for the time rate of change of the number of gas atoms in an average-size bulk cavity,

$$\frac{\mathrm{d}N_c^b}{\mathrm{d}t} = -16\pi F_n^f R_c^f D_g^f C_g^f C_g^f - 4\pi R_c^f D_g^f C_g^f C_c^f + \dot{g}_0(t) - \dot{h}_0 C_g^f \quad , \tag{4.1.5}$$

and

$$\frac{\mathrm{d}C_c^f}{\mathrm{d}t} = 16\pi \frac{F_n^f R_c^f D_g^f C_g^f C_g^f}{N_c^f} \quad , \tag{4.1.6}$$

where the superscript f denotes quantities associated with the phase boundaries (e.g., faces), and $\dot{h}_0$ is the fission-gas-release rate. Conservation of gas atoms on the phase boundaries requires that

$$N_c^f C_c^f + C_g^f = \int_0^t \dot{g}_0(t)\mathrm{d}t - \int_0^t \dot{h}_0(t)\mathrm{d}t \quad . \tag{4.1.7}$$

Gas release from the phase boundaries, which occurs when long-range interconnection of the interphase porosity develops is represented by the last term on the RHS of Eq. (4.1.7). The fission-gas-release rate $\dot{h}_0$ is given by

$$\dot{h}_0 = \chi V \left[C_g^f + C_c^f N_c^f \right] \quad , \tag{4.1.8}$$

where V is the volume of the fuel under consideration, and χ is the fraction of the boundary cavity interlinkage, which is determined as follows.

Phase-boundary cavity interlinkage is determined by directly addressing the distribution of the calculated cavity size. The projected areal coverage of the phase-boundary face by these cavities, per unit volume, is given by

$$A_f = \pi R_c^2 C_c^f f_f(\theta) \quad , \tag{4.1.9}$$

where $f_f(\theta)$ is a geometrical factor that accounts for any deviation from a spherical shape of the cavities (e.g. lenticular). If the cavities are assumed to be closely packed, the maximum areal coverage per unit area of phase boundary is $A_f^* = 0.907$. Cavity interlinkage occurs when

$$A_f \geq A_f^* S_v^{\alpha\alpha} \quad , \tag{4.1.10}$$

where $S_v^{\alpha\alpha}$ is the grain-face area per unit volume.

Equations (4.1.9) and (4.1.10) do not account for local variations in fuel microstructure. To include these effects in the calculation of cavity interlinkage, it is assumed that the local variations in fuel microstructure can be represented by the width σ_f of a distribution A_f, Eq. (4.1.9), such that the fraction of cavity interlinkage is given by

$$\chi = \frac{1}{\sigma_f \sqrt{2\pi}} \int\limits_{x=A_f^* S_v^{\alpha\alpha}} exp \left[\frac{(-x-A)^2}{2\sigma_f^2} \right] \mathrm{d}x \quad . \tag{4.1.11}$$

The width of the distribution in Eq. (4.1.11) is a function of erratic structural parameters that depend on local fuel condition and heterogeneity. In principle, this width can be determined experimentally.

In analogy to the derivation of Eq. (4.1.5) with the aid of Eqs. (4.1.6)-(4.1.7), we can obtain an equation for the time rate of change of the number of gas atoms within an average-size phase-boundary cavity, i.e.,

$$\frac{\mathrm{d}N_c^f}{\mathrm{d}t} = 4\pi R_c^f D_g^f C_g^f - \dot{h}_0 N_c^f \quad . \tag{4.1.12}$$

In a material containing several types of point-defect sinks, such as dislocations and cavities, the sinks generally have different capture efficiencies for vacancies and interstitials[40]. During irradiation, partitioning of point defects to sinks is unequal. This bias results in a larger flux of vacancies to voids and of interstitials to dislocations. Because the thermal emission rate of vacancies from cavities depends on the exponential of the inverse of the cavity radius, at a given temperature and for a fixed number of gas atoms in the cavity, there is a critical cavity radius above which the bias-induced net vacancy influx is larger than the net thermal vacancy outflux, and the cavity will grow as a void. Below the critical radius, the cavity will either shrink or, if it contains gas, become stabilized. Similarly, because the thermal emission rate of vacancies also depends on the exponential of the inverse of the temperature, at a given cavity radius and for a fixed number of gas atoms in the cavity, there is a critical temperature below which the bias-induced net vacancy influx is greater than the new thermally emitted vacancy outflux. As the temperature is raised, the critical radius increases.

Based on the above discussion, the growth rate of a cavity, as determined by the net vacancy flux, can be expressed as

$$\frac{\mathrm{d}R_c}{\mathrm{d}t} = \frac{1}{4\pi R_c^2 C_c}\left[k_{vc}^2 D_v c_v - k_{ic}^2 D_i c_i - k_{vc}^2 D_v c_v^c(R_c)\right] \quad , \tag{4.1.13}$$

where R_c is the cavity radius, C_c the cavity concentration, D_v and D_i are the vacancy and interstitial diffusivities, respectively, c_v and c_i are the respective concentrations of vacancies and interstitials, k_{vc}^2 and k_{ic}^2 denote the capture efficiency of a cavity for a vacancy or interstitial, respectively, and $c_v^c(R_c)$, the thermal equilibrium vacancy concentration near a cavity of radius R_c, is given by

$$c_v^c(R_c) = c_v^0 \exp\left[-\left(P_g - 2\gamma/R_c - \sigma\right)\Omega/kT\right] \quad , \tag{4.1.14}$$

where P_g is the pressure of the gas in the cavity, Ω is the atomic volume, γ is the surface energy, σ is the hydrostatic stress due to external forces (e.g.,

the cladding), and c_v^0 is the defect-free thermal equilibrium fractional vacancy concentration given by

$$c_v^0 = \exp\left[-\epsilon_v^F/kT\right] \quad , \tag{4.1.15}$$

where ϵ_v^F is the vacancy formation energy.

The pressure of the gas in the cavity, P_g, can be determined from the number of gas atoms in the cavity, N_c^f or N_c^b and an appropriate equation of state; a modified hard-sphere equation of state is utilized in the present formulation[18]. Once the fuel contacts the cladding, the high value of σ generated will inhibit further fuel swelling (see Eqs. (4.1.13) and (4.1.14)).

The concentration of mobile defects within the α-uranium (e.g., the vacancy concentration) can be determined from the solution of the rate equations describing point defect behavior. The equations are

$$\frac{\mathrm{d}c_v}{\mathrm{d}t} = \phi\dot{f} - k_v^2 D_v c_v - \alpha c_i c_v \quad , \tag{4.1.16}$$

$$\frac{\mathrm{d}c_i}{\mathrm{d}t} = \phi\dot{f} - k_f^2 D_i c_i - \alpha c_i c_v \quad . \tag{4.1.17}$$

Here, α is the rate constant for the bulk recombination of interstitials and vacancies, $\phi\dot{f}$ is the defect production rate (in displacements per atom (dpa) per second), and k_v^2 and k_i^2 are the total sink strengths for vacancies and interstitials, respectively.

On the basis of previous analytical studies[41] that used the defect behavior code Cluster 78[42], only single-vacancy and single-interstitial kinetics are considered. Cavity nucleation results from the agglomeration of two (or more) vacancy clusters and is described by the first terms on the RHS of Eqs. (4.1.3) and (4.1.6). If the only sinks for the point defects are cavities and dislocations, k_v^2 and k_i^2 are written

$$k_v^2 = k_{vc}^2 + k_{v\rho}^2 \quad , \tag{4.1.18}$$

$$k_i^2 = k_{ic}^2 + k_{i\rho}^2 \quad , \tag{4.1.19}$$

and the quantities $(k_v)^{-1}$ and $(k_i)^{-1}$ are the mean distances a free interstitial or vacancy moves in the material before it becomes trapped. The central problem in the rate theory of microstructural evolution is the determination of the various sink strengths for migrating point defects. The appropriate sink strengths of cavities for vacancies, k^2_{vc}, and interstitials, k^2_{ic}, in the continuum approximation implicit in a rate-theory approach take the form

$$k^2_{vc} = 4\pi R_c C_c \left[1 + k_v R_c\right] \quad , \tag{4.1.20}$$

and

$$k^2_{ic} = 4\pi R_c C_c \left[1 + k_i R_c\right] \quad . \tag{4.1.21}$$

The sink strengths of dislocations for vacancies and interstitials take the form

$$k^2_{v\rho} = Z_{v\rho}\rho \quad , \tag{4.1.22}$$

$$k^2_{i\rho} = Z_{i\rho}\rho \quad , \tag{4.1.23}$$

where $Z_{v\rho}$ and $Z_{i\rho}$ are the dislocation bias terms for vacancies and interstitials, respectively, and ρ is the total dislocation density in the material. The full set of Eqs. (4.1.1)-(4.1.23) that make up the fission-gas-bubble-nucleated cavitational swelling model is called Cavity.

Comparison with data from U-10Zr and U-19Pu-10Zr fuel elements

Incubational swelling is generally not observed in the case of pure metals. The incubation observed in the bias-driven swelling of stainless steels is quite short (10-20 dpa) compared with that observed in Integral Fast Reactor (IFR) fuels (hundreds of dpa) and is still not properly understood. Inasmuch as the critical cavity size required for void growth is relatively small (on the order of nanometers), this size is achieved for interphase bubbles at $\sim 0 - 20$ dpa, depending on the values of various gas-atom ad microstructural properties, far short of the incubation time observed in the IFR fuels (e.g. see Fig. 4.2). However, the results of Cavity (i.e., Eqs. (4.1.1)-(4.1.23)) assessment has shown that

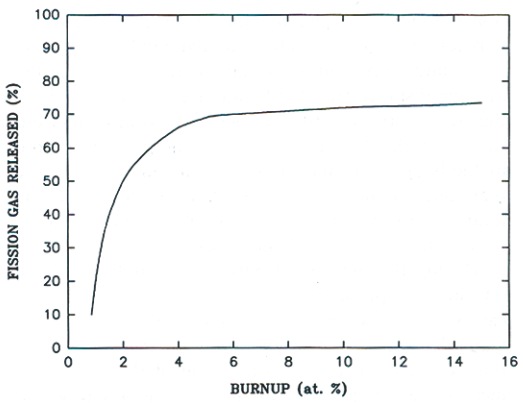

Figure 4.3: Fractional fission gas release behavior in fuel alloys of the type U-xPu-10Zr alloy fuel.

long incubation times can be fully understood in terms of a reduced gas-bubble nucleation rate on the α/δ-phase boundaries. In general, gas-bubble nucleation in bulk material is thought to be inefficient due to a successful nucleation even requiring the presence of one or more vacancies or vacancy clusters in close proximity to the colliding gas atoms[43]. In contrast, gas bubble nucleation on normal high-angle grain boundaries is usually treated as 100% efficient due to the characteristic high-sink strength nature of the boundaries. What is being proposed here is that the α/δ-phase boundary lamellae are less efficient gas-bubble incubators than normal high-angle grain boundaries.

Table 4.1 lists the nominal values of various material constants used in the Cav-

Symbol	Property	Value	Reference
D_v^0	Preexp. factor in vac. diff.	$2.0 \times 10^{-8}\,\mathrm{m^2 s^{-1}}$	[43]
ϵ_v^m	Vacancy migration energy	1.28 eV	[44]
ϵ_v^F	Vacancy formation energy	1.6 eV	[40]
Z_v	Dislocation bias for vacancies	1.0	[40]
Z_i	Dislocation bias for interstitials	1.025	[40]
γ	Surface energy	$0.5\,J/\mathrm{m^2}$	[45]
r_{iv}	Radius of recombination volume	$2.0 \times 10^{-10}\,\mathrm{m}$	[46]
ρ	Dislocation density	$7.0 \times 10^{13}\,\mathrm{m^{-2}}$	[45]
F_n^b	Bble. nucl. factor within lamina	10^{-5}	[43]
F_n^f	Bble. nucl. factor on phase bound.	10^{-5}	[45]
Ω	Atomic volume	$4.09 \times 10^{-29}\,\mathrm{m^{-3}}$	[43]

Table 4.1: Values of various material constants used in cavity calculations

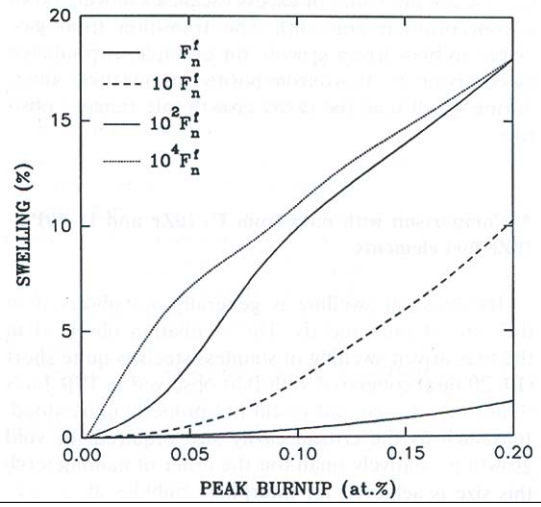

Figure 4.4: Cavity-calculated unrestrained fuel volume swelling for U-10Zr fuel elements as a function of fuel burnup for various values of the phase-boundary gas-bubble nucleation factor, F_n^f.

ity calculations. Figure 4.4 shows cavity-calculated low-burnup unrestrained fuel volume swelling for U-10Zr fuel elements as a function of fuel burnup for various values of the phase-boundary gas-bubble nucleation factor, F_n^f. The Cavity calculations were made by subdividing the element into nine axial and six radial nodes (i.e., 54 annular regions) to model the axial and radial temperature gradients as well as the axial flux gradient. The temperature and power history that were input to the Cavity simulations were obtained from LIFE-METAL calculations[47]. As shown in Fig. 4.4, as the value of F_n^f is varied from 10^{-1} to 10^{-5}, the slope of the swelling versus burnup decreases due to the reduced cavity nucleation rate. A value of $F_n^f = 10^{-5}$ results in calculated rates which are in qualitative agreement with average fuel column swelling data (see Fig. 4.3).

Figure 4.5 shows Cavity-calculated unrestrained fuel volume swelling for U-10Zr fuel elements and gas release as a function of burnup using $F_n^f = 10^{-5}$. The swelling shown in Fig. 4.5 increases rapidly in rate after an incubation period of $\sim$0.2 at.% burnup and reaches $\sim$50% volumetric swelling at 1.2 at.% burnup. Gas release begins at about 0.6% burnup and rises rapidly to $\sim$70% release at $\sim$1.2 at.% burnup. The calculated gas release shown in Fig. 4.5 is consistent wih the measured fission gas release behavior in fuel alloys of the type U-xPu-10Zr (see Fig. 4.3).

Figure 4.6 shows Cavity-calculated unrestrained swelling as a function of fuel length for two values of the average burnup for U-10Zr fuel elements irradi-

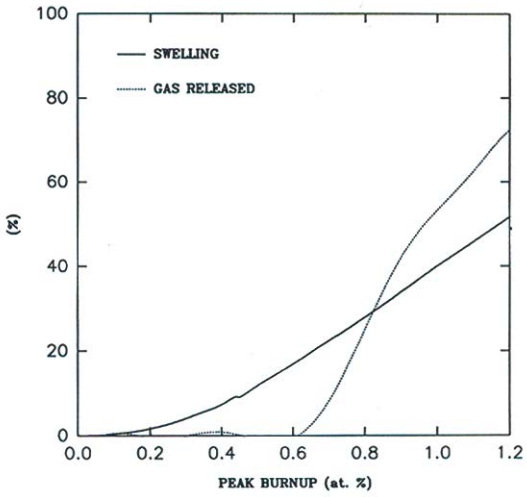

Figure 4.5: Cavity-calculated unrestrained fuel volume swelling and gas release for U-10Zr fuel elements as a function of burnup using $F_n^f = 10^{-5}$.

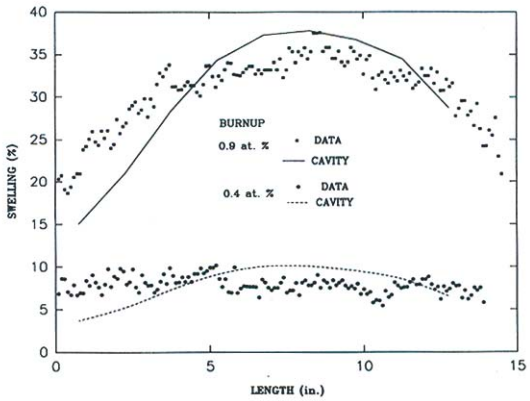

Figure 4.6: Cavity-calculated unrestrained swelling as a function of fuel length for two values of average burnup for U-10Zr fuel elements irradiated in Experimental Breeder Reactor II in assembly X423[48], compared with the data.

ated in the Experimental Breeder Reactor II in assembly X423[48], compared with data.

The data (mean length and diameter changes) were normalized to the peak swelling at each burnup using an average value of the measured axial to radial deformation. The Cavity calculations shown in Fig. 4.6 were performed with the values for various material constants listed in Table 4.1. As is shown in

Fig. 4.6, the results of the cavity calculations follow the trends of the measured deformation.

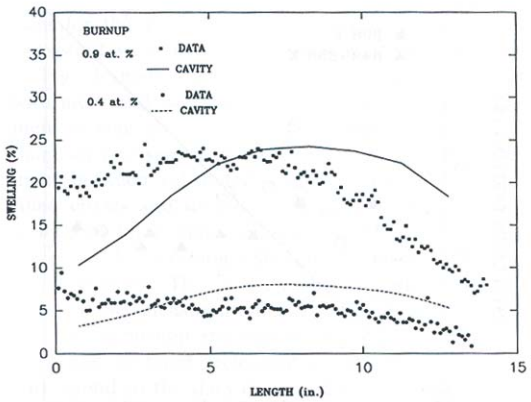

Figure 4.7: Cavity-calculated unrestrained swelling as a function of fuel length for three values of average burnup for U-19Pu-10Zr fuel elements irradiated in Experimental Breeder Reactor II in assembly X423[48], compared with the data. A value of the dislocation density of $\rho = 2 \times 10^{13}$ m^2 was used in the calculations.

Figure 4.7 shows Cavity-calculated unrestrained swelling as a function of fuel length for two values of the average burnup of U-19Pu-10Zr fuel elements irradiated in assembly X423[48], compared with the data. The calculations shown in Fig. 4.7 utilized a value for the dislocation density, ρ, of 2×10^{13} m^{-2}. Using the same dislocation density as was used to calculate swelling in U-10Zr (i.e., $\rho = 7 \times 10^{13}$ m^{-2}) results in an overprediction of swelling in the ternary fuel. As shown in Fig. 4.7, the difference in swelling between the binary and ternary alloy fuels can be attributed to the existence of a lower dislocation density (compared to the U-10Zr) in fuel containing plutonium.

4.1.2 *Intermediate* zone: Recrystallization

Although not much is known about the nature of swelling in the *intermediate* zone, the grain microstructure in this region has a strong resemblance to the recrystallized microstructure observed in irradiated intermetallic fuels used in research reactors. Models which have been developed to predict swelling in these intermetallic fuels can be used as a basis for calculating swelling in the *intermediate* zone. The model for swelling of the *intermediate* zone is based on the creation of additional grain surface, and as the principle of recrystallization proposes, a finer grained structure than what existed in the as-fabricated material evolves upon formation of the *intermediate* zone. Gas bubbles nucleate and grow at an accelerated rate on this relatively dense network of subgrain

boundaries as compared to the bulk material. The full recrystallization theory can be found in §2.2.3 and is outlined in Eqs. (2.2.20), (2.2.43), (2.2.46), and (2.2.47).

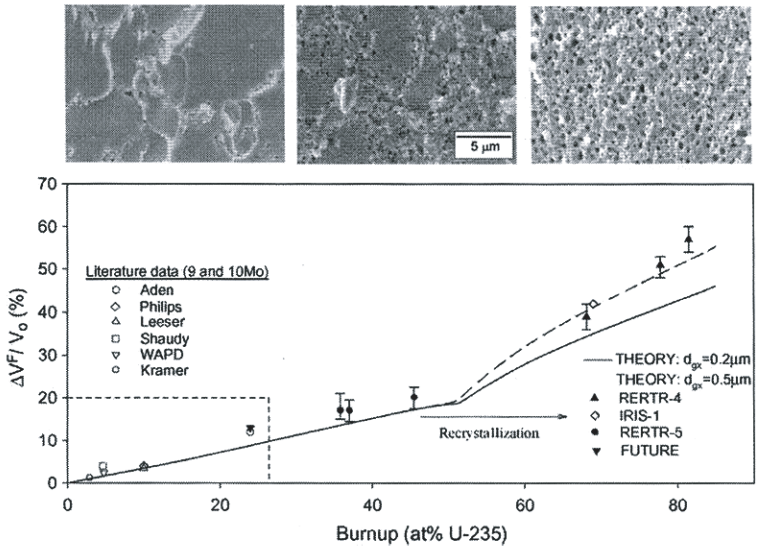

Figure 4.8: DART calculated reaction product thickness compared with data from RERTR-3 (a = atomized, m=ground).

Figure 4.8 shows data for U-xMo total fuel swelling behavior vs. burnup compared to the theory of recrystallization for two values of the nominal recrystallized grain size. Although further observations are necessary, the process of recrystallization seen in U-xMo is believed to be comparable to the phenomenon observed in the *intermediate* zone. From Fig. 4.8 it is clear that the theory follows the trends of the swelling data as a function of burnup across the transition from no recrystallization to full recrystallization. The three micrographs located above Fig. 4.8 show, respectively, the fuel prior to recrystallization, at the initiation of recrystallization and when approximately 100% of the fuel has been recrystallized. As seen in the second micrograph of Fig. 4.8, the initiation of recrystallization occurs primarily along the original grain boundaries. The recrystallized grain size measured from the micrographs in Fig. 4.8 is $\approx 0.2 - 0.5\,\mu$m.

4.1.3 γ-uranium zone: Plastic flow

The cubic γ-uranium phase occurs at the center of fuel pins that operate at centerline temperatures over $662°$C. Although a consistent understanding of the

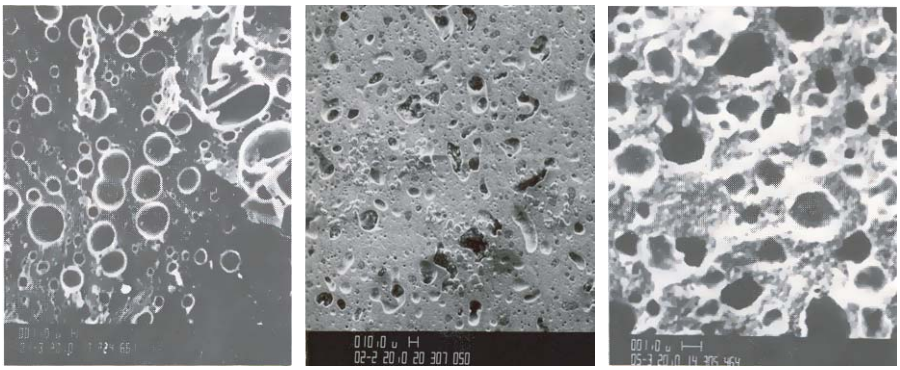

(a) (b) (c)

Figure 4.9: SEM micrographs of (a) amorphous U_3Si, (b) the γ-uranium zone of U-19Pu-Zr, and (c) amorphous U_6Fe. The side by side comparison suggests why diffusion in the γ-uranium zone may be approximated using a plastic flow model.

γ-uranium zone has not been reached, through microstructural examinations of the γ-uranium phase structure it has been asserted that there is no evidence of tearing, but a presence of large interconnected gas bubbles. These large, sinuous bubbles indicate high fission-gas mobility, isotropic growth, and motion in a viscous-like, highly plastic medium with characteristics analogous to those observed in fuels gone amorphous. The evolution of the porosity in the γ-uranium zone is due to enhanced gas-atom diffusivities in the irradiated material. Bubble growth in the low viscosity material is approximated by an this enhanced diffusivity due to plastic flow.

Because of the high plasticity of the γ-uranium zone, the enhanced diffusivity can be approximated by calculating the diffusivity of low-viscosity amorphous materials which also exhibit substantial plastic flow. This assumption does not imply that the γ-uranium zone has gone amorphous. Rather, the γ-uranium zone has a highly plastic crystalline structure making enhanced diffusivity possible. It should also be noted that the approximation derived below correlates the irradiated, high-temperature γ-uranium zone to irradiated, low-temperature, highly plastic, amorphous fuels such as, U_3Si and U_6Fe.

Model for gas-diffusion of highly plastic amorphous and crystalline materials

The major differences between the crystalline and amorphous phases are due to changes in elastic properties. P. R. Okamoto et al.[49] shows that substantial elastic softening of intermetallic compounds occurs in the crystalline phase and is associated with the progressive destruction of the chemical long-range

order. Brillouin scattering experiments and transmission electron diffraction studies[50] have shown that single crystal silicon and polycrystalline intermetallic compounds undergo dramatic elastic softening after irradiation with charged particle beams. Measurements of the change in sound velocity shows that the average shear constant decreases by as much as 30% in silicon and by as much as 50% in intermetallics. These results point ot a strong coupling between strain and order parameter as a possible origin of the elastic softening and to strain accumulation as an important prerequisite for the amorphization of these intermetallics.

The degree of long-range atomic order, S, has an exponential dependence on the total dose, ϕt

$$S/S_0 = \exp\left(-K\phi t\right) \quad , \tag{4.1.24}$$

where K is a constant. Measurements by Okamoto et al.[51] of the Zr_3Al lattice dilation, $\Delta a/a$, determined from the change spacings of the (400) fundamental reflections, showed that $\Delta a/a$ increases with increasing dose, reaches a maximum value of about 0.8% at the dose where amorphization starts, then drops abruptly to $\sim 0.7\%$ ($S \sim 0$) and thereafter remains approximately constant. For doses up to 0.2 dpa, the percentage lattice dilatation is a quadratic function of S

$$\Delta a/a = \left(\Delta a/a\right)_m \left[1 - \left(S/S_0\right)^2\right] \quad , \tag{4.1.25}$$

where $S/S_0 = \exp\left(-11.6\phi t\right)$ is the observed dose dependence of S and $\left(\Delta a/a\right)_m = 0.775\%$ is the maximum lattice dilatation due to disordering. The results of Brillouin scattering measurements (post-irradiation) on the same material showed that a lage ($\sim 50\%$) decrease in the shear constant occurs after chemical disordering. The decrease occurs prior to the onset of amorphization, and hence the elastic softening is a precursor effect rather than a consequence of amorphization. This result is significant since it strongly suggests that an elastic instability triggers the onset of amorphization. For doses up to 0.15 dpa, the shear constant is a quadratic function of S

$$C/C_0 = 0.5\left[1 + \left(S/S_0\right)^2\right] \quad . \tag{4.1.26}$$

The S^2 dependence of both the elastic softening and lattice dilatation can be understood qualitatively in terms of phenomenological theories of order-disorder

based on central pair-wise interactions, as described in refs. *12* and *13* of the paper by Okamoto et al.[49].

The S^2 dependence described by Eqs. (4.1.25) and (4.1.26) implies that the shear constant is a linear function of volume dilatation, $3\Delta a/a$. Eliminating $(S/S_0)^2$ in Eqs. (4.1.25) and (4.1.26) yields

$$C/C_0 = \left[1 - \frac{(3\Delta a/a)}{4.65}\right] \quad . \tag{4.1.27}$$

As described by Eq. (4.1.27), the shear constant decreases linearly with volume dilatation and extrapolates through the glass gap (i.e., the change in density between the partially disordered crystalline phase and the amorphous phase, which is $\sim 2.5\%$ to zero at $3\Delta a/a \sim 4.7\%$, which is very close to the value of $4 \pm 1\%$ measured by Schulson for total volume expansion of amorphous Zr_3Al[52]). The loss of resistance to shearing at a dilatation of 4.7% indicates that the partially disordered material ($S \sim 0.2$) is mechanically unstable with respect to density fluctuations of comparable magnitude to the glass expansion gap. Since density fluctuations of comparable magnitudes may occur in the cores of energetic cascades, the irradiation itself can provide the additional density fluctuation required to trigger an elastic instability in the partially disordered material.

Okamoto et al.[49] emphasize that the elastic instability that occurs during irradiation is not one in which the entire crystal transforms catastrophically to an amorphous phase at some critical disorder. The glass expansion gap represents a nucleation barrier against glass formation in the highly strained, metastable, disordered crystalline material. Although the dilatational strain will have a well-defined average-value, local dilatation fluctuations result in regions of mechanical instability, i.e., amorphization, and not everywhere simultaneously. In the context of this model, the important point is that disorder results in a volume-dependent shear coefficient during irradiation similar to that associated with the heating and melting of metals.

Calculation of gas-atom diffusivities within defect cascades

Measurements of ion beam mixing of tracer impurities in metallic glasses and in the pure crystalline elements comprising the glasses performed by Hahn et al.[53] at 80 K demonstrated that the ion mixing efficiency of the tracer impurities was greater in the metallic glasses than in either of the constituent elements for the NiZr and CuEr systems. The athermal diffusivities of the tracer impurities in the metallic glasses was within a factor of ten of those measured in the crystalline materials. Although in the right direction, a factor of ten increase

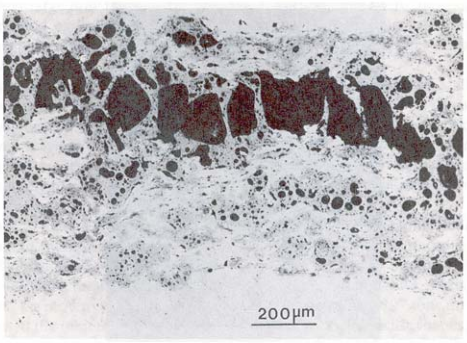

Figure 4.10: Formation of large gas bubbles in irradiated U_3Si dispersed in aluminum.

in the gas-atom diffusivities is not sufficient to explain the breakaway swelling observed in the irradiated U_3Si material (Fig. 4.10). However, the Hahn et al. results are consistent with the picture of cascade dynamics provided by recent molecular dynamics computer simulations[54]. The simulations show that the cascade region has a liquid-like structure during the thermal spike phase of the cascade evolution.

C. P. Flynn[55] has developed a simple picture for the relationship between the migration energy for diffusion and the elastic constants of the material. A diffusion jump introduces a lattice strain. One may expect the strain caused by the jump to be mainly a shear. An estimate of the energy in this shear strain can be obtained by treating the material as a Hookeian solid. For Hookeian shear, the work done per unit volume of strain energy in the body is given by

$$W = \frac{1}{2}\epsilon^2 C' \quad , \tag{4.1.28}$$

where C' is the shear modulus and ϵ is the strain caused by the jump. The energy in the shear strain is obtained by multiplying W by the strained volume. Choosing a volume given by $4/3\pi a^3$, where a is the atomic spacing, results in

$$E_m = \frac{4}{6}\pi a^3 \epsilon^2 C' \quad . \tag{4.1.29}$$

In Flynn's more rigorous elastic theory, large atomic displacements causing diffusion jumps in monatomic crystals are treated as a summation of phonon

amplitudes. Using the harmonic approximation, Flynn derived an expression for a Gibbs function for the migration energy given by

$$E_m = C\Omega\delta^2 \quad , \tag{4.1.30}$$

where C is an average elastic constant for migration, Ω is the atomic volume and $\delta^2 = q^2/s^2$, where q measures the energy fluctuation needed for a jump to continue completion and s is a measure of the jump path. Equations (4.1.29) and (4.1.30) have the same functional dependence on the shear modulus. A decrease in the shear modulus will result in a proportional decrease in the migration energy for diffusion.

The thermally activated gas atom diffusivities in a highly plastic material can be described by an exponential dependence on temperature, i.e.,

$$D_a = D_0 \exp\left(-E_m/RT\right) \quad . \tag{4.1.31}$$

Gas-atom mobility in irradiated crystalline material at relatively low temperatures is dominated by athermal diffusion. However, a decrease in E_m may result in thermal activation dominating the diffusion process. From Eq. (4.1.30) and (4.1.27), the migration energy in the damaged material is reduced to

$$E_d = E_m \left[1 - \frac{(3\Delta a/a)}{4.65}\right] \quad , \tag{4.1.32}$$

where E_m is on the order of the migration energy in the undamaged material. The diffusivity in the damaged material is thus increased to

$$D_d = D_a \exp\left[(-E_m/RT) \cdot \frac{(3\Delta a/a)}{4.65}\right] \quad . \tag{4.1.33}$$

For a 3% volume dilatation, the diffusivity at $150°$C would be enhanced by about 11 orders of magnitude over thermal diffusion.

While the high plasticity of the γ-uranium zone does not have a diffusion coefficient equal to the one given in Eq. 4.1.33, the enhanced diffusion observed in this phase can be related to Eq. 4.1.33 by approximating the migration energy

of amorphous fuels. That is, $E_d(\gamma\text{-uranium }) \approx E_d(\text{amorphous})$. The approximation follows the diffusivity of fuels that expand upon amorphization and that have a dilatation similar to that observed in U_3Si or U_6Fe. Other amorphous fuels may exhibit different forms of diffusion and would not serve as an approximation for the plastic flow of the γ-uranium zone.

What is important to note is that the gas-atom diffusivity as given by Eq. (4.1.33) is appropriate only for local regions of the amorphous (or crystalline) material that are sustaining the damage. The dilatation, $\Delta a/a$ in Eq. (4.1.33), applies to this damaged region (for example, the volume of the damage cascade), and is estimated to have a lifetime on the order of the defect cascade, 10^{-10} s. From the analysis presented on the irradiation-induced softening of the amorphous materials, Eq. (4.1.33) applies as well to damaged regions in partially disordered crystalline materials. The key difference in bubble behavior between irradiated crystalline and amorphous materials suggested by experimental results[56, 57, 58] is that the amorphous materials can undergo substantial plastic flow. In irradiated amorphous materials containing fission gas (U_3Si, for example), over-pressurized bubbles can provide the driving force for flow. In addition, density fluctuations produced by the damage cascade can provide a driving force for microscopic deformation. Plastic flow, in turn, results in enhanced bubble coalescence and bubble sweeping of gas-atoms out of solution.

The calculation of bubble growth in irradiated amorphous materials is complicated by the interplay between bubble growth (driven by plastic flow) and plastic flow (for example, driven by bubble overpressure). In order to provide for a computationally tractable description of this phenomenon, the assumption is made that bubble motion in a material that undergoes plastic flow can be described by an effective bubble diffusivity on the basis of random motion in a liquid where the bubbles move by volume diffusion. The diffusivity of a bubble of radius r_i migrating by volume diffusion is given by

$$D_i = \frac{3\Omega}{4\pi r_i^3} D_u \quad , \tag{4.1.34}$$

where Ω is a molecular volume and D_u is the diffusivity of the diffusing atoms. This diffusion is qualitatively described by the Stokes-Einstein equation

$$D_u = kT/\left(6\pi r_u \eta\right) \quad , \tag{4.1.35}$$

where r_u is the radius of the diffusing species and η is the viscosity. A softening of the material produces a decrease in η and a corresponding increase in D_u.

The assumption is made here that in irradiated amorphous materials, the effect of plastic flow can be described by using an effective atomic diffusivity D_u equal to D_d (Eq. (4.1.33)). Implicit in this assumption is the application of Eq. (4.1.27), determined for Zr_3Al, to U_3Si. Although, whether or not this assumption is supportable on a quantitative level is unclear, the application of the above ideas to the irradiated amorphous-like γ-uranium zone in U-xPu-Zr fuel should provide a qualitative basis for a physical interpretation.

Chapter 5

Behavior of fission products in off-normal (transient) reactor environments

The behavior of fission products under transient operating conditions differ from normal operating environments in several ways. Sudden thermal spikes have a significant effect on the ductility of the fuel leading to the propagation of microcracking. The strong thermal gradients generated under these conditions enhance the rate and effects of grain-growth/grain-boundary sweeping, which is a process that contributes to the flow of fission products from within the grains to the grain boundary. The transient regime also seems to have a pronounced effect on the diffusivities of fission gas bubbles, creating overpressurized bubbles that, unlike those observed in normal operating conditions, move with diffusivities predicted by a surface diffusion mechanism.

The confluence of the transient-specific processes mentioned above affect the release of fission gas from the fuel element. How some of these processes affect gas release will be discussed in light of the validation of the proposed gas-release models against post-irradiation annealing experiments.

5.1 Prediction of the ductility of fuel under transient heating conditions

The ability to determine whether microcracking will occur during a given thermal transient is an important element in the prediction of fuel temperatures

and fission product release [11, 4]. Microcracking can reduce the thermal conductivity , F_c, of UO_2 to $\sim 50\%$ of the F_c value in dense fuel [30, 59]. A change of this magnitude will have a strong effect on calculated temperature profiles. As an example, calculations of centerline temperature of fuel that had undergone a thermal transient induced by the direct electrical heating (DEH) technique [30, 59] vary by as much as 600 K, depending on whether or not microcracking is considered.

5.1.1 Microcracking

In principle a "classical" mechanical treatment, involving the high-temperature stress/strain relationships of UO_2, could be used to study microcracking. Besides being very complex, this approach would require knowledge of the mechanical properties of UO_2, including strain-rate effects, at high temperatures. Data in this area are sparse and are almost nonexistent for temperatures in excess of 2400 K.

As a first-cut approach to modeling ductile/brittle behavior of oxide fuels, the DiMelfi-Deitrich model [60] has been used in *FASTGRASS* code. This model estimates the growth rate of a grain-boundary bubble under the driving force of internal pressurization. The volume growth rate due to crack propagation and to diffusional processes are compared to determine the dominant mode of volume swelling. Knowledge of the mechanical properties of UO_2 is not required.

The underlying structure of the model can be summarized as follows: A fission-gas bubble on a grain boundary can be viewed as a crack nucleus. It can be shown that such a crack will propagate unstably if the internal bubble pressure exceeds that required for bubble equilibrium, i.e., if

$$p > \frac{\gamma_s}{\rho} - \sigma \quad , \tag{5.1.1}$$

where p is the internal bubble pressure, γ_s is the fuel-gas surface energy, ρ is the bubble radius of curvature and σ is the tensile stress normal to the boundary.

Further, if a bubble, initially at equilibrium, is subjected to transient heating, the internal pressure will increase above the equilibrium value. Under these conditions, crack propagation will occur unless diffusional growth of the bubble occurs rapidly enough to maintain equilibrium conditions.

During most thermal transients, the initial mode of bubble growth will be crack propagation. The "crack-like" bubble may be able to retain its equilibrium

shape by diffusional transport of material along the grain boundary. However, if the heating rate is sufficiently high, repressurization can take place. Thus, the competition between diffusional growth and crack growth determines whether bubbles tend to remain isolated or rapidly become part of an interconnected network of microcracks.

In the DiMelfi-Deitrich analysis, an attempt is made to predict the dominant mode of bubble growth by comparing rates of volume swelling due to crack propagation and diffusional growth. In practice, this is done by comparing the instantaneous value of the grain-boundary diffusion coefficient, D_i, with the minimum value needed to maintain the equilibrium bubble volume, $D_g^{\min}$. (The calculation of $D_g^{\min}$ is discussed in detail in Ref. [60].) If $D_i < D_g^{\min}$, cracking dominates; this behavior is termed "brittle". If $D_i > D_g^{\min}$, diffusional growth or "ductile" behavior dominates.

The minimum diffusion coefficient $D_g^{\min}$ is given by

$$w \cdot D_g^{\min} = \left(\frac{mk}{\gamma_s}\right)^2 \frac{k\lambda AT}{HL\Omega(\Delta p)} \quad , \tag{5.1.2}$$

where w is the grain boundary width, m is the average number of atoms per bubble arriving at the grain boundary, γ_s is the surface energy of UO_2 and here λ is the average bubble spacing in the grain boundary. The symbol A denotes the instantaneous heating rate, H is a geometric factor, L is the bubble length, Ω is the molecular volume of UO_2 and Δp is the pressure in excess of that for an equilibrium grain-boundary bubble. T and k are the absolute temperature and Boltzmann's constant, respectively. In deriving Eq. (5.1.2), the ideal gas law and zero normal stresses on the grain boundary were assumed. (A conditional equation for $D_g^{\min}$ can be derived for the case of nonzero normal stresses on the grain boundary, e.g. see Ref. [60].)

The *FASTGRASS* code provides the gas-bubble input to Eq. (5.1.2) as a function of time (i.e., $\lambda, L, m, \Delta p$). There are some reservations about the quantitative aspects of the DiMelfi-Dietrich analysis, but it is used here as an interim model since it does seem to address the real physical phenomena of importance.

To evaluate the relative effects of crack growth versus equilibrium bubble growth on such properties as fuel temperature, intergranular swelling, grain-boundary areal coverage, interconnected porosity, and gas release, the microcracking results are transmitted back to *FASTGRASS* and DEHTTD codes as a function of time. For example, the thermal conductivity, F_c, of UO_2 is given by

$$F_c = F_c^0 \left[1.0 - C_2 \sum_i C_1 \left(\frac{A_c}{A_e} \right)_i x_i \Delta t_i \right]$$
$$= F_c^0 \left(1.0 - C_2 S_v \right) \quad , \tag{5.1.3}$$

where F_c^0 is the thermal conductivity of uncracked, stoichiometric UO_2; C_1 and C_2 are constants; $(A_c/A_e)_i$ is the ratio of areal coverage of a crack to that of an equilibrium bubble [61]; x_i is the projected grain-face areal coverage per unit volume of bubbles; Δt is a time increment; and S_v is the pore-solid surface area per unit volume. The constant C_1 is nonzero whenever $D_i < D_g^{\min}$ [see Eq. (5.1.2)]. And as mentioned above, the effect of microcracking on the thermal conductivity of UO_2, as described in Eq. (5.1.3), can result in values for $F_c \sim 50\%$ of the value in dense fuel.

Prediction for TMI-2-type accident conditions

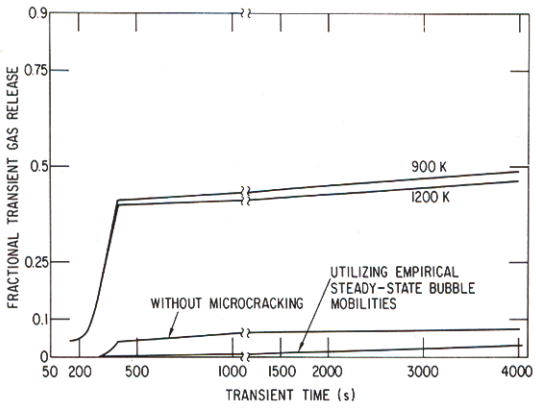

Figure 5.1: The *FASTGRASS* predictions of transient gas release versus transient time for two values of as-irradiated average fuel temperature. Results are also shown for the cases of no microcracking and no enhanced bubble mobilities (see §5.3). The heating rate, grain size and burnup are 5 K/s, 10 μm and 0.1 at.%, respectively.

The *FASTGRASS* program was run for simulated TMI-2-type power histories [62] in which steady-state period of irradiation to 0.1 at.% burnup at a constant operating temperature (and temperature gradient) is followed by a rapid shut-down, a subsequent heatup at a constant average heating rate, and a short hold period at this temperature (2600 K). Figure 5.1 shows *FASTGRASS* results for transient fission-gas release versus transient time for two values of the steady-state temperature. The fuel grain size, steady-state temperature gradient and

heating rate during the ramp were 10 μm, 1000°C/cm, and 5°C/s, respectively. The results shown in Fig. 5.1 demonstrate that most of the transient fission-gas release occurs during the heatup rather than during the relatively long hold at high temperature. The enhanced gas release during the ramp is primarily due to the enhanced bubble mobilities predicted to occur under these nonequilibrium conditions [e.g., see §5.3]. As is indicated by the additional curves in Fig. 5.1 for the cases of no microcracking and no enhanced bubble mobilities during transient (nonequilibrium) conditions (both the 900 and 1200 K steady-state scenarios give nearly identical results), the transient release during the ramp is a result of both "enhanced" bubble mobility and extensive fuel microcracking. (However, very little microcracking is predicted to occur when the empirical bubble mobilities are employed.)

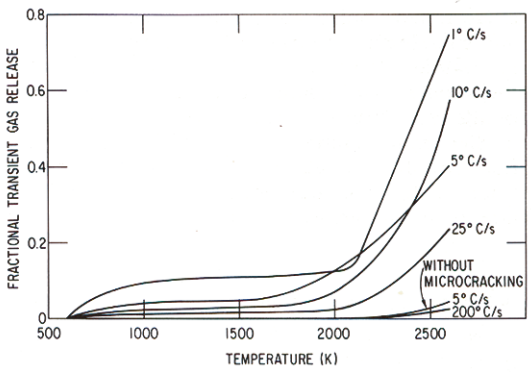

Figure 5.2: The *FASTGRASS* predictions of transient gas release versus fuel temperature for various values of the fuel heating rate. The cases of no microcracking is also shown. The as-irradiated temperature, grain size and burnup are 1200 K, 10 μm and 0.1 at.%, respectively.

Figure 5.2 shows *FASTGRASS* results for transient fission-gas release versus fuel temperature during the ramp for five values of heating rate. Also shown is a scenario where microcracking has not been permitted to occur (for a 5°C/s ramp). In general, for the ramps with microcracking, the transient fission-gas release increases rapidly after fuel temperatures in the range of 1700 to 2000 K have been attained. The dependence of gas release on heating rate results from the combination of "time and temperature" and "increased mobility" phenomena. For relatively high heating rates (e.g., 200°C/s in Fig. 5.2), the gas release is limited owing to the short diffusion times of the intragranular fission gas. The gas release during these higher heating rate conditions comes mainly from the pretransient distribution of gas on the grain boundaries and edges. Again, the no microcracking scenario results in a much smaller prediction of transient fission-gas release.

The results of the calculations for TMI-2-type accident conditions shown in Figs. 5.1 and 5.2 were based on fuel irradiated to 0.1 at.% burnup. Figures

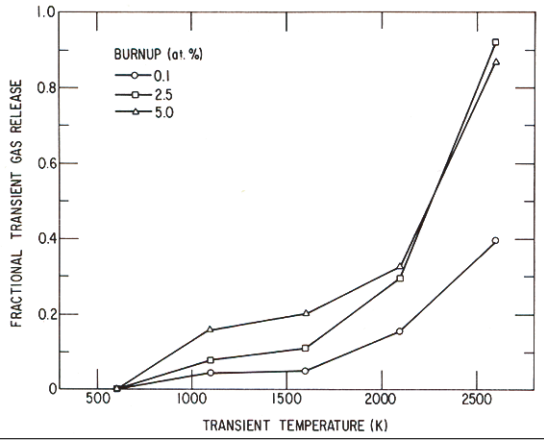

Figure 5.3: The *FASTGRASS* predictions of transient gas release versus fuel temperature for various values of fuel burnup with as-irradiated fuel temperature and grain size of 1200 K and 10 μm, respectively.

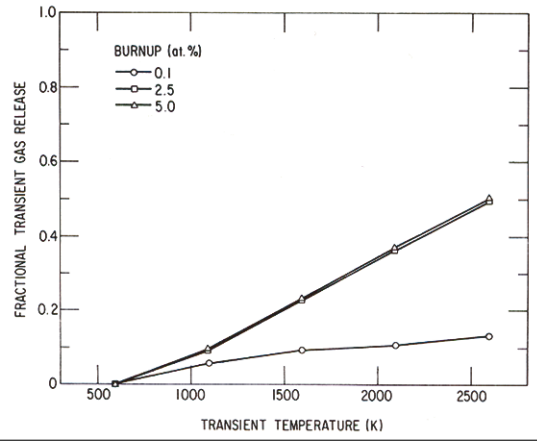

Figure 5.4: The *FASTGRASS* prediction of transient gas release versus fuel temperature for various values of the fuel burnup with as-irradiated fuel temperature and grain size of 2000 K and 10 μm, respectively.

5.3 and 5.4 show the results of *FASTGRASS* calculations of transient fission-gas release versus fuel temperature during the ramp for three values of the as-irradiated burnup and an average steady-state temperature of 1200 and 2000 K, respectively. The fuel heating rate and grain size were $5°C/s$ and 10 μ, respectively. As demonstrated in Figs. 5.3 and 5.4, the values of the as-irradiated average fuel temperature and burnup can have a significant effect on the transient fission-gas release for a given transient scenario. Fuels that have been irradiated at lower average temperatures (for a given burnup) or to a higher

burnup (for a given as-irradiated fuel temperature) have, in general, a higher fractional gas release during a subsequent transient. This burnup effect is related to the correspondingly larger concentration of intergranular fission gas that evolves during such an irradiation period. A larger concentration of intergranular fission gas prior to a transient increases the "gas release potential" in that a greater quantity of gas has a shorter diffusional distance to the exterior of the fuel, or in the case of microcracking, is directly available for release.

DEH tests

FASTGRASS was executed with a transient temperature code [30, 59] for a series of DEH tests. The calculation scenario is as follows (see Fig. 5.5): Based on the DEH test operating conditions, the radial transient temperature profile is calculated and is subsequently used for the calculation of the fission gas response. In turn, the fission gas behavior results are used for the calculation of fuel microcracking. If microcracking occurs, the fission-gas release, retention and swelling results are updated accordingly. Finally, the microcracking results are passed back to the transient temperature calculation where the thermal conductivity expression is modified, and the calculation proceeds to the next time step.

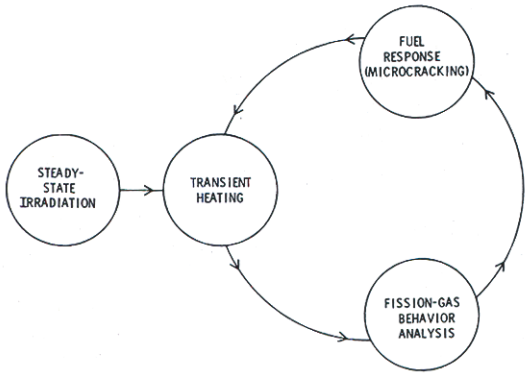

Figure 5.5: Interrelationship between fuel fracturing (microcracking), temperature scenario and fission gas bubble response.

Figures 5.6-5.8 show the prediction of the theory for pore-solid surface area per unit volume, S_v, as a function of pellet radius for DEH tests 22 and 32, 34 and 29, and 33 and 37, respectively, and measured values [30] of S_v for the same tests (the measured pore-solid surface is assumed to be produced mainly by fuel microcracking).

In general, considering the complexity (synergistic nature) of the phenomena and the relatively wide range of test conditions, the results of the theory are

in remarkably good agreement with the data. For example, there is reasonably good agreement between the theory and data for both test 33 and test 37 which had heating rates of 22 and 234 K/s, respectively (Fig. 5.8). The greatest discrepancy between theory and experiment occurs for test 22 (Fig. 5.6), where the theory underpredicts the data obtained near the center of the pellet by more than a factor of 2. The implication of this underprediction of fuel microcracking is that the calculated fuel temperatures will be low with a resultant underprediction of fission-product release (see Fig. 5.5). This scenario will be addressed in further detail in §5.4, below.

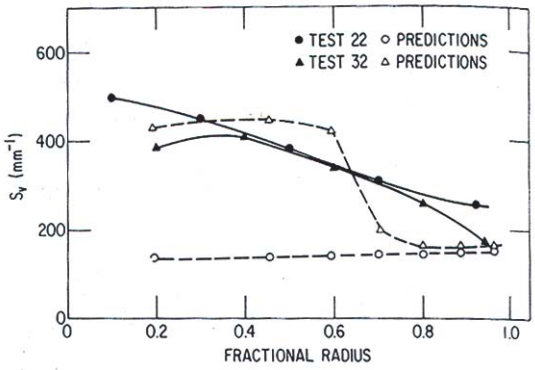

Figure 5.6: Predictions of pore-solid surface area, S_v, as a function of pellet radius for tests 22 and 32 compared with the data of Gehl[30].

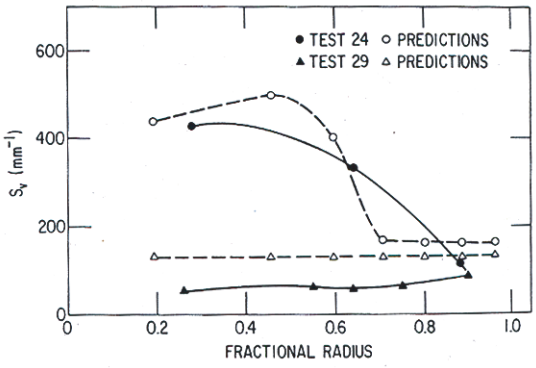

Figure 5.7: Predictions of pore-solid surface area, S_v, as a function of pellet radius for tests 24 and 29 compared with the data of Gehl[30].

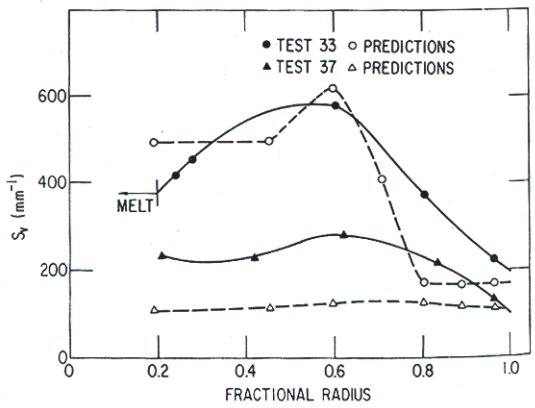

Figure 5.8: Predictions of pore-solid surface area, S_v, as a function of pellet radius for tests 33 and 37 compared with the data of Gehl[30].

5.2 Grain growth/grain-boundary sweeping

A theory of grain-boundary sweeping has been included within the *FAST-GRASS* formalism. This theory considers the interaction between the moving grain boundary and two distinct size classes of bubbles, those on grain faces and grain edges, and provides a means of determining whether gas bubbles are caught up and moved along by a moving grain boundary or whether the grain boundary is only temporarily retarded by the bubbles and then breaks away.

Speight and Greenwood[63] proposed a grain-growth theory which includes the sweeping of entrapped micro-bubbles by the front of an advancing grain boundary. The basic postulate of their theory is that small bubbles exert a minimal drag force on an advancing grain surface because of their higher drag. To assess the efficiency of bubble sweeping, they compared the magnitude of the force exerted by a bubble on the boundary, i.e.,

$$F_b = \pi R_b \gamma_{gb} \sin 2\phi \quad , \tag{5.2.1}$$

with the adhesive effects of the interfacial surface tension, i.e.,

$$F_{gb} = \frac{2\gamma_{gb}}{r_c} \pi r_{gb}^2 \quad , \tag{5.2.2}$$

where R_b is the bubble radius, r_c is the radius of curvature of the grain, $2r_{gb}$ is

the characteristic distance of bubble spacing, γ_{gb} is the grain boundary surface tension and ϕ is the angle of contact between the bubble and the boundary.

Whereas Speight and Greenwood considered the effects of the moving boundary interacting with a population of equal-sized bubbles, the present theory, includes the effects on the moving boundary of two distinct distribution of bubble sizes, those on the grain faces and those on the grain edges: the motion of the moving boundary is retarded by the presence of both grain-face and grain-edge bubbles. In addition, as *FASTGRASS* provides for a mechanistic calculation of intra- and intergranular fission product behavior, the coupled calculation between fission gas behavior and grain growth is kinetically comprehensive. The magnitude of the total force exerted by the bubbles on the boundary, or vice versa, depends on bubble radius and angle of contact according to the relationship

$$\begin{aligned} F_b &= \pi R_f B_f \gamma_{gb} \sin 2\phi_f + \pi R_e N_e \gamma_{gb} \sin 2\phi_e \\ &\equiv N_f F_f + N_e F_e \quad . \end{aligned} \tag{5.2.3}$$

F_f and F_e represent, respectively, the forces exerted by a grain-face and grain-edge bubble on the boundary, N_f and N_e are the respective number of bubbles on the grain faces and grain edges, R_f and R_e are the corresponding bubble radii, and ϕ_f and ϕ_e are the corresponding angles of contact between the bubbles and the boundary.

The velocity of these bubbles can be determined from the individual forces on the bubbles by utilizing the Nernst–Einstein equation. Assuming that the grain-face and grain-edge bubbles move by surface diffusion control, the velocity of these bubbles can be expressed as

$$V_f = \frac{D_f F_f}{kT} = \frac{3}{4} \frac{a_0^4 D_0}{R_f^3} \left(\frac{2\gamma_{gb}}{kT} \right) \sin 2\phi_f \exp \left[\frac{-E_s}{kT} \right] \quad , \tag{5.2.4}$$

and

$$V_e = \frac{D_e F_e}{kT} = \frac{3}{4} \frac{a_0^4 D_0}{R_e^3} \left(\frac{2\gamma_{gb}}{kT} \right) \sin 2\phi_e \exp \left[\frac{-E_s}{kT} \right] \quad , \tag{5.2.5}$$

where V_f and V_e, and D_f and D_e are the velocities and diffusion coefficients of the face and edge bubbles respectively, a_0 is the lattice constant, T is the absolute temperature, k is Boltzmann's constant, D_0 is the preexponential factor

for surface self-diffusion of the matrix solid, and E_s is the activation energy for this process.

In order to determine the contact angles ϕ_f and ϕ_e in Eqs. (5.2.4) and (5.2.5), the velocity of the moving grain boundary needs to be evaluated. At temperatures of about 1900 K, atomic mobilities in UO_2 result in an enhanced migration of atoms from the convex to the concave side of the boundary because in that location they are surrounded by a somewhat larger number of neighboring atoms and thereby exhibit a lower effective energy state. In other words, the net flux of atoms, J, across a curved grain boundary occurs because the binding energy of the atoms in the matrix is somewhat higher on the concave than on the convex side of the boundary. The net result of this atomic motion is shrinkage of small grains with predominantly convex surfaces and growth of larger grains with concave surfaces. The net flux of atoms across the boundary can be expressed as[1]

$$J = \frac{\nu}{a_0^2}\frac{\Delta E}{kT}\exp\left[-Q/kT\right] \quad , \tag{5.2.6}$$

where ν is the frequency of vibration of an atom in the solid lattice adjacent to the boundary, Q is the activation energy for grain boundary motion, and ΔE is the difference in energy between atoms located on the concave versus the convex side of the boundary. The velocity of the grain boundary, V_{gb}, is the product of the flux, J, and the atomic volume, which is approximately equal to the cube of the lattice constant:

$$V_{gb} = Ja_0^3 = \nu a_0\frac{\Delta E}{kT}\exp\left[-Q/kT\right] \quad . \tag{5.2.7}$$

The energy difference, ΔE, can be related to the intrinsic properties of the curved grain boundary and the sizes and number of gas bubbles attached to the boundary. In the absence of differential strain between adjacent grains, the intrinsic grain-boundary tension force is the primary force acting on the boundary, and acts to move the boundary toward the center of curvature of the convex grain. The grain-face and grain-edge bubbles exert a drag force in the opposite direction. If a section of grain boundary with area A_{gb} moves a distance $\mathrm{d}x$, the change in energy is

$$\left[\frac{2\gamma_{gb}}{r_c}\left(A_{gb}\right) - F_b\right]\mathrm{d}x \quad ,$$

where F_b is given by Eq. (5.2.3). The first term in the brackets in the above equation represents the adhesive effects of the interfacial surface tension, i.e., αF_{gb} of Eq. (5.2.2). The number of atoms displaced from one side of the boundary to the other is

$$A_{gb}\mathrm{d}x/a_0^3 \quad .$$

Dividing this expression into the preceding one gives the energy change per atom transferred across the boundary, ΔE:

$$\Delta E = \frac{2a_0^3\gamma_{gb}}{r_c}\left(1 - \frac{\pi R_f N_e r_c \sin 2\phi_f}{2A_{gb}} - \frac{\pi R_e N_e r_c \sin 2\phi_e}{2A_{gb}}\right) \quad . \tag{5.2.8}$$

Inserting Eq. (5.2.8) into Eq. (5.2.7) yields the grain boundary velocity

$$V_{gb} = \frac{2a_0^4\nu\gamma_{gb}}{r_c kT}\exp\left[-Q/kT\right]\left[1 - \frac{1}{2}\left(\frac{\pi R_f^2 N_f}{A_{gb}}\right)\left(\frac{r_c}{R_f}\right)\sin 2\phi_f \right. \\ \left. - \frac{1}{2}\left(\frac{\pi R_e^2 N_e}{A_{gb}}\right)\left(\frac{r_c}{R_e}\right)\sin 2\phi_e\right] \quad . \tag{5.2.9}$$

When the bubbles are widely spaced or very small, the second and third terms in the brackets in Eq. (5.2.9) are negligible compared to unity, and V_{gb} reduces to the intrinsic velocity of the curved grain boundary. The second and third terms in the brackets in Eq. (5.2.9) account for the retarding effects of the bubbles on grain-boundary motion.

If both the grain-face and grain-edge bubbles are swept along with the moving boundary then

$$V_f = V_e = V_{gb} \quad . \tag{5.2.10}$$

The first equality in Eq. (5.2.10) yields

$$\frac{\sin 2\phi_f}{R_f^3} = \frac{\sin 2\phi_e}{R_e^3} \tag{5.2.11}$$

From Eqs. (5.2.9) – (5.2.11), one obtains

$$\sin 2\phi_e = \left[\frac{3}{4} \frac{D_0 r_c}{R_e^3 \nu} \exp\left[-\frac{E_s - Q}{kT} \right] + \frac{1}{2} \left(\frac{\pi R_e^2 N_f}{A_{gb}} \right) \left(\frac{r_c}{R_e} \right) + \frac{1}{2} \left(\frac{\pi R_f^2 N_f}{A_{gb}} \right) \left(\frac{r_c}{R_f} \right) \left(\frac{R_f}{R_e} \right)^3 \right]^{-1} \quad . \tag{5.2.12}$$

Since $\sin 2\phi$ cannot exceed unity, the condition for bubble detachment is met when the RHS of Eq. (5.2.12) exceeds unity. If this condition is satisfied and $R_f = R_e$, both face and edge bubbles become detached from the boundary. If $R_f \neq R_e$, the larger bubble becomes detached (we assume for the sake of this discussion that $R_e > R_f$) and the condition that the smaller bubble be swept along with the moving boundary is examined by requiring

$$V_f = V_{gb} \quad ,$$

which results in

$$\sin 2\phi_e = \left[\frac{3}{4} \frac{D_0 r_c}{R_e^3 \nu} \exp\left[-\frac{E_s - Q}{kT} \right] + \frac{1}{2} \left(\frac{\pi R_f^2 N_f}{A_{gb}} \right) \left(\frac{r_c}{R_f} \right) \right]^{-1} \quad . \tag{5.2.13}$$

If the right hand side of Eq. (5.2.13) exceeds unity, then the smaller bubble (R_f in this case) is also detached from the boundary. If the RHS of Eq. (5.2.12) or (5.2.13) is less than unity, both face and edge bubbles, or just face bubbles, respectively, are swept along with the moving boundary. The contact angles ϕ_f and ϕ_e can be computed from Eqs. (5.2.11) – (5.2.13) and used in Eqs. (5.2.4) and (5.2.5) or (5.2.9) to determine the bubble or grain-boundary velocity.

As the boundary moves, the rate $\mathrm{d}C_{gb}/\mathrm{d}t$ at which fission products are swept up by the moving boundary is proportional to the rate of change of the volume of the grains, i.e.,

$$\frac{\mathrm{d}C_{gb}}{\mathrm{d}t} = \frac{\pi e C_I D_t^2}{2} \frac{\mathrm{d}D_t}{\mathrm{d}t} = \frac{\pi e C_I D_t^2 V_{gb}}{2} \quad , \tag{5.2.14}$$

where C_I is the *intra*granular concentration of a fission product, D_t is the grain diameter at time t, and e is a factor that describes the grain-boundary sweeping efficiency.

5.3 Mobility of fission gas bubbles under transient conditions

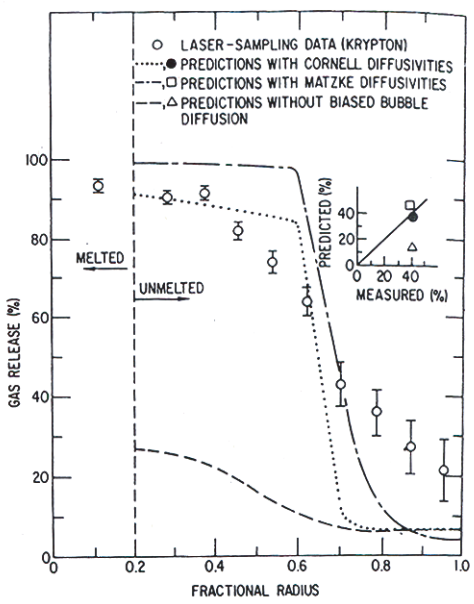

Figure 5.9: Transient gas release predictions of the theory, for various assumptions about gas-atom and gas-bubble mobility, compared with measured values.

Analyses with the *GRASS-SST* code[7] for steady-state conditions, coupled with experimentally determined fission-gas release during DEH tests, indicated that large quantities of gas are transported out of the UO_2 grains during transient heating. This release of fission gas from the grains is much greater than can be explained by empirical steady-state diffusivities measured under isothermal annealing conditions[7]. The model for bubble diffusion in *FASTGRASS* theory[4, 7, 11, 64] is unique in the sense that it relates the bubble diffusivities to the fuel yield stress, heating rate, and vacancy mobility, as well as to fuel temperatures and bubble radius.

MacInnes and Breary[65] have proposed a model for the release of fission gas from reactor fuel undergoing transient heating which utilizes an alternative release mechanism based on stationary bubbles and migration of gas by diffusion of single gas atoms. The essence of this model is that gas bubbles, which have previously been regarded as infinite sinks for gas atoms, can, in fact, accept only a few atoms before thermal emission of atoms dominates flow to the bubble. However, the successful application [65] of this thermal re-solution approach requires the assumption that the initial bubble radius is extremely

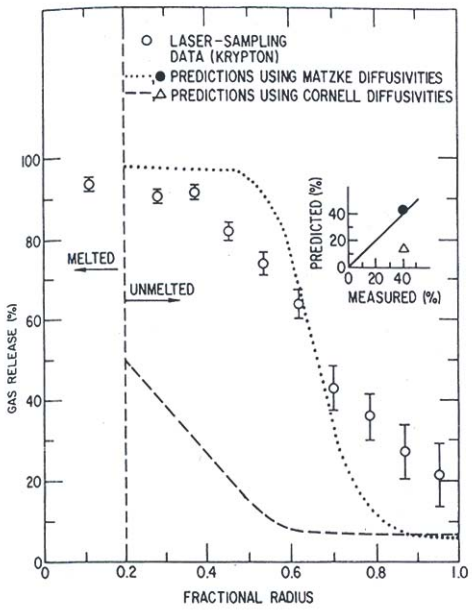

Figure 5.10: Transient gas release predictions of the theory, with the assumption of 100% thermal re-solution of intragranular gas and various values of gas-atom mobility, compared with measured values.

small ($\leq$ 0.5 nm), and values for the solution energy which are substantially smaller than have been determined theoretically[66].

In this section, the effect of changing the bubble mobility upon gas release during a thermal transient will be examined. Figure 5.9 shows the predictions of *FASTGRASS* theory for gas release from DEH test 33 as a function of fuel fractional radius, compared with the measured values (open circles). Also shown in Fig. 5.9 are the predicted vs. measured values of total gas release during this test. The dotted curve and solid circle in Fig. 5.9 show the predictions of the theory using gas-atom diffusivities based on the observations of Cornell[67]. (The theory of bubble mobility[4, 11] based on the assumption that surface diffusion is the rate-controlling process was used for the calculations shown in Fig. 5.9.) The upper curve and open square in Fig. 5.9 show predictions based on gas-atom diffusivities from Matzke[68]. Considering that the Matzke gas atom diffusivities are $\sim$100 times greater than those obtained by Cornell, the results in Fig. 5.9 indicate that the results of the theory for DEH transient heating test 33 are relatively insensitive to intragranular single-gas-atom diffusion.

The dashed curve and open triangle in Fig. 5.9 show predictions based on the Cornell gas-atom diffusivities and a constraint which precluded any biased bubble motion of the fission-gas bubbles. The random motion of gas bubbles

results in substantially lower predictions than those obtained without the constraint on biased bubble motion. Thus the results of Fig. 5.9 demonstrate that within the context of *FASTGRASS* theory, biased motion during transient heating conditions is a key mechanism of fission gas behavior.

Figure 5.10 shows the predictions of the theory for the same transient heating test conditions used in Fig. 5.9, but with the assumption of 100% thermal re-solution of gas atoms from bubbles during the transient. Thus, gas-atom diffusion is assumed to be the only mechanism whereby fission gas can migrate to the grain boundaries. The results shown in Fig. 5.10 demonstrate that without any bubble motion, 100% thermal re-solution and relatively high atom mobilities are required in order to obtain agreement between the theory and data. It should also be noted that the assumption of 100% thermal re-solution results in a prediction of zero microcracking for this test, in contrast to the substantial number of fractured boundaries observed (fuel microcracking was artificially simulated for these calculations in order to provide correct temperature profiles, see §5.4, below).

5.4 Fission gas release during transient conditions

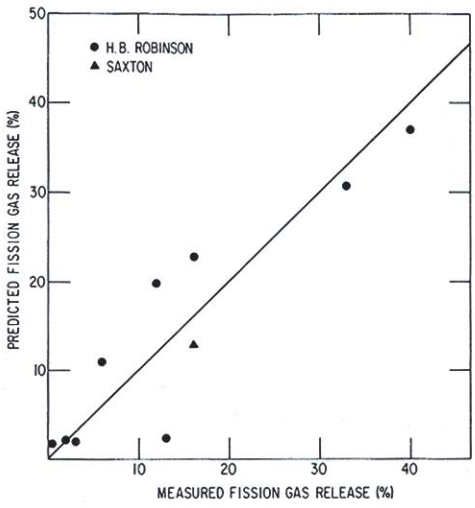

Figure 5.11: Predictions of the theory of transient gas release vs. experimentally measured values from DEH tests.

Figure 5.11 shows the predictions of the theory for transient fission gas release for 10 transient DEH tests on irradiated UO_2 fuel. Nine tests were on fuel irradiated in the HBR reactor and one test was on fuel irradiated under relatively

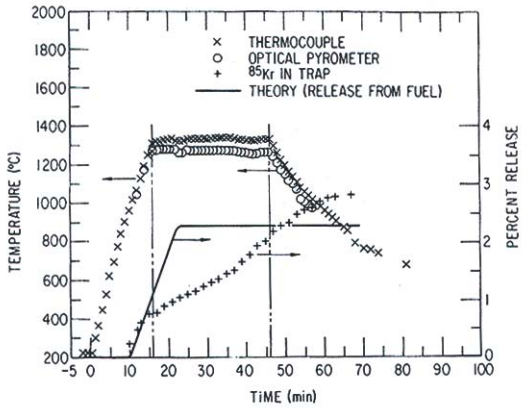

Figure 5.12: Predictions of the theory (solid curve) for noble gas release as functions of time and temperature, compared with the ^{85}Kr Data in test HI-1.

high-power, load-following conditions in the Saxton reactor[30]. The diagonal line in Fig. 5.11 indicates perfect agreement between theory and observation.

Except for test 22 (12% gas release measured), the predictions are in reasonable agreement with the measured values. There appears to be relatively uniform scatter of the predicted vs. the measured values on either side of the diagonal line, indicating random rather than biased uncertainties. Random uncertainties are most likely associated with the calculation of fuel temperatures. The complex synergism among radial heat flux, fuel microcracking and fission gas response has already been discussed in §5.1.1, above (see Fig. 5.5). In addition, the actual transient temperature profiles for the DEH tests contain asymmetries due to nonuniform heating associated with the inhomogeneity of the DEH test pellets. These asymmetries have not been quantified and were not included in the analysis of the DEH tests.

The theory predicts that 2.3% gas release occured during DEH test 22, as compared to the measured value of 13.1% (Fig. 5.11). As discussed in §5.1.1 above, and shown in Fig. 5.6, the theory underpredicts (by more than a factor of two near the pellet center) the amount of pore-solid surface area generated during DEH test 22 by fuel microcracking. Based on the discussion of the synergisms involved in the determination of radial heat flux (represented pictorially in Fig. 5.5), the underprediction of fuel microcracking should lead to underprediction of fuel temperatures and, hence, to an underprediction of fission-gas release. As relatively reasonable predictions for fuel microcracking were made for the other DEH tests (Figs. 5.6-5.8), the predictions for fuel temperatures and fission-gas release in those tests should also be reasonable (if the fission-gas response theory is accurate); indeed, they are, as demonstrated in Fig. 5.11.

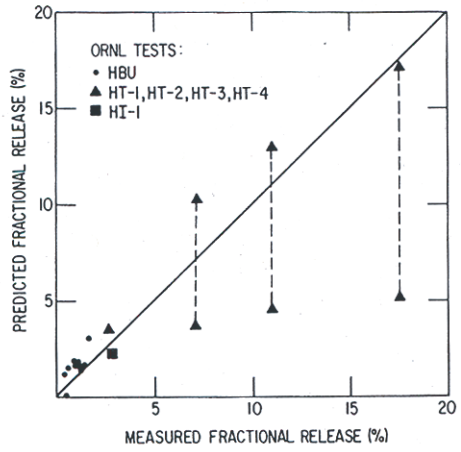

Figure 5.13: Predictions of the theory for transient gas release vs. experimentally measured values from the HBU, HT and HI tests.

Figure 5.12 shows the results of the theory for transient fission-gas release from UO_2 fuel (solid line) as a function of time and temperature for the HI-1 high-temperature transient test[60] performed at Oak Ridge National Laboratory (ORNL), compared with the measured values ($+$ symbols) for ^{85}Kr obtained from a downstream charcoal trap. Also shown in Fig. 5.12 are the measured fuel temperatures obtained by thermocouple and optical pyrometer. The ORNL tests were performed with high-burnup LWR fuel (from the HBR reactor) to explore the characteristics of fission-product release in a flowing steam atmosphere under a controlled loss-of-coolant accident (LOCA) over the temperature range 1400 to $\sim$2400°C. Earlier tests[69, 70], conducted under similar conditions, were performed at temperatures of 500 to 1600°C.

The results shown in Fig. 5.12 indicate that the theory predicts the release of ^{85}Kr during the HI-1 test in a flowing steam atmosphere reasonably well.

Fig. 5.13 shows the results of the theory for 10 ORNL transient fission-product release tests compared with the measured values[69, 70, 71]. The temperatures were ramped to values of 500 to 1600°C and held for various lengths of time before test termination. The diagonal line in Fig. 5.13 indicates perfect agreement between theory and experiment. In general, the agreement between theory and experiments is reasonable. A range of predicted values is shown for three tests in Fig. 5.13 and correspond to reported uncertainties[72] in the fuel temperatures during the test. The temperature uncertainties in these tests are attributed to the combined heat from rapid cladding oxidation and higher levels of ohmic energy deposition.

Chapter 6

Modeling the behavior of volatile fission products

The *FASTGRASS* code was designed, in large part, to model the time-dependent distribution and release of volatile fission products (VFPs) as well as alkaline-earth fission products (AEFPs). For simplicity, the term VFP will imply AEFP, unless otherwise stated. The fission-gas atom and bubble concentration relationships covered in Chapter 2 as well as the swelling and release mechanisms detailed in that chapter, form the physical foundation describing the behavior of VFPs. An accurate representation of these gases, however, requires a treatment of the chemical interaction between the various VFPs and the interaction between the VFPs and the fission-gas bubbles.

6.1 Volatile fission product chemistry

The *FASTGRASS* model for reactive VFP release is based on two major assumptions: (1) as the VFPs are known to react with other elements to form compounds, a realistic description of VFP release must include the effects of chemistry on behavior, and (2) as the noble gases have been shown to play a major role in establishing the interconnection of escape routes from the interior to the exterior of the fuel, a realistic description of VFP/AEFP release must include, a priori, a realistic description of fission gas release and swelling. The physical reasonableness of these assumptions has been supported, thus far, by good agreement between model predictions and actual observation.

Based on the work of Tam et al. [73], the following system of equations is used

to assess Cs and I sequestering behavior in UO2 fuel:

$$2\mathrm{Cs}(g) + \mathrm{UO_2}(c) + \mathrm{O_2}(g) \rightarrow \mathrm{Cs_2UO_4}(c) \quad , \tag{6.1.1}$$

$$2\mathrm{Cs}(g) + \mathrm{Mo}(c) + 2\mathrm{O_2}(g) \rightarrow \mathrm{Cs_2MoO_4} \quad , \tag{6.1.2}$$

$$\mathrm{Cs} + \mathrm{I} \rightarrow \mathrm{CsI} \quad , \tag{6.1.3}$$

where (g) and (c) designate gas and crystalline phases, respectively.

Tellurium (Te) is considered non-reactive within the fuel matrix. The physical basis for the primary reactions governing the chemical behavior of I and Cs in UO_2 -based fuel is reasonably well established and documented in the literature (Refs. [73, 74, 75]). However, the internal fuel rod chemistry governing Ba and Sr release is less certain and no mechanistic model exists at this time for the estimation of the release behavior of Ba and Sr, from severely damaged fuel. Rather, the release of these fission products is based solely on empirical correlations obtained from a limited data base. Here we postulate a basic for estimation of such Ba and Sr release.

Barium and strontium belong to the Group II (alkaline earth) elements. As discussed in Ref. [76], evidence indicates that Ba and Sr may be present in the fuel as simple oxides, uranates, molybdates, or zirconates. The simple oxides and the molybdates would be the most stable of these compounds; compounds formed with Sr tend to be more stable than the corresponding Ba compounds. In general, the formation of such compounds can be expected to immobilize Ba and Sr within the fuel matrix, and thus limit their release potential. Therefore, of particular interest with respect to release modeling is the establishment of a basis for estimating the amount of Ba and Sr that remains in the more mobile elemental form or in a vapor phase (e.g., within fission gas bubbles), versus the quantities of these fission products that react to form less volatile species.

A qualitative guide to the chemical state of fission product Ba and Sr in oxide fuel is their affinity for oxygen. The stability of fission product Ba and Sr as elements or as oxides in the presence of UO_2 depends on the difference between the free energy of the fission product oxide and the fuel oxygen potential. For fission product compounds with free energies below that of the fuel oxygen potential, an oxide is predicted; for compounds with free energies above that of the fuel oxygen potential, a stable element is predicted. Comparison of the oxygen potential of stoichiometric UO_2 fuel with the free energies of formation of Ba and Sr fission product oxides clearly indicates that Ba and Sr have a high propensity to form oxides. Stoichiometry also plays an important role: hyperstoichiometric fuel tends to show an enhanced potential for the formation of fission product oxides.

The Ba and Sr reactions of interest are as follows:

Barium	Strontium
$Ba + \frac{1}{2}O_2 \rightarrow BaO$	$Sr + \frac{1}{2}O_2 \rightarrow SrO$
$Ba + Zr + \frac{3}{2}O_2 \rightarrow BaZrO_3$	$Sr + Mo + 2O_2 \rightarrow SrMoO_4$
$BaO + Mo + \frac{3}{2}O_2 \rightarrow BaMoO_4$	$SrO + UO_2 + \frac{1}{2}O_2 \rightarrow SrUO_4$
$BaO + UO_2 + \frac{1}{2}O_2 \rightarrow BaUO_4$	

It should be noted that the alkaline earths also exhibit the potential to form iodides. However, since high-yield Cs has a higher free energy of formation with I than do Ba and Sr, the potential for CsI formation is greater, and tends to limit the formation of Ba and Sr iodides. Thus, for all practical purposes, the above reactions can be expected to control the internal fuel rod chemistry of Ba and Sr. The free energies of formation, ΔG, for some of the above reactions, and for several relevant Cs reactions, are presented in Table 6.1; they are based upon values suggested in Ref. [77].

In addition to the formation of oxides, uranates, molybdates, and zirconates, which can be expected to be dispersed throughout the fuel matrix, evidence exists that Ba and Sr may aggregate into inclusions which effectively form a separate phase within fuel (i.e., physical and chemical properties determined by inclusion composition rather than fuel properties). However, the consensus of various researchers is that both Ba and Sr, in normally irradiated fuel, exist primarily in the fuel matrix in oxide form and not as a prime constituent of metallic inclusions. Because of uncertainties in composition, oxidation state, homogeneity, and the indication that Ba and Sr are not major inclusion constituents, Ba and Sr holdup via metallic inclusion sequestering will not be considered in this analysis. Indeed, one would expect that inclusions containing Ba and Sr would be primarily of the oxide form rather than metallic.

Equilibrium fission product distributions for the various phases of the fuel/fission-product system at 1500 K have been calculated[76, 77]. The calculations are based on UO_2 fuel at 2 at.% burnup, an oxygen-to-uranium ratio that is slightly hyperstoichiometric, and a 10% void volume in the fuel. Such an equilibrium distribution may not be achieved at 1500 K in a transient sequence, since the release of the fission products to voids and bubbles may be too slow. Moreover, the estimates of solutions of fission product oxides in urania are based on sparse data. In spite of these limitations, thermochemical equilibrium calculations indicate that the most probable distribution of Ba and Sr in the UO_2 is as follows:

Barium partitioning in UO_2		Strontium partitioning in UO_2	
BaO	59%	SrO	96%
$BaZrO_3$	35%	$SrMoO_4$	4%
$BaMoO_4$	4%		
$BaUO_4$	2%		

In view of the thermochemical conditions in fissioned UO_2 fuel discussed above, *FASTGRASS* assumes that the following reactions dominate Sr and Ba sequestering effects within the UO_2 matrix:

$$\mathrm{Sr}(s) + \tfrac{1}{2}\mathrm{O}_2(g) \rightarrow \mathrm{SrO}(c) \quad , \tag{6.1.4}$$

$$\mathrm{SrO}(c) \rightarrow \mathrm{SrO}(g) \quad , \tag{6.1.5}$$

$$\mathrm{Ba}(s) + \tfrac{1}{2}\mathrm{O}_2(g) \rightarrow \mathrm{BaO}(c) \quad , \tag{6.1.6}$$

$$\mathrm{BaO}(c) \rightarrow \mathrm{BaO}(g) \quad , \tag{6.1.7}$$

$$\mathrm{UO}_2(c) + \mathrm{BaO}(c) + \tfrac{1}{2}\mathrm{O}_2(g) \rightarrow \mathrm{BaUO}_4 \quad , \tag{6.1.8}$$

where (s) represents atoms in solution, and (c) and (g) represent crystalline and gas phases, respectively.

For the Sr and Ba reactions, the concentration of nine chemical species [Sr, SrO(c), SrO(g), OM_2, Ba, BaO(c), BaO(g), $BaUO_4$(c), and UO_2] must be determined in order to specify the fraction of fission product Sr and Ba that is available for release from the fuel matrix either in atomic form, or as an oxide. Six additional chemical species result from the I and Cs reactions (I, Cs, CsI, Cs_2UO_4, Cs_2MoO_4, and Mo). From the law of mass balance, the total fractional atom concentration of Sr, Ba, Cs, I, and Mo equals the sum of their respective fission yields, i.e.,

$$C^{\mathrm{T}}_{\mathrm{Sr}} = C_{\mathrm{Sr}} + C_{\mathrm{SrO}(c)} + C_{\mathrm{SrO}(g)} = 0.0926B \quad , \tag{6.1.9}$$

$$C^{\mathrm{T}}_{\mathrm{Ba}} = C_{\mathrm{Ba}} + C_{\mathrm{BaO}(c)} + C_{\mathrm{BaO}(g)} + C_{\mathrm{BaUO_4}} = 0.0682B \quad , \tag{6.1.10}$$

$$C^{\mathrm{T}}_{\mathrm{Cs}} = C_{\mathrm{Cs}} + C_{\mathrm{CsI}} + 2C_{\mathrm{Cs_2UO_4}} + 2C_{\mathrm{Cs_2MoO_4}} = 0.1882B \quad , \tag{6.1.11}$$

$$C^{\mathrm{T}}_{\mathrm{I}} = C_{\mathrm{I}} + C_{\mathrm{CsI}} = 0.011B \quad , \tag{6.1.12}$$

$$C^{\mathrm{T}}_{\mathrm{Mo}} = C_{\mathrm{Mo}} + C_{\mathrm{Cs_2MoO_4}} = 0.2348B \quad , \tag{6.1.13}$$

where C^{T}_i = total fractional concentration of species i (e.g., Sr, Ba) generated as a function of fractional burnup B, and C_i = fractional concentration of the

Reactants [a]	Product	Free energy, ΔG (cal/mol product)		Temperature (K)
Barium				
$Ba(c) + \frac{1}{2}O_2(g)$	$BaO(c)$	-117713	$+16.7T$	298-983
$Ba(l) + \frac{1}{2}O_2(g)$	$BaO(c)$	-133186	$+24.56T$ [b]	983-2122
$Ba(c) + \frac{1}{2}O_2(g)$	$BaO(g)$	-31367	$-12.95T$	298-983
$Ba(l) + \frac{1}{2}O_2(g)$	$BaO(g)$	-38373	$-6.76T$	983-2268
$BaO(c)$	$BaO(g)$	98138	$-33.21T$	-
$Ba(c) + U(c) + 2O_2(g)$	$BaUO_4(c)$	-473010	$+87.3T$	298-1403
$UO_2(c) + BaO(c) + \frac{1}{2}O_2(g)$	$BaUO_4(c)$	-81517	$+22.32T$	-
Strontium				
$SrO(c)$	$SrO(g)$	135344	$-36.42T$	298-2938
$SrO(c) + \frac{1}{2}O_2(g)$	$SrO(c)$	-141156	$+22.92T$	298-1041
$SrO(l) + \frac{1}{2}O_2(g)$	$SrO(c)$	-142835	$+24.55T$	1041-1654
$SrO(g) + \frac{1}{2}O_2(g)$	$SrO(c)$	-174079	$+43.44T$	1654-2938
Cesium				
$Cs(g) + I(g)$	$CsI(g)$	-73041	$+ 15.81T$	-
$2Cs(g) + UO_2(c) + O(g)$	$Cs_2UO_4(c)$	-233152	$+91.62T$	-
$2Cs(g) + Mo(c) + 2O_2(g)$	$Cs_{Mo}O_4(g)$	-325372	$+86.52T$ [c]	952-2892

[a] (c), (g), and (l) designate crystalline, gas, and liquid phases, respectively.
[b] The value of ΔG listed in Ref. [77] is incorrect.
[c] The value of ΔG used in this analysis is $\Delta G = -297715 + 79.166T$.

Table 6.1: Free energy formation of Ba and Sr fission product oxides

individual chemical forms of species i. The concentrations of O_2 and UO_2 can be assessed from standard models as a function of temperature, O/U ratio, burnup, and fuel density; thus, seven of the fifteen concentrations are known. The eight remaining equations can be obtained from the law of mass action. For the reaction(s) $Sr + \frac{1}{2}O_2(g) \rightarrow SrO(c)$, Eq. (6.1.4), the equilibrium constant, K_1, can be expressed in terms of the free energy of formation, ΔG, and the concentration of the reactants and products; i.e.,

$$K_1 = \exp\left[\frac{-\Delta G_1}{RT}\right] = \frac{a_{SrO(c)}}{C_{Sr} P_{O_2}^{1/2}} \quad , \tag{6.1.14}$$

where ΔG_1 is obtained from Table 6.1; P_{O_2} is the oxygen partial pressure; and $a_{SrO(c)}$ is the activity of SrO(c). For the reaction $Ba(s) + \frac{1}{2}O_2(g) \rightarrow BaO(c)$, Eq. (6.1.6), the equilibrium constant, K_2, can be similarly expressed as

$$K_2 = \exp\left[\frac{-\Delta G_2}{RT}\right] = \frac{a_{\mathrm{BaO}(c)}}{C_{\mathrm{Ba}} P_{\mathrm{O_2}}^{1/2}} \quad . \tag{6.1.15}$$

The remaining six equations [Eqs. (6.1.1)-(6.1.3), (6.1.5), (6.1.7)-(6.1.8)] can be expressed in terms of the corresponding free energies of formation and concentrations of the reactants and products in a similar manner.

In order to utilize the free energies given in Table 6.1 for the reactions described by Eqs. (6.1.4) and (6.1.6), one needs to know the corresponding solution energies for Ba and Sr. The values used in this analysis for Ba and Sr are $46,700$ and $33,000$ cal/mol, respectively.

The activities of the various reaction products in a condensed phase can be written as an activity coefficient times the concentration of the reaction product [e.g., $a_{\mathrm{BaO}(c)} = \alpha_{\mathrm{BaO}(c)} C_{\mathrm{BaO}(c)}$]. It is assumed that all the condensed-phase Ba, Sr and Cs reaction products are distributed uniformly within the UO_2 matrix, so that $\alpha_i = 1$, where i denotes the particular reaction product. Following the analysis of CsI formation in UO_2 given by Cronenberg and Osetek[78, 79] it is assumed that the formation of the reaction products CsI(g), SrO(g), and BaO(g) requires the presence of reaction sites, which are primarily microbubbles containing the noble fission gases Xe and Kr.

The activities of the gas-phase reaction products [i.e., CsI(g), BaO(g), and SrO(g)] are equal to their corresponding partial pressures, P_{CsI}, P_{BaO}, and P_{SrO}. Once these partial pressures have been calculated, they can be used in conjunction with an equation of state of the van der Waals form,

$$P\left(V_b - b\right) = nRT \quad , \tag{6.1.16}$$

[where b is the van der Waals constant, V_b is the bubble volume, and n is the number of atoms of CsI(g), SrO(g) or BaO(g) in the bubble in atoms $\cdot$ cm^{-3}], to calculate the quantity of CsI(g), SrO(g) and BaO(g) in the material. As the bubble volume, V_b, is calculated directly in *FASTGRASS* , there are no remaining unknowns in this calculation.

The oxygen partial pressure is calculated according to the analysis of Blackburn and Johnson[77], and is given by the following expression:

$$P_{\mathrm{O_2}}^{1/2} = \frac{(\phi - 2) + \left[(\phi - 2)^2 + 4B\,(3 - \phi)\,(\phi - 1)\,/A\right]^{1/2}}{2B\,(3 - \phi)\,/\phi} \quad , \tag{6.1.17}$$

where $A = \exp\left[78300/T - 13.6\right]$, $B = \exp\left[16500/T - 5.1\right]$, and ϕ = O/U.

The value of ϕ can be calculated by taking into account the fissioning of ^{235}U and the formation of the oxides and uranates given in Eqs. (6.1.1)-(6.1.8), i.e.,

$$\phi = \phi_0 + \frac{\dot{f}t}{N_{\mathrm{m}}^0}\left(\phi - \alpha\right) - \alpha \quad , \tag{6.1.18}$$

where $\alpha = C_{\mathrm{SrO}(c)} + C_{\mathrm{SrO}(g)} + C_{\mathrm{BaO}(c)} + C_{\mathrm{BaO}(g)} + C_{\mathrm{BaUO_4}} + 2C_{\mathrm{Cs_2UO_4}} + 4C_{\mathrm{Cs_2MoO_4}}$, N_{m}^0 is the initial number of heavy metal atoms, t is the irradiation time, and ϕ_0 is the starting O/U ratio. In general, as $\dot{f}$ and T are functions of time, Eq. (6.1.18) is phrased in differential form and integrated over time.

Simultaneous solution of this coupled system of equations (specifically, Eqs. (6.1.1)-(6.1.13),(6.1.17),(6.1.18)) yields the equilibrium concentrations as a function of fuel burnup and temperature. The amount of Sr and Ba that is predicted to be retained in the fuel in atom form or in the vapor phase in microbubbles is assumed available for release, whereas all other species are assumed to be immobilized within the fuel microstructure.

Once the fraction of atomic Sr and Ba are known, their mobility through the fuel microstructure is assessed. CsI(g), BaO(g) and SrO(g) are assumed to migrate within fission gas bubbles. The migration of atomic I, Cs, Ba, and Sr are handled in an analogous fashion to that of the noble gases: the concentrations of these species within the grains and on the grain boundaries are described using equations of the form shown by Eq. (3.2.1). Cs, I, Sr and Ba gas atom diffusivities are taken to be the same as that of Xe. The specific variables associated with these equations are defined in a table analogous to Table 3.1. The actual table in question is found in [17], pg. 205. These calculations for fission product chemistry and migration are performed sequentially, as a function of time. This method of calculating VFP behavior is reasonable as long as the integration time steps are chosen small enough so that a quasi-chemical equilibrium is maintained.

6.2 Fission-product release during normal operating conditions

Figure 6.1 shows *FASTGRASS* -predicted fractional release of iodine (^{131}I + ^{133}I) as a function of irradiation time, and compares these results with the data of Turnbull and Friskney[29]. To reflect the experimental uncertainty in temperature reported in Ref. [29], three predicted curves are given in each figure,

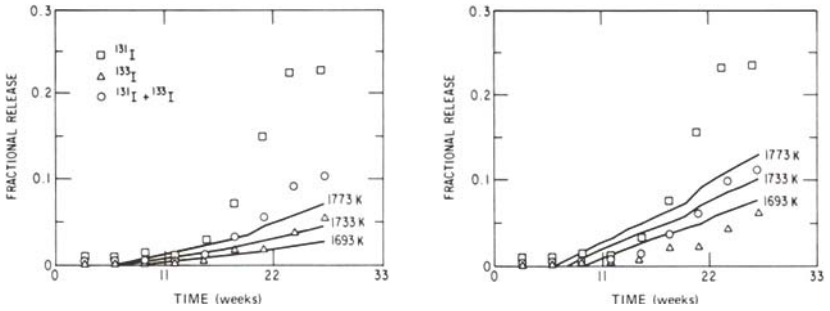

Figure 6.1: A *FASTGRASS* -predicted fractional release of ^{131}I + ^{133}I at 1733$\pm$40 K (solid curves), compared with data of Turnbull and Friskney[29] (symbols). The *FASTGRASS* predictions are based on two different assumptions about the diffusion of atomic iodine: (a) it diffuses intragranularly through the solid UO_2 and (b) it diffuses with CsI in fission gas bubbles.

corresponding to irradiation temperatures of 1733 ± 40 K. The circles in Figs. 6.1a and 6.1b represent the fractional release of iodine (^{131}I + ^{133}I) calculated from the data by taking into account the respective fission yields of ^{131}I and ^{133}I. The predictions of Fig. 6.1a a are based on the assumptions that (1) atomic iodine (i.e., iodine that is not predicted to be bound up as CsI) diffuses intragranularly through the solid UO_2 and (2) CsI migrates in fission gas bubbles: in Fig. 6.1b, the atomic iodine is assumed to migrate intragranularly with the CsI in fission gas bubbles, instead of diffusing through the solid as an individual species. A comparison of the curves in Figs. 6.1a and 6.1b shows that the latter assumption leads to higher total iodine release predictions than calculations performed with the assumption that the atomic iodine diffuses intragranularly independent of the fission gas. The reason for this result is that the xenon (and krypton) gas bubbles (predicted average-size bubble diameter $\simeq 25$ Å) diffuse to the grain boundaries at a faster mass-transfer rate than the diffusing iodine atoms and, hence, provide a relatively faster iodine release rate to the grain faces. The iodine atomic species diffuses to the grain faces at a slower mass-transfer rate than these smaller gas bubbles because the effective iodine generation rate is a factor of $\sim$30 less than that for the noble gases. Presumably, the real situation is somewhere in between the curves in Figs. 6.1a and 6.1b (i.e., a certain fraction of atomic iodine is captured in intragranular fission-gas bubbles). However, the assumption that both atomic iodine and CsI diffuse predominantly in gas bubbles gives the best overall agreement with the data. In addition, this particular assumption is more consistent with the general assumption of quasi-chemical equilibrium. Because of the much higher diffusivity of atomic cesium as compared to the noble gases, it is assumed that the predominant intragranular migration mechanism for atomic cesium is solid-state diffusion as an individual species.

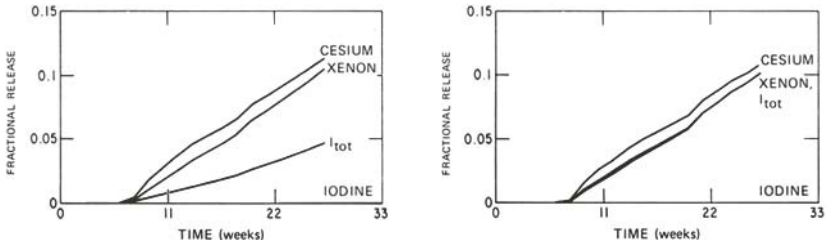

Figure 6.2: A *FASTGRASS* -predicted fission-product release at 1733 K. The curves in (a) and (b) are based on the same assumptions as 6.1a and 6.1b, respectively.

The iodine release data shown in Figs. 6.1a and 6.1b do not provide any information on the chemical form of the released iodine. The *FASTGRASS* calculations shown in Figs. 6.1a and 6.1b represent the sum of the released atomic iodine and the iodine released as the compound CsI.

Figures 6.2a and 6.2a show *FASTGRASS* -predicted fission product release at 1733 K for xenon, cesium, atomic iodine (I), and total iodine, based on the assumptions of Figs. 6.1a and 6.1b, respectively. As is shown in Figs. 6.2a and 6.2b, the release of iodine is predicted to occur mainly as CsI (i.e., the difference between I_{tot} and I). This result indicates that at the average operating temperature of 1733 K utilized for the calculations shown in Figs. 6.1a and 6.1b, serious error is introduced when the formation of CsI is neglected in the analysis.

Again, the assumption that atomic iodine migrates intragranularly with CsI in fission gas bubbles (Fig. 6.2b) results in a higher total-iodine release at 1733 K than the assumption that the iodine atoms diffuse as an individual species through the solid UO_2 (Fig. 6.2a). In fact, under the assumption of Fig. 6.2b (iodine migrates with CsI in fission gas bubbles), total iodine fractional release is almost identical with the fractional release of the stable fission gases. This result is in agreement with the observation of Appelhans and Turnbull[80] that the total-iodine release is similar to the noble gas release at relatively low temperatures and burnup. It is interesting to note that in Turnbull and Friskney's analysis of these experiments, no account of the chemical form of the iodine was included. Based on the *FASTGRASS* analysis, it can be concluded that neglecting fission product chemistry (e.g., the formation of CsI) in the interpretation of the data shown in Fig. 6.1 could result in quite misleading conclusions about the mechanisms of VFP release. Subsequent analyses (e.g., Refs. [81, 82]) have also neglected to include the effects of fission product chemistry.

The calculations shown in Figs. 6.1 and 6.2 were repeated, but with the effects of the formation of Cs_2UO_4 and Cs_2MoO_4 neglected. The resulting CsI formation will then be independent of the starting O/M and, consequently, of the oxygen potential. The results showed that in the temperature and burnup

range utilized in Figs. 6.1 and 6.2, neglecting Cs_2UO_4 and Cs_2MoO_4 formation has very little effect on the predicted form and amount of iodine release. Thus, the growing instability of Cs_2UO_4 and Cs_2MoO_4 at these temperatures decreases the efficiency of these compounds as strong sinks for cesium. At 1733 K, 3% of the retained cesium is predicted to occur as Cs_2UO_4 and Cs_2MoO_4 compounds.

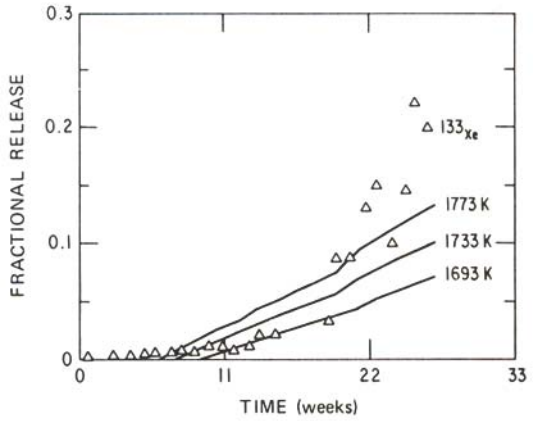

Figure 6.3: A *FASTGRASS* -predicted fractional release of the total stable noble gases at 1733 ± 40 K (solid curves), compared with the ^{133}Xe data of Turnbull and Friskney[29] (symbols).

Figure 6.3 shows *FASTGRASS* -predicted fractional release of stable xenon as a function of time, and compares it with the data for ^{133}Xe from Ref. [29]. Again, the three predicted curves reflect the ± 40 K uncertainty in irradiation temperature. The agreement between prediction and data is good for the first 20 weeks of irradiation, but *FASTGRASS* underpredicts ^{133}Xe release during the last 7 weeks of the irradiation. The reason for this discrepancy is unclear at present. However, it should be noted that *FASTGRASS* currently calculates only the behavior of the stable fission gases, and the comparison between the predicted fractional releases of total stable gases and the data for ^{133}Xe (a 5.25day half-life) as shown in Fig. 6.3 may reflect the qualitative and quantitative differences in behavior between the total stable gases and ^{133}Xe. This requires further study. A comparison of Figs. 6.1 and 6.3 shows that the predicted fractional release of iodine (^{131}I + ^{133}I) qualitatively follows that of the stable fission gases; as outlined above, this agrees with the data of Turnbull and Friskney reported in Ref. [29]. However, the fractional release behavior of ^{131}I, in contrast to the behavior of ^{133}I (and the sum of ^{131}I and ^{133}I), differs qualitatively from that of the noble gases. Presumably, this effect is due to enhancement of ^{131}I release through grain boundary diffusion[29].

6.3 Fission-product release during transient heating conditions

Previous *FASTGRASS* studies on the behavior of fission gases during transient conditions have resulted in the identification of the as-irradiated condition of the fuel (e.g., fuel burnup), the fuel microstructure (e.g., grain size), and the transient scenario (e.g., the fuel heating rate) as the key variables affecting fission gas response. Well-characterized data on VFP release during transient conditions are not currently available. In this study, the *FASTGRASS* code was used to examine the effect of as-irradiated fuel temperature and burnup, transient temperature and heating rate, and fission product chemistry (i.e., the effect of Cs_2UO_4 and Cs_2MoO_4) on the chemical form (e.g., iodine, cesium, and CsI) of the released fission products, as well as on the relative magnitude of the VFP release during transient heating conditions. Based on the analyses presented in §6.2, it is assumed that atomic iodine and CsI migrate intragranularly in fission gas bubbles, and that atomic cesium diffuses intragranularly through the solid UO_2 as an individual species.

6.3.1 Effect of fuel heating rate on fission-product release

Figures 6.4a and 6.4c show *FASTGRASS* predictions for xenon, iodine, cesium, and I_{tot} irradiated at 1500 K to 1.0 at.% burnup during a transient heatup from 1500 to ∼3000 K at 0.1, 1.0, and 10.0 K/s, respectively. The end-of-life results shown in the plot (at 1500 K) are again in qualitative agreement with the observations reported by Appelhans and Turnbull[80] (i.e., the iodine release is similar to the noble gas release at relatively low temperatures and burnup; see also §6.2). A comparison of Figs. 6.4a, 6.4b, and 6.4c shows that at 1 at.% burnup, the effect of an increase in heating rate from 0.1 to 1 K/s is to reduce the total fractional iodine release (as well as cesium and fission-gas release) through the majority of the transient; only at ∼3000 K does the total iodine release at 1 K/s approach that predicted to occur at 0.1 K/s. In addition, the fractional release of CsI is substantially lower in the 1 K/s case than for 0.1 K/s. The fractional release of atomic iodine in the 1 K/s case exceeds that predicted to occur for 0.1 K/s after fuel temperatures on the order of 2700 K have been achieved.

The reduction in CsI release at the higher rate of heating is due, in part, to the shorter transient time and the associated reduction in the development of pathways on the grain faces and along the grain edges to the exterior of the fuel (i.e., intergranular pathways to preexisting cracks or pellet/pellet interfacial regions; see §2.1.3). The latent development of these pathways prevents substantial release of the gaseous and VFPs until substantial fuel temperatures (∼2600 K) have been attained. The ratio of the amount of CsI to atomic iodine in chemical equilibrium at these relatively high fuel temperatures is reduced

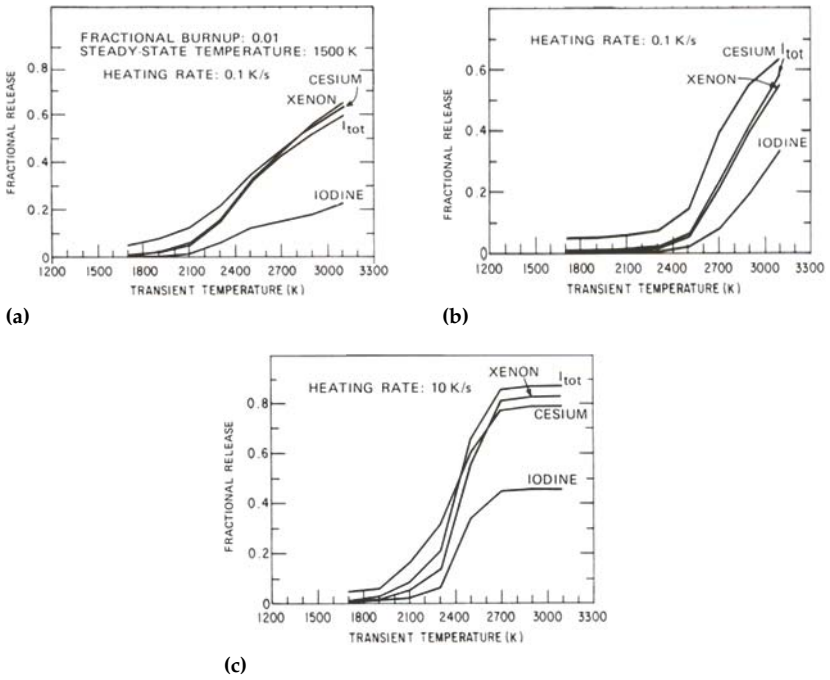

Figure 6.4: A *FASTGRASS* -predicted transient fission-product release for fuel heating rates of (a) 0.1, (b) 1.0, and (c) 10.0 K/s, respectively.

from the corresponding amount in equilibrium at lower temperatures ($\sim$2100 K). Hence, when enhanced iodine release begins to occur in the 1 K/s case at $\sim$2600 K (Fig. 6.4b), the amount of available CsI in the fuel is substantially less than the amount available at $\sim$2100 K, the temperature at which enhanced CsI release begins to occur in the 0.1 K/s case (Fig. 6.4a). On the other hand, the amount of available atomic iodine at $\sim$2600 K is greater than that available at $\sim$2100 K so that in the 1 K/s case, a greater fraction of the total iodine release has occurred as atomic iodine.

The development of intergranular pathways at fuel temperatures on the order of 2600 K in the 1 K/s case includes a substantial contribution from grain boundary separation (microcracking), as shown in Fig. 6.5. In Fig. 6.5, the fraction of the total grain boundary area which has undergone fracture is plotted as a function of transient temperature for fuel heating rates of 0.1, 1.0, and 10.0 K/s. No grain boundary separation is predicted to occur in the 0.1 K/s case. (In a previous study described in Ref. [11], extensive grain boundary separation is predicted to occur for 0.1 K/s heatups. However, the accident scenario for the earlier study was of the TMI-2 type, i.e., as-irradiated fuel temperatures dropped rapidly to $\sim$800 K before fuel heatup occurred. This scenario is in contrast to the one in the present study in which the heatup occurs without a

reduction in the fuel temperatures. These heatups are more representative of a transient overpower. In the earlier TMI-2-type scenario, the majority of the microcracking occurred at 0.1 K/s before fuel temperatures on the order of 1200 K had been reached.) For the 1 K/s case, grain boundary separation begins to occur at ∼2700 K and climbs rapidly until 58% of the available grain boundary area has undergone fracture. The reason for the grain boundary separation at 1.0 K/s is that at this level of heating rate and temperature, the fission gas bubbles arriving at the grain boundaries are in an enhanced state of nonequilibrium and overpressure, and hence have more of a tendency to propagate as cracks than to retain an equilibrium shape. (The *FASTGRASS* models for the diffusion of overpressurized fission gas bubbles (§5.3 and §A) and fuel microcracking (§5.1.1) have been described previously.)

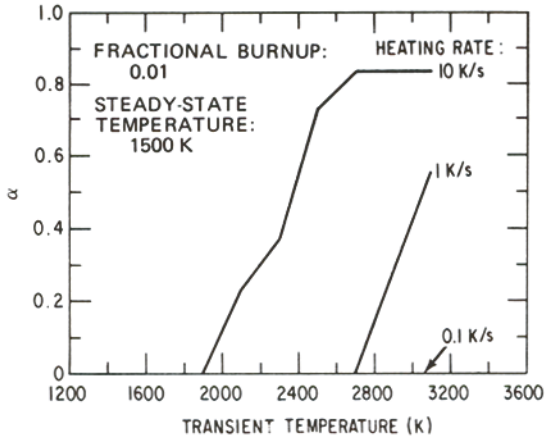

Figure 6.5: A *FASTGRASS* -predicted fraction of total grain boundary area per unit volume which has fractured (α), for fuel heating rates of 0.1, 1.0 and 10.0 K/s.

A comparison of Figs. 6.4a, 6.4b, and 6.4c shows that the fission product release values at 10.0 K/s are, in general, much greater than at 0.1 or 1.0 K/s. The greater release at 10.0 K/s is a result of (1) increased gas bubble mobility due to enhanced nonequilibrium conditions (see §A) and the associated formation of pathways through the solid UO_2 to the fuel exterior and (2) the increased rate of microcracking predicted to occur at 10.0 K/s (Fig. 6.5). The onset of enhanced fission product release shown in Fig. 6.4c at ∼1900 K correlates well with the onset of extensive microcracking (Fig. 6.5). Based on previous analyses[11], one would expect that as the heating rate were further increased, a point would be reached (∼25 K/s) where the fission product release would start to decrease. This would be due to a combination of a saturation of the enhanced mobility phenomena and the shortness of the transient time.

Figures 6.4a, 6.4b, and 6.4c show that the total iodine release is closely correlated with the predicted noble gas release. Again, as described in §6.2, the

similarity between the total-iodine release and the noble gas release is due to the assumption that both atomic iodine and CsI travel predominantly in fission gas bubbles. On the other hand, the form of the iodine release is not, in general, closely correlated with the noble gas release, as the determination of the chemical form of the iodine is complicated by cesium chemistry (i.e., formation Of CsI, Cs_2UO_4 and Cs_2MoO_4).

6.3.2 Effect of as-irradiated fuel burn-up on fission-product release

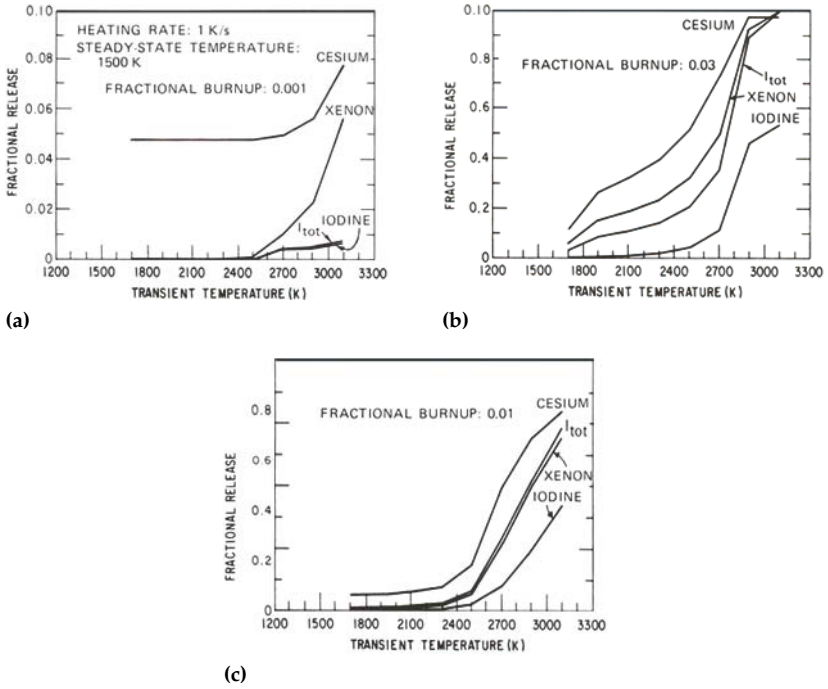

Figure 6.6: A *FASTGRASS* -predicted transient fission-product release at (a) 0.001, (b) 0.01, and (c) 0.03 fractional burn-up, respectively.

Figures 6.6a, 6.6b, and 6.6c show *FASTGRASS* predictions for VFP and noble gas release during a 1.0 K/s heatup from 1500 K for as-irradiated burnups of 0.1, 1, and 3 at.%, respectively. A comparison of Figs. 6.6a, 6.6b, and 6.6c shows that fission product release increases with increasing burn-up. The increased transient fission product release with increased as-irradiated burn-up is due, in part, to the more extensive network of pathways, which results, in general, from increased fuel burnups. Figure 6.7 shows the predicted grain boundary separation versus transient temperature for the three burnups under consideration. The predicted microcracking increases dramatically with burn-up. In

addition, the temperature at which the microcracking initiates decreases with an increase in burn-up. Again, the reason for this behavior is linked to the increased development of fission gas bubbles on the grain boundaries at the higher fuel burnups.

The fraction of iodine released as CsI during the transient also increases with burn-up. Because enhanced release begins at lower transient temperatures for higher values of as-irradiated burn-up (Figs. 6.6a, 6.6b, and 6.6c), and because the relative amount of iodine present as CsI is greater at the lower temperatures, the higher burn-up fuel releases the available CsI earlier in the transient before the higher temperatures are reached, and the CsI availability has been appreciably reduced.

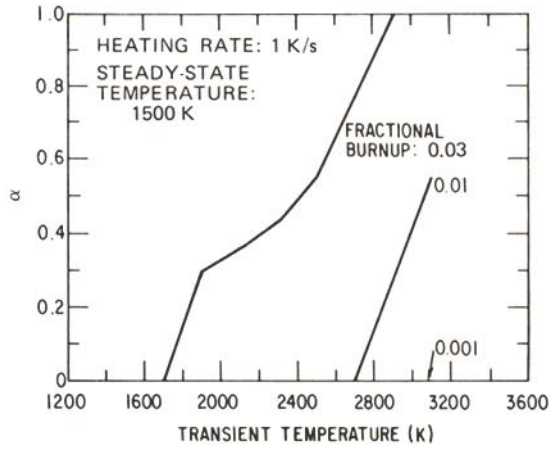

Figure 6.7: A *FASTGRASS* -predicted fraction of total grain boundary area per unit volume which has fractured (α), for fractional burnups of 0.001, 0.01, and 0.03.

Note also that for 0.1 at.% burn-up, the total iodine release is substantially less, and follows qualitatively different kinetics, than the noble gas release, in contrast to the results at higher burn-up values. This is because at this low burn-up value, gas atom diffusion to the grain boundaries is dominating the intragranular fission gas transport during the transient. At the higher values of burn-up, the intragranular fission gas transport during the transient is dominated by the migration of small fission gas bubbles; and because of the assumption that both atomic iodine and CsI migrate within these bubbles, the fractional total-iodine release is qualitatively and quantitatively similar to the noble gas values.

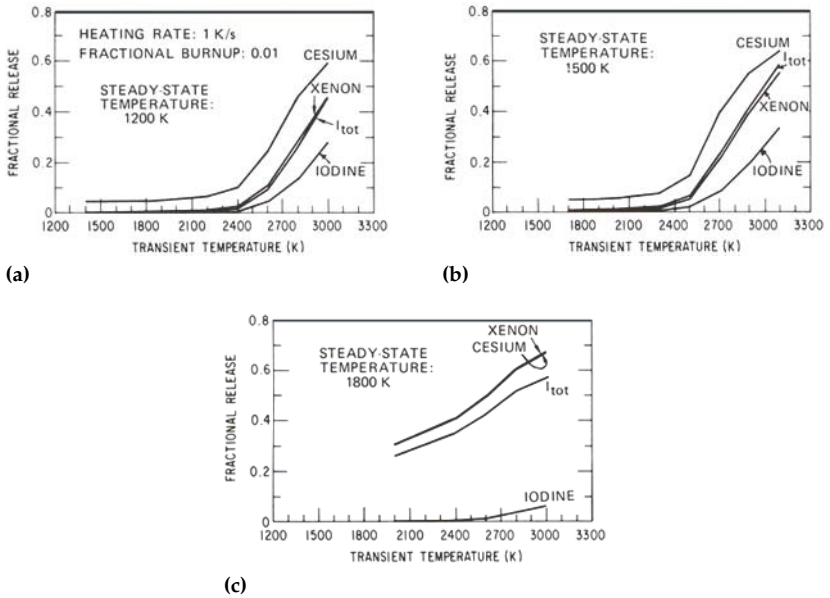

Figure 6.8: A *FASTGRASS* -predicted transient fission-product release for as-irradiated fuel temperatures of (a) 1200, (b) 1500, and (c) 1600 K.

6.3.3 Effect of as-irradiated fuel temperature on fission-product release

Figures 6.8a, 6.8b, and 6.8c show *FASTGRASS* calculated fission product release during a 1.0 K/s heatup in fuel irradiated to 1 at.% burn-up for three values (1200, 1500, and 1800 K) of the average as-irradiated temperature. Figure 6.9 shows the corresponding predictions for fuel microcracking during the three transients. The microcracking results are somewhat similar for the 1200 and 1500 K cases. However, no microcracking is predicted to occur during the transient for the 1800 K case. The reason for this is that at these high fuel temperatures and for a 1.0 K/s heating ramp, the fuel behaves in a relatively ductile fashion and bubble equilibrium behavior dominates over crack-like behavior.

The *FASTGRASS* predictions of transient fission product release for as-irradiated fuel temperatures of 1200 K (Fig. 6.8a) and 1500 K (Fig. 6.8b) are quite similar. The 1800 K case (Fig. 6.8c) shows a much higher steady-state release of xenon, cesium, and total iodine than at 1200 or 1500 K, but similar end-of-transient releases of these fission products. The transient fractional CsI release for the 1800 K case is somewhat higher than for the 1200 or 1500 K case. Also, in the 1800 K case, although the curves for fractional release of xenon and total iodine are qualitatively similar in shape, the fractional release of total iodine is

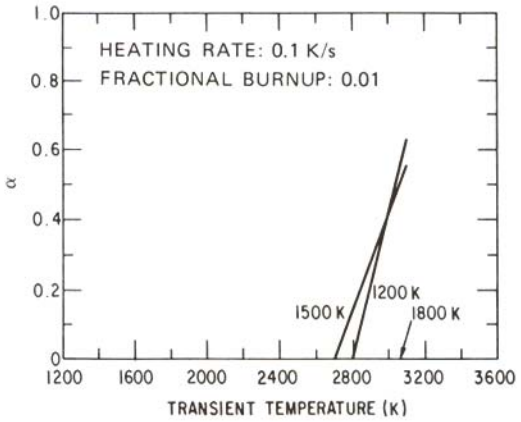

Figure 6.9: A *FASTGRASS* -predicted fraction of total grain boundary area per unit volume which has fractured (α), for as-irradiated fuel temperatures of (a) 1200, (b) 1500, and (c) 1800 K.

somewhat less (by $\sim 10\%$) than that of xenon, in contrast to the results at 1200 or 1500 K. The lower fractional total-iodine release for this case is again due to the fact that during the 1800 K irradiation to 1 at.% burn-up, part of the fission gas migration to the grain boundaries is due to diffusion of single gas atoms. Intragranular diffusion of single gas atoms is also operative at 1200 or 1500 K. In fact, intragranular single-gas-atom diffusion makes a greater contribution to the total fission gas flux to the grain boundaries at the lower temperatures, but the total steady-state releases at these temperatures are, relatively, so low (at 1 at.% burn-up) that the differences between the total-iodine release and the noble gas release are not readily apparent. At higher burnups where the fractional fission product releases are larger (see Fig. 6.6c), the contribution of the intragranular single gas-atom flux to the total fission gas flux to the grain boundaries, and the associated differences between the noble-gas release and the total-iodine release, become more readily visible. The increased transient fractional CsI release for the higher as-irradiated temperature (1800 K) is again due to the associated relatively early release (starting at ~ 2000 K versus ~ 2400 K for the 1200 and 1500 K cases) of the fission products. Release at these relatively lower temperatures, where the CsI contribution to the total available iodine is larger than at the higher fuel temperatures, results in early release of CsI and a resultant increase in the total fractional CsI release during the transient.

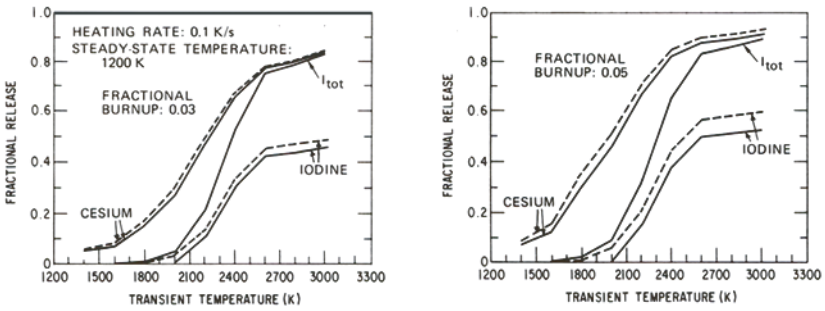

Figure 6.10: A *FASTGRASS* -predicted transient iodine and cesium release, with the effects of Cs_2UO_4 and Cs_2MoO_4 formation included (solid curves) and excluded (dashed curves), for fractional burnups of (a) 0.03 and (b) 0.05.

6.3.4 Effect of cesium chemistry on VFP release

Figures 6.10a and 6.10b show *FASTGRASS* -calculated transient fission product release during a heatup at 0.1 K/s from 1200 K for two values of fuel burn-up (3 and 5 at.%, respectively). The dashed lines in Figs. 6.10a and 6.10b show the results of the calculations when the effects of Cs_2UO_4 and Cs_2MoO_4 formation are not included. In general, these results indicate that the effect of Cs_2UO_4 and Cs_2MoO_4 formation is to increase the fractional release of CsI, and that the magnitude of the effect increases with as-irradiated fuel burn-up. The reason behind the increased fractional CsI release in the presence of Cs_2UO_4 and Cs_2MoO_4 formation can be traced to the reduced release of cesium, which makes more cesium available for CsI formation (i.e., as dictated by chemical equilibrium). This effect would also increase with a decrease in the as-irradiated fuel temperatures (as well as with an increase in fuel burn-up, as shown by a comparison of Figs. 6.10a and 6.10b).

Chapter 7

Fission gas behavior in amorphous nuclear fuels

Until recently, post-irradiation examinations of uranium-silicide dispersion fuel had indicated that the material remained crystalline to high fission doses. A model for irradiation-induced recrystallization of U_3Si_2 (and UO_2) was developed and successfully applied to the interpretation of the experimental observations [38]. Subsequently, ion irradiation and neutron diffraction studies[83] did not confirm the crystalline interpretation, but instead demonstrated that the as-fabricated crystalline material transformed rapidly upon irradiation to an amorphous state and remained thus to extremely high fission doses[84].

In stable intermetallic compounds such as U_3Si_2 (e.g., as compared to compounds such as U_3Si that exhibit unstable swelling behavior), the fission-gas bubble morphology is uniform with no clear evidence of bubble coalescence or interlinkage. The small fission-gas bubbles remain stable to high burn-up. Even at 63% burn-up of a 93% enriched mini-plate, the fission-gas bubbles retain a uniform morphology[38].

Two very important observations were made that still underpin current understanding of the swelling behavior[38]. Firstly, the initial rate of swelling is relatively low, and then accelerates markedly. This transition referred to as the 'knee point' marks the fission density at which the fission-gas bubbles reach a sufficient size to influence swelling behavior in addition to solid fission products. Prior to the knee, a small fraction of the fission gas is retained in solution while the rest is believed to be stored in nanometer-size bubbles which are below the limit of resolution of the SEM. Secondly, the fission rate appeared to influence the fission density at which the fuel swelling began to accelerate. At a higher fission rate the knee point is shifted to a higher fission density.

The model consists of a set of rate equations that are described in the next section. Sections 7.2 and 7.3 contain an analysis of bubble growth at and beyond the knee. Section 7.4 consists of a comparison of the theory with data for an U_3Si_2 intermetallic compound.

7.1 Model description

In crystals, bubbles cannot form without vacancies. Vacancy migration leads to bubble growth. This basic mechanism still holds for amorphous materials. In amorphous materials, fission damage does not produce vacancies but instead generates free space commonly called free volume. Fission gas generated during irradiation diffuses by a free volume migration mechanism and leads to the nucleation and growth of fission gas bubbles. The diffusivity of the gas in the amorphous material can be described by a Nernst-Einstein relationship [4], i.e. the diffusivity is inversely proportional to the viscosity η,

$$D_g = \frac{kT}{6\pi r_g \eta} \quad , \tag{7.1.1}$$

where T is the absolute temperature, k is Boltzmann's constant, and r_g is the radius of a diffusing gas-atom. A drastic decrease in the viscosity of a simple glass has been observed to occur under irradiation by heavy ions[85, 86]. In analogy with mechanical deformation, the viscosity is assumed to have a similar dependence on fission rate as it has on mechanically induced strain rate, i.e. the viscosity is inversely proportional to the fission rate $\dot{f}$,

$$\eta = \eta_0 / \dot{f} \quad , \tag{7.1.2}$$

where in general η_0 is a function of temperature, i.e. $\eta_0 = e^{-\theta/T}$ Eq. (7.1.2) is supported by observations of plastic flow of glasses under bombardment by heavy ions[86]. Combining Eqs. (7.1.1) and (7.1.2) results in a gas-atom diffusivity that is proportional to the fission rate, i.e.

$$D_g = \frac{kT\dot{f}}{6\pi r_g \eta_0} = D_0 \dot{f} \quad , \tag{7.1.3}$$

where $D_0 = D_0(T) = kT/6\pi r_g \eta_0$. Free volume migration can also result in the movement of small bubbles by a volume diffusion mechanism. In this case the gas-bubble diffusivity is given by

$$D_b = \frac{3\Omega D_g}{4\pi r_b^3} \quad , \tag{7.1.4}$$

where Ω is the atomic volume and r_b is the bubble radius.

The bubble nucleation rate is proportional to the interaction rate between fission gas atoms. In general, when gas atoms come together at a free volume site in the amorphous material and form a small cluster, neighboring host atoms produce interactions with the cluster that can lead to its dissolution. For example, consider the mechanism of plastic flow in metallic glasses in which strain is produced by the local rearrangement of atoms nucleated under the applied stress with the assistance of thermal fluctuations in regions around free volume sites. Argon named this strain generating mechanism a local shear transformation[87]. During these local shear transformations the surrounding atoms have to be pushed apart at some point along the activation path, producing an activation dilatation. If the small gas atom clusters are nearby to the dilatation, nucleation of a gas bubble can occur. Thus, the bubble nucleation rate depends on the volume fraction of shear bands in the material. This condition is analogous to the requirement in crystalline material that in order to become a stable bubble, the gas atom clusters must be in close proximity to vacancies and/or vacancy clusters[1]. Bubble nucleation is not considered to occur outside of the shear bands due to insufficient free volume within the U_3Si_2 compound (e.g., U_3Si_2 contracts upon amorphization: see Ref. [83]).

Consider a region of the material initially shearing at a rate $\dot{\gamma}_0$ imposed by some external agency that maintains the rate constant. The separation of flow in this region into shear bands covering a fraction f_s of the volume and the remaining matrix covering a fraction $(1 - f_s)$ is described by the equation

$$f_s \dot{\gamma}_b + (1 - f_s)\, \dot{\gamma}_m = \dot{\gamma}_0 \quad . \tag{7.1.5}$$

In general, $\dot{\gamma}_m \ll \dot{\gamma}_0 \ll \dot{\gamma}_b$ so that solving Eq. (7.1.5) for f_s yields

$$f_s \approx \frac{1}{\dot{\gamma}_b} \left(\dot{\gamma}_0 - \dot{\gamma}_m\right) \approx \frac{\alpha}{\dot{f}} \quad . \tag{7.1.6}$$

The shear strain rate γ_b in Eq. (7.1.6) due to mechanical deformation has been assumed to be proportional to the fission rate, $\dot{f}$, where α is the constant of proportionality. This last relationship underlies the assumption that there is a

direct correspondence between mechanically induced and fission-induced processes in the same material (i.e., in one the stresses are induced by mechanical deformation and in the other by fission events).

Eq. (7.1.2) gives the viscosity of an amorphous material undergoing shear deformation due to fission spikes. We are concerned here with the behavior of bubble nucleation as a function of fission rate, or analogously, viscosity. As the fission rate increases, the viscosity decreases and, thus, the shear strain rate within the shear bands increases. Eq. (7.1.6) states that for constant $\dot{\gamma}_0$, an increase in $\dot{\gamma}_b$ results in a smaller volume fraction of shear bands in the material.

When gas atoms come together within a free volume site, a shear force acting to separate the atoms is generated by the plastic flow of material around the cluster. These small gas-atom clusters must grow to a critical size (e.g., on the order of 10 or more gas atoms) in order to become a stable, equilibrium gas bubble. In analogy with the theory of viscous adhesion[88], it is assumed that the probability that the gas-atom cluster stays intact is proportional to the viscosity. Thus, the bubble nucleation rate is proportional to the viscosity as well as to f_s, i.e.

$$\frac{\mathrm{d}c_b(t)}{\mathrm{d}t} \approx f_s \eta \quad , \tag{7.1.7}$$

where c_b is the gas-bubble concentration.

As the irradiation continues, the bubble-size distribution coarsens by bubble growth due to the accumulation of fission gas atoms and bubble coalescence. In addition, bubbles can be totally destroyed (whole bubble destruction for bubbles below a critical size) by collisions with fission fragments, or have their growth rate reduced due to the shrinkage effects of irradiation-induced resolution. With the exception of the bubble nucleation mechanism given by Eqs. (7.1.2) and (7.1.7), the equations describing the time evolution of the fission gas atoms and bubbles in the amorphous compound are analogous to the rate equations describing bubble behavior in a crystalline material[26] and are given by

$$\begin{aligned}\frac{\mathrm{d}c_g(t)}{\mathrm{d}t} =& \beta\dot{f} - \frac{4\pi f_n D_g c_g(t) c_g(t)}{\dot{f}^2} \\ & - 4\pi r_b(t) D_g c_b(t) c_g(t) - 2b m_b(t) c_b(t) \quad ,\end{aligned} \tag{7.1.8}$$

$$\frac{\mathrm{d}c_b(t)}{\mathrm{d}t} = \frac{4\pi f_n D_g c_g(t) c_g(t)}{m_b(t)\dot{f}^2} - b c_b(t) - 16\pi r_b(t) D_b(t) c_b(t) c_b(t) \quad , \tag{7.1.9}$$

$$\frac{\mathrm{d}m_b}{\mathrm{d}t} = 4\pi r_b(t) D_g c_b(t) c_g(t) - b m_b(t) + 16\pi r_b(t) D_b(t) m_b(t) c_b(t) \quad , \tag{7.1.10}$$

where c_g and c_b are the concentration of gas atoms and bubbles, respectively, m_b is the number of gas atoms in a bubble of radius r_b, b is the gas-atom re-solution rate, and $f_n = 4\alpha\eta_0 r_g$.

The quantities c_g, c_b, m_b in Eqs. (7.1.8)-(7.1.10) represent average values. For example, $c_b(t)$ bubbles each containing $m_b(t)$ gas atoms represents the average value of the bubble-size distribution at time t. In general, r_b is related to m_b through the gas law and the capillarity relation. Using the van der Waals gas law,

$$\frac{2\gamma}{r_b}\left(\frac{4}{3}\pi r_b^3 - b_v m_b\right) = m_b k T \quad , \tag{7.1.11}$$

where γ is the surface tension, b_v, is the van der Waals constant, k is Boltzmann's constant, and T is the absolute temperature. The four terms on the RHS of Eq. (7.1.8) respectively represent the generation of gas atoms due to fission (β is the number of gas atoms produced per fission), the loss of gas atoms due to bubble nucleation, the loss of gas atoms due to diffusion to existing bubbles, and the gain of gas atoms due to irradiation-induced gas-atom re-solution from bubbles. The three terms on the RHS of Eq. (7.1.9) respectively represent the gain of bubbles due to bubble nucleation, the loss of bubbles due to whole bubble destruction by interaction with fission fragments, and the loss of bubbles due to bubble coalescence. The three terms on the RHS of Eq. (7.1.10) respectively represent the gain of gas atoms per bubble due to gas atom diffusion to bubbles, the loss of gas atoms per bubble due to irradiation-induced re-solution, and the gain of gas atoms per bubble due to bubble coalescence. In general, the gas-atom re-solution rate is proportional to the fission rate, i.e.

$$b = b_0 \dot{f} \quad . \tag{7.1.12}$$

Eqs. (7.1.8)-(7.1.11) can be solved numerically to obtain the quantities $c_g(t)$, $c_b(t)$, $m_b(t)$, and $r_b(t)$.

Due to the strong effect of irradiation-induced gas-atom re-solution, in the absence of geometrical contact the bubbles stay in the nanometer size range. The density of bubbles increases rapidly early in the irradiation. Subsequently, at longer times the increase in bubble concentration occurs at a much-reduced rate at the relatively low irradiation temperatures under consideration ($T/T_m < 0.5$).

Eventually, the bubble distribution reaches a point where larger bubbles from the tail of the distribution begin to contact the more numerous smaller bubbles from the peak region. This condition defines the knee in the swelling curve. That these nanometer-sized bubbles exist and have an evolving size-distribution that is consistent with the above picture is clearly illustrated in Fig. 1 of Ref. [89] that shows a TEM photograph of bubble formation and growth in glasses. The validity of an evolving log normal bubble-size distribution in an irradiated amorphous material that coarsens by bubbles growing into each other is further strengthened by the observation of nanometer sized helium bubbles that form, grow, and coalesce during low-temperature helium implantation in an amorphous alloy[90].

7.2 Bubble growth at the knee

At the knee the larger bubbles within the tail of the bubble-size distribution begin to contact smaller bubbles and grow as a result of the coalescence. This growth facilitates more contact and the process continues until the density of smaller bubbles is reduced below the value required for contact. In order to simplify a quantitative description of this process, the bubble-size distribution is separated into two regimes characterized by average radii and number densities: the small bubble bell-shaped region, and the large bubble tail region. The peak of the bubble-size distribution given by

$$n(r) = \frac{2b_v\chi\beta\dot{f}t}{\pi^{3/2}}\kappa^{5/2}\exp\left[-\kappa r^2\right] \quad , \tag{7.2.1}$$

where $\kappa = \kappa(t) = b_0/2\beta b_v D_g t$ with $r_0 = 0$ (see [91], §2.3.1) occurs at a bubble radius

$$r_{\text{peak}} = \sqrt{\frac{1}{2\kappa}} \quad . \tag{7.2.2}$$

The bubble radius that defines the interface between the two regions r_I (see Fig. 7.2) is taken to be

$$r_I = 3.33 r_{\text{peak}} \quad . \tag{7.2.3}$$

The tail of the bubble-size distribution is centered at a bubble radius

$$r_{\text{tail}} = 5 r_{\text{peak}} \quad . \tag{7.2.4}$$

The average bubble densities characterizing these two regions are obtained by integrating Eq. (7.2.1) over each regime to obtain, respectively, the total quantity of gas in bubbles and choosing number densities of bubbles of sizes r_{peak} and r_{tail}, respectively, that are consistent with the conservation of gas atoms, i.e.

$$N_1 = \frac{1}{m\left(r_{\text{peak}}\right)} \int_0^{r_I} m(r) n(r) \mathrm{d}r = 3.6 \chi b_v \beta \dot{f} t \left(\frac{\kappa}{\pi}\right)^{3/2} \quad , \tag{7.2.5}$$

$$N_2 = \frac{1}{m\left(r_{\text{tail}}\right)} \int_{r_I}^{\infty} m(r) n(r) \mathrm{d}r = 2 \times 10^{-3} \chi b_v \beta \dot{f} t \left(\frac{\kappa}{\pi}\right)^{3/2} \quad , \tag{7.2.6}$$

where χ is the fraction of gas generated during the time required to reach the knee (i.e. $t \rightarrow t_{\text{knee}}$), and the ideal gas law (i.e., neglect second term within the parenthesis in Eq. (7.1.11)) has been used to express $m(r)$ and $m(r_{\text{tail}})$ in Eq. (7.2.6) in order to simplify the integration.

Fig. 7.1 shows $n(r)$ from Eq. (7.2.1) as well as the position of r_{peak}, r_I, and r_{tail} calculated at the onset of the knee for a fission rate of 2.5×10^{20} $\text{m}^{-3} \cdot \text{s}^{-l}$ and using the parameters in Table 7.1. The insert in Fig. 7.1 is a blowup of the region containing r_I, and r_{tail} showing details of their positioning. Fig. 7.2 shows the calculated (see [91], §2.3.2 Eq. (39)) average number of intersections, $\bar{I}(r)$, of a bubble with radius r_I with other bubbles in distribution $n(r)$ shown in Fig. 7.1. The position of $\bar{I}(r_I) = 1$ is shown and corresponds to the onset of the knee and to the value of $R_{ds} = 0.42$ (obtained from the solution of Eq. (40), Ref. [91], §2.3.2).

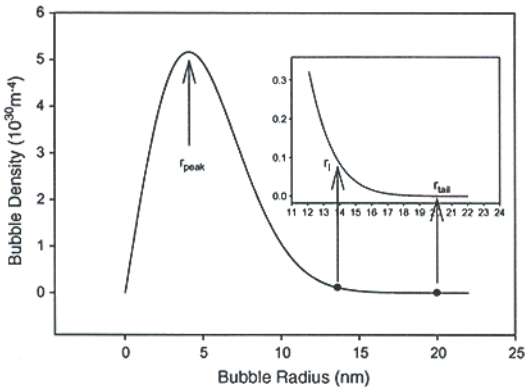

Figure 7.1: Calculation of bubble-size distribution showing position of r_{peak}, r_I, and r_{tail}. The inset shows a blowup of the regions containing r_I and r_{tail}.

The coarsening of the larger bubbles in region 2 at the expense of the smaller bubbles in region 1 is modeled by an increase in the radius R of a fixed density of N_2 bubbles with a commensurate decrease in the density N of bubbles having fixed radius r_{peak}. If the population of N_1 bubbles decreases by ΔN_1, due to coalescence with the population of N_2 bubbles, the number of gas atoms in N_2 bubbles increases from $m(r_{\text{peak}})$ to $m(\text{obs})$ where

$$m(\text{obs}) = m(r_{\text{tail}}) + m(r_{\text{peak}})\Delta N/N_2 \quad . \tag{7.2.7}$$

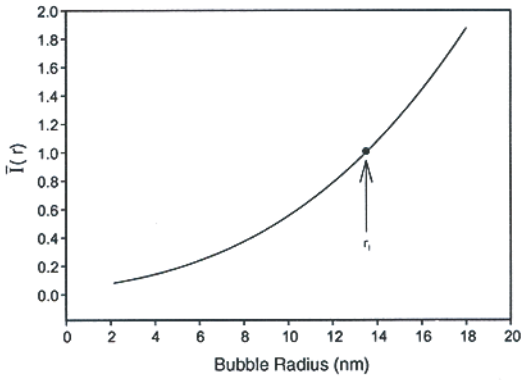

Figure 7.2: Calculation of average number of intersections of bubble with radius r_I with other bubbles in distribution $n(r)$ shown in Fig. 7.1. The position of $\bar{I}(r_I) = 1$ is shown and corresponds to the onset of the knee and to the value of $R_{ds} = 0.42$.

The bubble density functions $n(r)$, (r_{peak}, N_1), and (r_{tail}, N_2) represent spatially smeared quantities: the bubble density is locally high in some regions and locally low in others. Coalescence at the knee will continue until all of the locally high bubble density regions are consumed with each local region being replaced by one bubble containing $m(\text{obs})$ gas atoms. At this point the bubble-size distribution (e.g., Eq. (7.2.1)) will represent the remaining spatial regions. It is assumed here that the characteristics of the bubble-size distribution are such that when the locally high-density regions are removed from the calculation, the average number of intersections a representative bubble at the interface between the two regions has with other bubbles (see Eq. (38), Ref. [91], §2.3.2,) is equal to $^1/_2$. This condition constrains the larger bubbles in the tail to have an average number of intersections with other bubbles < 1, and the contact-coalescence event is terminated. It follows from Eq. (38) in [91], Sec. §2.3.2, that, in terms of the average quantities in regions 1 and 2 this condition is satisfied by

$$\Delta N_1 = \frac{N_1}{2} \quad . \tag{7.2.8}$$

7.3 Bubble growth after the knee

Eqs. (7.2.6)-(7.2.8) can be solved to obtain the radius of the large bubble distribution after the coalescence event at the knee reaches completion, i.e.

$$R = \frac{1}{2}\left[\frac{50}{\kappa} + \frac{196\pi kT}{\gamma b_v \kappa^{3/2}}\right]^{1/2} \quad . \tag{7.3.1}$$

Immediately after knee formation the gas bubble swelling is given by

$$\left(\frac{\Delta V}{V_0}\right)^{t=t_{\text{knee}}} = \frac{4\pi}{3}\left(r_{\text{peak}}^3 \frac{N_1}{2} + R^3 N_2\right) \quad . \tag{7.3.2}$$

Subsequent to the formation of the knee, the above process repeats, but now the evolution of the nanometer size bubble distribution is overlaid on the pre-existing larger bubble population. Both bubble distributions coarsen due to the accumulation of fission gas as the irradiation proceeds. Eventually, a secondary knee point is achieved and a second population of bubbles in the tenths of a micron size range is generated. Thus, as the population of larger bubbles

formed at the primary knee has coarsened, a bi-modal population of bubbles is observed subsequent to the secondary knee point.

The spatial distribution of larger bubbles formed at the knee by coalescence of clusters of smaller bubbles growing into each other mirrors the spatial distribution of the bubble distribution prior to the knee, but on a larger length scale. Thus, as the irradiation proceeds, larger bubbles situated in relatively close proximity will grow into each other and coalesce. The rate of swelling increases at the knee due to the large bubble coarsening process. The large bubble coarsening process is described by

$$N(t) = N_2 \exp\left[-\phi\left(t - t_{\text{knee}}\right)\right] \quad , \tag{7.3.3}$$

where the value of the rate constant ϕ is estimated from the data (see Table 7.1).

The interpretation provided for Fig. 7.4 (discussed in §7.4, below) that the fraction of generated gas in bubbles remains relatively constant after knee formation supports the assumption that the generated gas is depleted initially by the evolving nanometer size bubble distribution with the remainder available for absorption into the existing, larger bubble population. Thus, for times $t > t_{\text{knee}}$ the growth of the larger bubbles can be expressed by

$$\frac{\mathrm{d}m(t)}{\mathrm{d}t} = \frac{\left[1 - \chi(t)\right]\beta\dot{f}}{N(t)} - \frac{m(t)}{N(t)}\frac{\mathrm{d}N(t)}{\mathrm{d}t} \quad , \tag{7.3.4}$$

where $\chi(t) \leq \chi(t_{\text{knee}})$.

Eqs. (7.3.3) and (7.3.4) can be solved to obtain $m(t)$. Thus, the fuel swelling after knee formation is approximately given by

$$\begin{aligned}\left(\frac{\Delta V}{V_0}\right)^{t>t_x} =& \beta_s \dot{f} t + \frac{2\pi r_{\text{peak}}^3 N_1}{3}\left[1 + \frac{\chi(t)}{\chi(t_{\text{knee}})}\right] \\ &+ \left[\frac{3kT}{8\pi\gamma}\left(m(\text{obs}) + \frac{\beta\dot{f}te^{\phi t}\left(1 - \chi(t)/2\right)}{N_2}\right)\right]^{1/2} \quad ,\end{aligned} \tag{7.3.5}$$

where β_s is the fractional swelling due to solid fission products per unit fission density.

Parameter	Value	Reference
β	0.25	[1]
b_0	$2 \times 10^{-23}\,\mathrm{m}^{-3}$	[92]
η_0	$2 \times 10^{7}\,\dot{f}_0$ poise	[91]
r_g	0.216 nm	[93]
γ	$0.7\,\mathrm{Jm}^{-2}$	[3]
$\dot{f}_0$	$1.25 \times 10^{20}\,\mathrm{m}^{-3}\,\mathrm{s}^{-1}$	[91]
α	$2 \times 10^{-10}\,\dot{f}_0$	[91]
β_s	$1.75 \times 10^{-29}\,\mathrm{m}^{3}$	[91]
ϕ	$8 \times 10^{-8}\,\mathrm{s}^{-1}$	[91]

Table 7.1: Values of key parameters used in calculation for U_3Si_2

7.4 Comparison with data

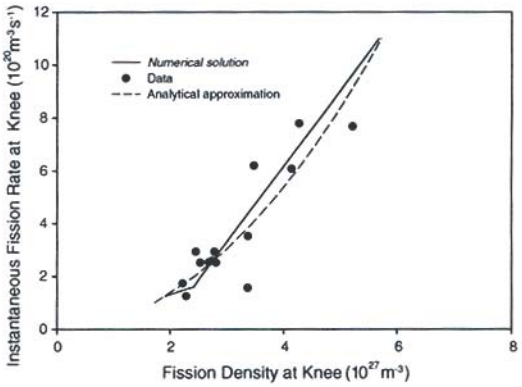

Figure 7.3: Calculation of the fission density at which the knee occurs compared with data.

Fig. 7.3 shows the fission density at which the knee occurs obtained from a numerical solution of Eqs. (7.1.8)-(7.1.11) using Mathematica (http://www.wolfram.com) and the value of $R_{ds} = 0.42$ (derived from the solution of Eq. (40), Ref. [91], §2.3.2) as a function of fission rate compared with the experimentally estimated quantities[93]. The uncertainty in the experimental values is estimated to be $\pm 20\%$. The results of Fig. 7.3 demonstrate that the theory is in agreement with the trends of the data. The fission density at which the knee occurs, given by the analytical approximation found in Ref [91], §2.2, is proportional to the

	Bubble diameter (μm)	Bubble density (10^{19} m^{-3})
Data	0.1	7.5
	0.15	0.85
Theory	0.116	7

Table 7.2: Calculated average bubble diameter and density compared with data for mini-plate A224[93].

square root of the fission rate. The analytical solution is also shown in Fig. 7.3. The approximation is dependent on the validity of the approximate solution to Eq. (7.1.8). Fig. 7.4 shows a comparison between c_g calculated from a numerical solution to Eqs. (7.1.8)-(7.1.11) and an approximation of c_g as a function of irradiation time for three values of the fission rate. Also shown in Fig. 7.4 is the calculated position of the knee. It is clear from Fig. 7.4 that the approximate solution approaches the numerical solution at irradiation times near the time required to achieve the knee. It is also interesting to note from Fig. 7.4 that the knee shifts to shorter times (and, as shown in Fig. 7.3, higher fission densities) as the fission rate is increased. Examination of the calculated quantities in Fig. 7.4 supports the validity of the approximation equations derived. Comparison of the calculated quantities and the data shown in Fig. 7.3 demonstrates that the theory follows the trend of the observation.

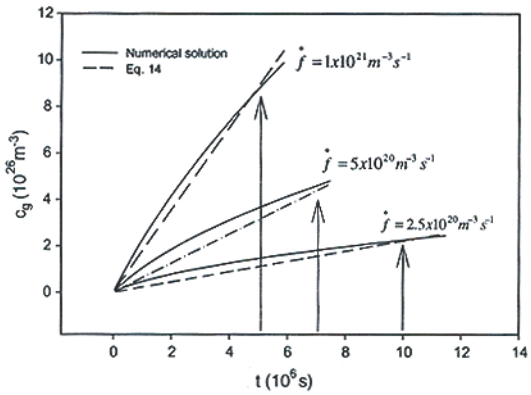

Figure 7.4: Comparison between c_g calculated from a numerical solution to Eqs. (7.1.8)-(7.1.11) and an approximation of c_g as a function of irradiation time for three values of the fission rate. Also shown is the calculated position of the knee (arrows).

Fig. 7.5 shows the calculated fraction of generated gas in SEM-observable bubbles at the knee (i.e., $m(\text{obs}) * N_2/\beta\dot{f}t$) made using Eqs. (7.2.2), (7.2.4), (7.2.6),

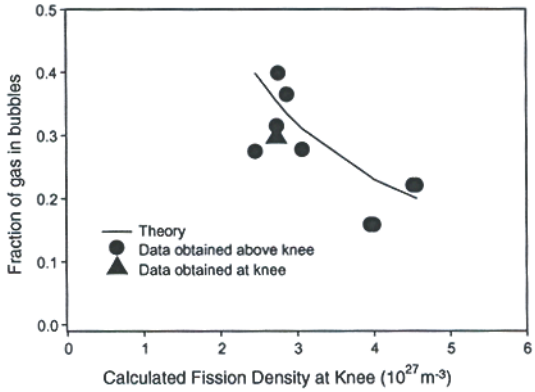

Figure 7.5: Calculation of the fraction of generated gas in bubbles at the knee compared with data taken at various fission densities.

(7.2.7), and an approximating function (specifically, Eq. (22), Ref. [91], §2.2) subsequent to the solution of Eqs. (7.1.8)-(7.1.11) compared with data taken at various fission densities[93]. The general agreement between the calculated and measured quantities supports the position that the gas in bubbles at times subsequent to the formation of the knee is relatively constant. This situation is possible due to the presence of the large bubble population formed at the knee which accumulates the generated gas concurrently with the evolution of the nanometer sized bubble population that inhabits the spaces in between the larger bubbles.

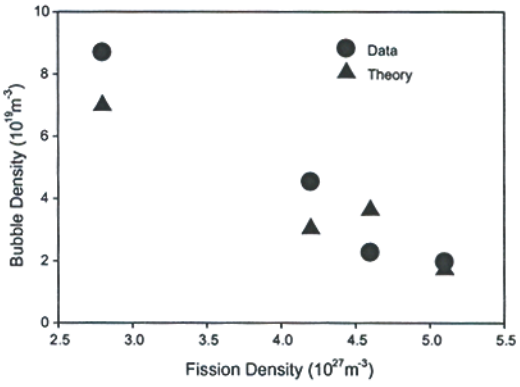

Figure 7.6: Bubble densities calculated using Eq. (7.3.3) compared with data.

Table 7.2 shows the calculated average bubble diameter (Eqs. (7.1.11) and (7.2.7)) and density (Eq. (7.2.6)) at the knee compared with data for mini-plate A224[93]. The calculated quantities are in agreement with the measured val-

ues. Fig. 7.6 shows the calculated bubble density (Eq. (7.3.3)) as a function of fission density compared with data. The points at the lowest fission density are at the knee, whereas the other points are beyond the knee. It is important to note that aside from the time dependence inherent in Eq. (7.3.3), the density of bubbles at the knee N_2 is dependent on the fission rate (N_2 increases as the fission rate decreases, e.g. see Eq. (7.2.6)). The calculated results plotted in Fig. 7.6 show that in general, the bubble density decreases with continued irradiation (i.e., due to bubble coarsening by bubbles growing into each other) and follow the trend of the data.

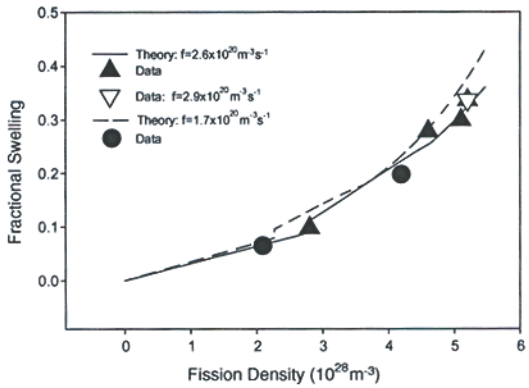

Figure 7.7: Calculated fuel particle swelling using Eqs. (7.3.2) and e:amrfgbblsllaknee for several values of the fission rate compared with data.

Fig. 7.7 shows the calculated fuel particle swelling using Eqs. (7.3.2) and (7.3.5) for several values of the fission rate compared with data[93]. As is shown in Fig. 7.7, the knee in the swelling curve is defined by the increased slope due to the formation of the SEM-visible bubbles at the knee. The calculations shown in Fig. 7.7 indicate that higher fission rates result in decreased values of fuel swelling. The calculated swelling follows the trends of the data.

Chapter 8

Next steps: application and development of analytical modeling

First principle atomistic modeling of radiation damage was actively pursued in the 60's and early 70's. Limited computer power at that time did not allow development of comprehensive models. It is fashionable these days for scientists to use "first principle" terminology, but the problem remains complex with solutions dependent on many assumptions (e.g. nature of inter-atomic potentials), and simulation times on the order of 10^{-9} s. Thus, comparison to experimental results (e.g. atomic diffusion) is very limited. Kinetic mechanistic modeling depends on various key materials properties that are currently experimentally unavailable for the proposed candidate advanced fuels. First principle modeling (e.g. molecular dynamics combined with kinetic Monte Carlo methods) can be utilized to calculate/estimate these critical property values. Keeping in mind a proper balance between the coupling of atomistic and mechanistic modeling (see §B), atomistic first principle modeling can be combined with kinetic modeling in order to provide the kinetic modeling with required materials properties values, and to make a direct connection to observation.

The opportunity for pursuing the above has never been greater. The capability and availability of high performance computing (HPC) continue to expand in the field. HPC modeling of RERTR fuels would tie together the phenomenological results that have been seen in fuels development and irradiation performance with the experience gained around the complex in HPC models development. The result would provide a true science-based understanding of

RERTR fuel evolution during irradiation. RERTR fuels provide the ideal foundation to expand the models as there is a vast amount of data that has been collected on RERTR fuel performance. The RERTR fuel base is viable jumping-off point for the application of the theory to advanced fuels for power reactors. More importantly, the extensive validation opportunities within the RERTR research program will enable the successful extrapolation of the models to describe advanced fuel behavior. Design using such models can help avoid some of the testing costs by allowing *a priori* decisions to target the most important test conditions to validate and verify the predictions. Additionally, the research could be used to help develop future fuels for HEU to LEU conversion (i.e., for the last few reactors) or for other materials handling/disposition issues.

First principle understanding of phenomena such a bubble nucleation, coalescence and diffusion is critical. The understanding of fuel evolution during irradiation and the development of a predictive capability for gas-driven swelling and fission-gas release will improve the capability to extrapolate from known database of results into new regimes and afford a better understanding of the margin of uncertainty, which may enable additional options. The milestones reached in this effort are ultimately aimed at strengthening the foundation for design of fuel systems necessary for next generation research reactors.

8.1 Development areas

To further the present understanding of the effects of fission gas and irradiation produced defects in advanced fuel microstructures, current research would seek to theoretically explore the synergistic relationship between the evolution of the fuel microstructure and fission-gas response. This approach, pursued in conjunction with analytical and first principle modeling of key materials properties that are currently experimentally unavailable, is required for the calculation of advanced fuel behavior. Experience in analyzing the coupled kinetics of inert gas behavior and defect clustering and the effects of modeling the fundamental nature of defect clusters in irradiated materials, mechanistic modeling of materials properties, theoretical modeling of irradiation-induced microstructural changes, and analyzing the behavior of a wide class of nuclear fuels under both steady state and off-normal conditions is necessary to fully exploit this theoretical approach.

As a first year plan, an attainable objective would be to identify the key atomistic and materials properties required by the kinetic mechanistic models, collect the physics models currently available to describe the fuel evolution, the bubble morphology, the cladding properties, etc., and build a thermo-mechanical model of the fuel evolution. The following milestones are in-line with current thinking:

1. Development of a balanced atomistic/kinetic-mechanistic approach to the uranium-molybdenum fuels that incorporates cascade evolution; various defects, such as fission gas bubbles, vacancies and interstitials, based on electronic and atomistic models, including accelerated MD methods; fission-gas bubble formation and evolution and its effect on thermo-mechanical properties; mesoscale simulation of irradiation effects.
2. Development of a thermo-mechanical model, which would incorporate the above.
3. Validation of the models by comparing to existing experimental data.

Chemical-rate-theory modeling can be employed in order to calculate the formation, interaction, and evolution of Xe, irradiation-produced defects, defect complexes such as interstitial and vacancy loops, forest dislocations, and impurities as a function of materials properties and irradiation conditions. MD and KMC techniques are suitable candidates to estimate the required atomistic and materials properties. In addition, the calculations derived can be used to assess the nature of the effect of helium on these irradiation-produced obstacles to dislocation motion. General principles should be extracted from models to allow enhancement of the mitigation of fuel swelling, perform calculations to show this, and define experiments to test theory.

8.1.1 Timeline

Outlined is a three year plan for the development of the key strategies mentioned above.

Year 1:

- General formulation of first principle approaches for calculating key materials properties required by kinetic mechanistic models.
- Identification of key materials and atomistic properties required for fuel modeling studies.
- Initiate modeling of the effects of Xe on irradiation-produced precipitation

Year 2:

- Initiate incorporation of mechanistic model materials and atomistic property requirements into first principle codes.
- Initiate mechanistic treatment of dislocation interactions with Xe-precipitate complexes based on existing experimental results and models devised in this research

- Initiate modeling of fuel swelling

Year 3:

- Incorporate models for Xe-precipitate complexes into first principle formulation
- Develop combined atomistic/kinetic-mechanistic models for swelling in irradiated fuels
- Extract general principles from models to allow enhancement of the mitigation of fuel swelling; perform calculations to show this and define experiments to test theory

8.2 Final thoughts

The body of work developed by Jeffrey Rest and collected in this publication represents an important contribution of the physical understanding of nuclear fuel behavior within nuclear reactors. A physical, analytical description of nuclear fuel behavior, although highly useful, has become an uncommon practice in the field. Despite the high level of productivity that followed the success of the first controlled fission reaction in 1942, research dwindled down to a trickle since the developments of Three Mile Island.

Today, the great majority of fuel performance and predictive codes are commissioned for reactor- or task-specific applications. The models employed in these applications are consistently empirical, as it is difficult to justify the economic cost of modeling the physical behavior underlying the models. Empirical models are viable in the narrow range of conditions in which they were developed and cannot be used to predict observed behavior outside of their range of applicability. Thanks to these intrinsic limitations, however, these models are relatively straight-forward and generally provide accurate results.

The reason for the prevalence of empirical computer models is essentially twofold. The first reason, as suggested above, has to do with the development cost of generating task or category-specific statistical models. An empirical model reflects the observed behavior of the subject and strives to discover the trends and patterns that describe this observed behavior. Causative mechanisms and processes are not generally considered. Secondly, there's a significant amount of inertia to produce analytical models due to the many obstacles that make progress difficult in that field. The environment of an irradiated fuel element is a highly active and complex system. Accurate modeling entails the coupling of many related processes in changing fuel conditions. The endeavor is further complicated by the absence of important material properties, such as accurate

values for gas-atom, vacancy and interstitial diffusion coefficients; measures of thermal conductivity; and bubble nucleation rates, etc. Moreover, it is often difficult to extract precise information of what actually occurs within the fuel under irradiation. Since it is impossible to take any measurements while the fuel is being irradiated, all observations and measurements of nuclear fuels are performed out-of-pile. Therefore, these observations are, by necessity, retrospective, and it is not always possible to determine the sequence of events that caused the observed characteristics of the fuel.

Understandably, empirical models are efficient and tend to yield acceptable results within their range of applicability. However, because these performance codes are calibrated to the narrow application they were designed for, changes in operating conditions may invalidate the model. Furthermore, since the essential parameters change among different fuels and reactors, using an empirical model for a different application may be impractical, if not unfeasible.

Analytical models are characterized by their flexibility and portability. The aim of these models is to approximate the behavior of a fuel under one or a variety of different conditions. Because the focus is on fuel *behavior*, it is not only possible to describe observed phenomenon from these models, but also to predict potential issues that have not yet occurred. This is possible, even under varying conditions. Most importantly, because many fuels share similar composition and material characteristics, analytical models can be translated with minimal modifications to model a range of different fuels.

The major impediment to accurate portability of analytical models is the relative shortage of fuel properties values. The property values, like some of the examples given above, form the qualitative differences in nuclear fuels and often drive the dominating mechanisms that are manifested. As the preceding section suggests, much can be learned from first principle computer simulations and there seems to be great promise in the development of atomistic and molecular models. These models may be able to provide accurate gas-atom and vacancy and interstitial diffusion coefficients, bubble nucleation rates, values for the thermal conductivity of the fuel, as well as many other properties that are presently unavailable.

First principle modeling can provide the observations that are impossible to obtain from in-pile experiments. This resource can be useful as the development of improved experimental methods have yielded results that motivate further theoretical investigation. For example, it has been observed that bubble nucleation mechanisms on the grain boundary do not appear to proceed according to established theory and that other processes may be involved. Similarly, many questions still abound regarding the exact mechanism for gas-atom diffusion within the fuel. Even in the relatively short run time of the proposed atomistic models, processes such as the two just mentioned may be readily observable.

The efficiencies of analytical, physically-based models provide compelling reasons to expand this kind of research. Mechanistic models that provide accurate representations of fuel behavior are valuable tools that can be used to assess and evaluate a range of fuels in a variety of operating environments.

8.2.1 Extended effort

The authors of this work believe that it is important to note that this compilation is not exhaustive. While the Rest Models offer insight into many of the behaviors influence by gaseous fission products, a full description of fuel behavior would require the investigation of all available, workable mechanistic models. A proposed future work would, in a manner similar to what has been done in this report, compile and organize relevant theoretical models from around the world.

Appendix A

The mobility of overpressurized fission gas bubbles

The physical basis behind this approach is as follows: During equilibrium conditions, the bubbles may be faceted, and the rate of motion of a faceted bubble is determined by the frequency of nucleation of steps instead of the time required for atoms to move from a step on one side of a bubble to a step on the other side[94]. (That is, the atom attachment and detachment rates are slower than predicted by surface diffusion.) However, if the atom attachment and detachment rates increase during transient conditions, higher bubble diffusivities will result.

Since plastic deformation of the UO_2 due to an overpressurized bubble is expected to result in a high density of dislocations around the bubble surface, the diffusivity of such a bubble (if otherwise restricted in its mobility, as the steady-state model assumes) would be expected to increase rapidly. In effect, bubble diffusion would depend more on the time required for atoms to move from a step on one side of a bubble to a step on the other (i.e., surface diffusion) than on the frequency of nucleation of steps.

A.1 A model for the diffusion of overpressurized fission gas bubbles

In an attempt to quantify the ideas presented above, consider the excess internal gas pressure in a bubble of radius ri that is given by

$$P_i^{\text{ex}} = P_i^g(T) - 2\gamma/r_i \quad , \tag{A.1.1}$$

where γ is the effective surface tension and

$$P_i^g(T) = f\left(r_i, n_i\right) T \quad , \tag{A.1.2}$$

is the gas pressure within the bubble at temperature T. Equation (A.1.2) represents any general gas law where the internal gas pressure is linearly dependent on temperature (ideal gas behavior, van der Waals, etc.); $f\left(r_i, n_i\right)$ is, in general, a function of the bubble radius and the number n_i, of gas atom/bubble. The term P_i^{ex} is a measure of the resultant pressure transmitted to the matrix, which vanishes under the initial equilibrium conditions. In Eq. (A.1.1), the effect of external stresses has been neglected. Consider a time interval, Δt (s), of the transient during which the fuel temperatures are increasing at a rate $\mathrm{d}T/\mathrm{d}t$ (° C· s^{-1}). During this time interval,

$$T = T_1 + \frac{\mathrm{d}T}{\mathrm{d}t}\Delta t \quad , \tag{A.1.3}$$

where T_1 is the fuel temperature at the beginning of the time interval Δt, and

$$P_i^g(T_1) = f\left(r_i, n_i\right) T_1 \quad . \tag{A.1.4}$$

First consider the case where the bubble radius r_i is constant over the time interval Δt. The time τ_i^y required for the bubble to acquire an excess pressure sufficient to generate an equivalent stress equal to the yield stress σ_y of the surrounding matrix is, using Eqs. (A.1.1) through (A.1.4), given by

$$\tau_i^y = \frac{\sigma_y r_i T_1}{3\gamma\left(\mathrm{d}T/\mathrm{d}t\right)} \quad . \tag{A.1.5}$$

Equation (A.1.5) does not take into account the situation in which the bubble may be overpressurized prior to the beginning of the time interval Δt. If the bubble was initially in an overpressurized state, then Eq. (A.1.5) would overestimate the time required for the equivalent stress generated by the overpressurized bubble to become equal to σ_y. On the other hand, if appreciable bubble relaxation occurred during time τ_i^y (i.e., r_i increases), then Eq. (A.1.5) would underestimate the time required for the equivalent stress generated by the overpressurized bubble to become equal to σ_y.

A rigorous approach to the calculation of the excess internal gas pressure for each bubble of radius r_i, where i varies over the limits of the bubble size distribution, requires the numerical solution of a large set of coupled partial differential equations for the rate of change of bubble radii and the rate of change of the lattice vacancy concentration c_v. Because of code running time requirements, this approach is outside the scope of most analytical codes. However, a phenomenological approach to the problem of bubble overpressurization can be formulated by evaluating τ_i^y as given by Eq. (A.1.5) with respect to the bubble relaxation time, τ_i^B.

Let α_i ($0 \leq \alpha_i \leq 1$) characterize the degree of nonequilibrium in the lattice surrounding a bubble of radius r_i; the larger α_i, the farther the system is from an equilibrium configuration. The change in α_i can be written in terms of α_i and times τ_i^y and τ_i^B as

$$\mathrm{d}\alpha_i = (1 - \alpha_i)\, \mathrm{d}\left(\tau_i^B / \tau_i^y\right) \quad . \tag{A.1.6}$$

Thus, as τ_i^y decreases and τ_i^B increases, the system departs further from its equilibrium configuration. Conversely, as τ_i^y increases and τ_i^B decreases, the system approaches equilibrium. Solving Eq. (A.1.6) for α_i gives

$$\alpha_i = 1.0 - \exp\left[-\tau_i^B / \tau_i^y\right] \quad . \tag{A.1.7}$$

The bubble relaxation time τ_i^B in Eq. (A.1.7) is given by

$$\tau_i^B(t) = \frac{r_i^2}{C_v^e D_v} \quad , \tag{A.1.8}$$

where C_v^e is the fractional equilibrium vacancy concentration, given by

$$C_v^e = \exp\left[-E_v^f / kT\right] \quad , \tag{A.1.9}$$

and D_v is the vacancy diffusion coefficient, given by

$$D_v = D_v^0 \exp\left[-E_v^m/kT\right] \quad , \tag{A.1.10}$$

E_v^f and E_v^m are the vacancy formation and migration energies, respectively, and D_v^0 is a preexponential factor.

The problem that remains is to relate α_i to the bubble diffusivity. This can be accomplished by considering the limits of the bubble diffusivities used in *FASTGRASS* , for example. During steady-state conditions (i.e., $\alpha_i \ll 1$), empirical intragranular diffusivities are given by[11]

$$D_i^1 = 2.1 \times 10^{-4} \exp\left[-91,000/kT\right] \left(r_1/r_i\right)^{1.62} \ \mathrm{cm}^2 \cdot \mathrm{s}^{-1} \quad . \tag{A.1.11}$$

Equation (A.1.11) is limited by constraints of compatibility with theoretical treatments of bubble mobility by surface diffusion. The diffusivity of a bubble moving by surface diffusion is given by[11]

$$D_i^S = 2.42 \times 10^{-25} \exp\left[-108,000/kT\right] / r_i^4 \ \mathrm{cm}^2 \cdot \mathrm{s}^{-1} \quad . \tag{A.1.12}$$

Based on the discussions above, the bubble diffusivities during transient heating conditions should be given by Eq. (A.1.12) as $\alpha \rightarrow 1$. Thus, using Eqs. (A.1.11) and (A.1.12), the fission gas bubble diffusivities can be expressed in terms of the equilibrium parameter, α_i, as

$$D_i = \frac{4.9202 \times 10^{-11} \exp\left[-\left(91,000 + 17,000\alpha_i\right)/kT\right]}{\left(3365.51 r_i\right)^{1.62+2.38\alpha_i}} \ \mathrm{cm}^2 \cdot \mathrm{s}^{-1} \quad , \tag{A.1.13}$$

where r_1 of Eq. (A.1.11) is the radius of a gas atom (0.24×10^{-7} cm). The form of Eq. (A.1.13) was chosen to make $\log D_i$ a linear function of α_i, i.e., $\log D_i = \log D_i^1 + \left(\log D_i^s - \log D_i^1\right) \alpha_i$.

When $\alpha_i \rightarrow 0$, Eq. (A.1.13) approaches Eq. (A.1.11) for bubble diffusivities based on the isothermal results of Cornell[67] and Gulden[95]. When $\alpha_i \rightarrow 0$, Eq. (A.1.13) approaches Eq. (A.1.12) for bubble diffusivities based on the theory of surface diffusion. For intermediate values of α_i, Eq. (A.1.13) lies between those values given by the empirical expression (as a lower limit) and those obtained from the theory of surface diffusion (as an upper limit).

Equation (A.13) is unique in the sense that it relates the bubble diffusivities to the fuel yield stress, heating rate, and vacancy mobility, as well as to fuel temperature and bubble radius.

To use Eq. (A.1.13), the UO_2 yield stress, σ_y, in Eq. (A.1.5) must be determined. In general, σ_y is a complex function of fuel temperature, strain rate, and microstructure (e.g., UO_2 grain size). Experiments designed to measure the UO_2 yield stress under steady-state and transient in-reactor conditions are difficult to perform and adequate data are lacking. The UO_2 yield stress used in the calculation of gas bubble diffusivities, as given by Eq. (A.1.13), has been determined based on the data of Roberts[96]. Roberts conducted conventional load versus deflection, strain rate change, and stress relaxation tests on UO_2 –20 wt% PuO_2 specimens in the strain rate range from 0.1 to 0.4 h^{-1} and in the temperature range from 1500 to $1800°C$. The specimens, prepared from mechanically blended powders with grain sizes ranging from 2 to 14.5 μm, were deformed in four-point bending in a high temperature, inert-atmosphere furnace. The most significant observations from these experiments are the strong temperature dependence of the flow stress (flow stress decreases as the temperature increases) and the increase in flow stress with an increase in grain size (in these experiments, the flow stress corresponds to the proportional elastic limit stress).

An analytical expression for the yield stress as a function of the temperature and grain size was obtained from Roberts' data by quadratic regression analysis. Explicitly, for σ_y (in dyn $\cdot$ cm^2),

$$\sigma_y = 9.8 \times 10^5 \exp\left[\alpha_0 + \alpha_1/T + \alpha_2/T\right] \quad , \tag{A.1.14}$$

where

$$\alpha_0 = -57.364866 - 7.0264656d + 0.52281105d^2$$

$$\alpha_l = 1.9840863 \times 10^5 + 2.9969484 \times 10^4 d - 2.07175 \times 10^3 d^2$$

$$\alpha_2 = -1.4947535 \times 10^8 - 3.0994649 \times 10^7 d + 2.0330226 \times 10^6 d^2 \quad .$$

Equation (A.1.14) is assumed valid for temperatures between 1500 and $1800°C$ and for grain sizes d between 2.0 and 14.5 μm. No further change in the ratio τ_i^B/τ_i^y of Eq. (A.1.7) was assumed (all other parameters remaining fixed) for temperatures $< 1500°C$ or $> 1800°C$.

Appendix B

Example of a calculated materials property

Often, the most significant impediment to accurate modeling systems is the unavailability of experimentally derived materials property values. Due to the nature of observations for irradiated nuclear fuel, it can prove very difficult to set up experiments to derive the necessary properties. In cases such as this, analytical and first principle methods can be used to extract properties. To ensure these properties provide a realistic approximation, the underlying models are rigorously validated against representative data.

In the section below, Rest[97] proposes a model relating the excess entropy of an amorphous fuel and the viscosity of the material to derive the viscosity of various fuels. This model exemplifies how an analytical model, drawing from a well grounded physical understanding of a system, can be used to calculate important properties that are otherwise unavailable.

The model presented is a summary of the actual work, the entirety of which, including the derivations and solutions to the model, have been submitted at the time of this publication (see Ref. [97]).

B.1 A generalized hard-sphere model for the viscosity of binary alloys that undergo an irradiation induced crystalline-amorphous transformation

A large number and variety of compounds and alloys have been found to become amorphous when exposed to various types of irradiation[39]. For nuclear fuels, the primary damage to the crystal structure is due to the highly energetic fission fragments. Amorphization is a low temperature phenomenon and amorphized materials recrystallize at the so called glass transition temperature. Above this temperature, amorphization is not possible and the fuel exhibits crystalline irradiation behavior. Fuel behavior can be quite different in amorphized fuels. Diffraction studies have revealed that both U_3Si[98] and U_3Si_2[83] become amorphous almost instantly under irradiation. Figure B.1a shows the fission gas bubble morphology in irradiated U_3Si[39]. This fuel developed very large bubbles that led to unacceptable breakaway swelling. The extremely high growth rate of fission gas bubbles in U_3Si was attributed to fission-induced amorphization[23]. Such a transformation resulted in changes in fission gas mobility and the plastic flow rate of the fuel that were responsible for the swelling increases.

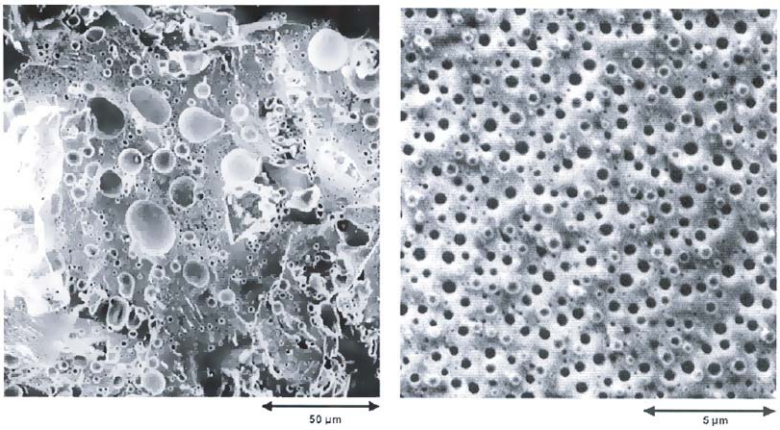

Figure B.1: Fission gas morphology in (a) U_3Si (73% burn-up, 4.3×10^{21} f/cm^3) and (b) U_3Si_2 (96% burn-up, 5.2×10^{21} f/cm^3).

Post-irradiation hardness tests showed that this fuel had retained its relatively hard and brittle pre-irradiation property. The observed fluid-like behavior thus only exists during irradiation. Klaumunzer[99] has demonstrated this irradiation behavior with heavy ion beam irradiations of borosilicate glasses and Pd-Si metallic glasses. He was able to correlate the measured increase in fluidity in these tests with the excess free volume that was independently measured on

these glasses. Work on quenched metallic glasses has shown that the viscosity during annealing tests can be described by the Doolittle equation[100]

$$\eta = \eta_0 \exp\left[C/\Delta V_R\right] \quad , \tag{B.1.1}$$

where C is a constant and ΔV_R is the part of the quenched-in free volume associated with structural relaxation that is recovered during the annealing of the glass prior to recrystallization.

As shown in Fig. B.1b, this extreme behavior was not observed in the lower density compound U_3Si_2, where a distribution of relatively small and stable fission gas bubbles was observed to form and remain throughout the irradiation to very high burn-up[93]. A model developed by Rest to interpret the behavior of fission gas in irradiated amorphous materials such as U_3Si and U_3Si_2 demonstrated that the bubble coarsening process would depend on the materials viscosity and on irradiation-induced re-solution[91]. Figure B.2 shows the estimated viscosity made by comparing the calculated bubble distributions with measured quantities (e.g. from Figs. B.1a and B.1b). Figure B.2 clearly shows that the viscosity of a U-Si compound (derived with the model) is a strong function of the materials composition. Thus, in order to utilize such models in a quantitative fashion, an estimate of the materials viscosity as a function of composition is required. The Adam-Gibbs relation[101] states that the value of the viscosity η is given by

$$\eta = \eta_0 \exp\left[Q/TS_c\right] \quad , \tag{B.1.2}$$

where S_c is the configurational entropy and T the absolute temperature. Equations (B.1.1) and (B.1.2) show that $S_c \approx \Delta V_R/T$. This problem is investigated by considering the entropy of mixing of solid alloys using a generalized hard sphere model of binary fluids in an application to alloys that undergo an irradiation-induced crystalline-amorphous transformation. The basic assumption here is that the behavior of certain irradiated amorphous materials is "liquid like". This model, in simple form, views each alloy component, before mixing, as a collection of hard spheres of suitable diameter; then, on mixing, the hard sphere diameters are adjusted such that the mean volume per atom of the alloy is recovered.

The connection between a real liquid metal and a hard sphere liquid is provided by the attractive forces of the real particles which give rise to cohesion of the real liquid. A generalization of the model due to such attractive forces can be obtained by adding the effect of a uniform negative background potential to the hard sphere model. This generalized hard sphere model was applied to

the U-Si, U-Al, and Al-Si systems. The key assumption in the application of the hard sphere model to the U-Si, U-Al, and Al-Si alloy systems is that the alloys, which undergo irradiation-induced amorphization at low temperatures, is behaving similarly to that of a liquid with similar composition at significantly higher temperatures.

The entropy of mixing of U-Si, U-Al and Al-Si alloys using a generalized hard sphere model of binary fluids was considered in an application to alloys that undergo an irradiation-induced crystalline-amorphous transformation at temperatures significantly below the melting temperature. The model is used to calculate the viscosity of the alloy as a function of composition.

The calculated viscosity as a function of composition for the U-Si system at 400 K is shown in Fig. B.2. For appropriate values of η_0 and A, the calculated excess entropy combined with Eq. (B.1.2) yields viscosity values that are in qualitative agreement with the estimates also shown in Fig. B.2.

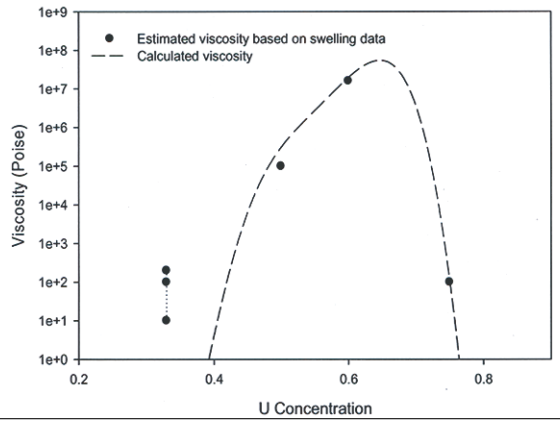

Figure B.2: Calculated viscosity for the U-Si system.

Bibliography

[1] D. R. Olander, *Fundamental Aspects of Nuclear Reactor Fuel Elements* (Energy Research and Development Administration, TID-26711-P1, 1976).

[2] J. R. Matthews and M. H. Wood, Nucl. Eng. Des. **56**, 439 (1980).

[3] J. Rest, J. Nucl. Mater. **321**, 305 (2003).

[4] J. Rest, Nucl. Technol. **61**, 33 (1983).

[5] J. Rest, J. Nucl. Mater. **120**, 195 (1984).

[6] A. A. Solomon, A. Casagrowda, and J. Rest, J. Nucl. Mater. **154**, 332 (1988).

[7] J. Rest, *GRASS-SST: A Comprehensive Mechanistic Model for the Prediction of Fission-Gas Behavior in UO_2-Base Fuels During Steady-State and Transient Conditions*, *NUREG/CR-0202, ANL-78-53* (Argonne National Laboratory Report, Argonne, IL, 1978).

[8] H. Matzke, Radiat. Eff. **53**, 219 (1980).

[9] M. O. Marlowe and A. I. Kaznoff, Nuclear Fuel Performance, *in: Proc. Int. Conf. British Nucl. Soc*, London, 1973.

[10] J. Spino, K. Vennix, and M. Coquerelle, J. Nucl. Mater. **231**, 179 (1996).

[11] J. Rest, Nucl. Technol. **56**, 553 (1982).

[12] J. Rest, NUREG/CR-0202, ANL-78-53, Argonne National Laboratory, 1973.

[13] P. Nikolopoulos, S. Nazare, and F. Thümmler, J. Nucl. Mater. **71**, 89 (1977).

[14] J. Spino, J. Rest, W. Goll, and C. T. Walker, J. Nucl. Mater. **346**, 131 (2005).

[15] F. Anseling, USAEC Report GEAP-5583, General Electric Company, 1969.

[16] J. A. Turnbull, J. Nucl. Mater. **38**, 203 (1971).

[17] J. Rest, J. Nucl. Mater. **150**, 203 (1987).

[18] J. Rest, J. Nucl. Mater. **168**, 243 (1989).

[19] C. Ronchi, J. Nucl. Mater. **96**, 314 (1981).

[20] M. V. Speight, Nucl. Sci. Eng. **37**, 180 (1969).

[21] M. H. Wood and K. L. Kear, J. Nucl. Mater. **118**, 320 (1983).

[22] N. Nakae, T. Kirihara, and S. Nasu, J. Nucl. Mater. **74**, 1 (1978).

[23] J. R. et al., in *Effects of Radiation on Materials*, edited by N. H. Packan, R. E. Stoller, and A. Kumar (American Society for Testing and Materials, Philadelphia, 1990), p. 789, 14th International Symp. (Vol. II), ASTM STP 1046.

[24] J. Rest and G. L. Hofman, in *Proceedings of the Materials Research Society Meeting* (Symposium R, Boston, MA, 2000).

[25] J. Rest, J. Nucl. Mater. **326**, 175 (2004).

[26] J. Rest and G. L. Hofman, J. Nucl. Mater. **277**, 231 (2000).

[27] N. Hanson and D. Kuhlmann-Wilsdorf, Mater. Sci. Eng. **81**, 141 (1986).

[28] H. Zimmerman, in *Proc. Workshop on Fission Gas Behavior in Nuclear Fuels* (European Institute for Transuranium Elements, Karlsruhe, Germany, 1978), p. 127.

[29] J. A. Turnbull and C. A. Friskney, J. Nucl. Mater. **58**, 331 (1975).

[30] S. M. Gehl, *NUREG/CR-2777, ANL-80-108* (Argonne National Laboratory, Argonne, IL, 1982).

[31] C. C. Dollins and F. A. Nichols, J. Nucl. Mater. **66**, 143 (1977).

[32] H. Zimmerman, private communication, 1983.

[33] J. Rest, M. C. Billone, and V. Z. Jankus, *LIFE Code, ANL-76-121* (Argonne National Laboratory, Argonne, IL, 1978), p. 50.

[34] A. Mendelson, *Plasticity: Theory and Application* (MacMillan, New York, NY, 1968), chap. 8.

[35] J. W. Blake, Master's thesis, Northwestern University, Department of Mechanical Engineering, 1984.

[36] J. Rest and G. L. Hofman, Nucl. Technol. **126**, 88 (1999).

[37] G. L. Hofman, Nucl. Technol. **77**, 110 (1987).

[38] J. Rest and G. L. Hofman, J. Nucl. Mater. **210**, 187 (1994).

[39] G. L. Hofman and Y. S. Kim, Nucl. Eng. Tech. **37**, 299 (2005).

[40] L. K. Mansur and W. A. Coghlan, J. Nucl. Mater. **150**, 203 (1987).

[41] J. Rest, unpublished work, Argonne National Laboratory, 1991.

[42] P. B. Kruger and R. M. Mayer, Comput. Phys. Commun. **18**, (1979).

[43] J. Rest and S. A. Zawadzki, NUREG/CR-5840, ANL-92/3, Argonne National Laboratory, 1992.

[44] S. M. Murphy, J. Nucl. Mater. **168**, 312 (1989).

[45] J. Rest, J. Nucl. Mater. **207**, 192 (1993).

[46] N. Q. Lam, S. J. Rothman, and R. Sizmann, Radiat. Eff. **23**, 53 (1974).

[47] M. C. Billone, unpublished work, Argonne National Laboratory, 1991.

[48] R. G. Pahl, D. L. Porter, C. E. Lahm, and G. L. Hofman, Metall. Trans. **21A**, 1863 (1990).

[49] P. R. Okamoto, L. E. Rehn, J. Pearson, R. Bhadra, and M. Grimsditch, in: *Procedures of Materials Research Society Meeting*, Vol. 100, Boston, MA, Nov. 1987, pp. 51-56.

[50] M. Grimsditch, K. E. Coray, R. Bhadra, R. T. Kampwirth, and L. E. Rehn, Phys. Rev. Lett. **B35**, 883 (1987).

[51] P. R. Okamoto, L. E. Rehn, J. Pearson, R. Bhadra, and M. Grimsditch, J. Less Common Met. **140**, 231 (1988).

[52] E. M. Schulson, J. Nucl. Mater. **83**, 239 (1979).

[53] H. Hahn, R. S. Averback, and S. Rothman, Phys. Rev. Lett. **B33**, 8825 (1986).

[54] T. D. de la Ruban, R. S. Averback, R. Benedek, and W. E. Kins, Phys. Rev. Lett. **59**, 1930 (1987).

[55] C. P. Flynn, Phys. Rev. Lett. **171**, 682 (1960).

[56] S. Klaümunzer, G. Schumacher, S. Rentzsch, and G. Vogel, Acta Metallurgica **30**, 1493 (1987).

[57] S. Klaümunzer and G. Schumacher, Phy. Rev. Lett. **51**, 1987 (1983).

[58] S. Klaümunzer, G. Schumacher, M. D. Hou, and G. Vogel, in *Rapidly Quenched Materials*, edited by S. Steeb and H. Warlimont (North Holland, New York, NY, 1987).

[59] S. M. Gehl, M. G. Seitz, and J. Rest, *NUREG/CR-0088, ANL-77-80* (Argonne National Laboratory, Argonne, IL, 1978).

[60] R. J. DiMelfi and L. W. Deitrich, Nucl. Technol. **43**, 328 (1979), see also ANL/RAS-78-32, (Argonne National Laboratory, Argonne, IL, 1978).

[61] R. J. DiMelfi, *Effect of Grain-Boundary Fission Gas Bubbles on Fuel Behavior During Transients*, *ANL-RDP-82* (Argonne National Laboratory Report, Argonne, IL, 1969), p. 2.67.

[62] J. Rest and C. E. Johnson, *A Prediction of TMI-2 Core Temperatures from the Fission Product Release History, NSAIC-12*, Nuclear Saftey Analysis Center of the Electric Power Research Institute (1980).

[63] M. V. Speight and G. W. Greenwood, Phil. Mag. **9**, 683 (1964).

[64] J. Rest and S. M. Gehl, Nucl. Engrg. Des. **56**, 233 (1980).

[65] D. A. MacInnes and I. R. Brearly, J. Nucl. Mater. **107**, 123 (1982).

[66] C. R. A. Catlow and R. A. Jackson, in: *Proc. of the Int. Specialist Mtg. on Fission Gas Behavior in Safety Experiments*, Cardache, France, 1983.

[67] R. M. Cornell, Philos. Mag. **19**, 539 (1969).

[68] H. Matzke, in: *Harwell Consultants Symposium on Inert (Rare) Gases in Metals and Ionic Solids*, UKAEA Research Report AERE R-9733, Vol. 2 (1980) p. 345.

[69] R. A. Lorenz, J. L. Collins, A. P. Malinauskas, O. L. Kirkland, and R. L. Towns, NUREG/CR-0722, (Feb. 1980).

[70] R. A. Lorenz, J. L. Collins, A. P. Malinauskas, M. F. Osborne, and R. L. Towns, NUREG/CR-1386, (Nov. 1980).

[71] M. F. Osborne, R. A. Lorenz, J. R. Travis, and C. S. Webster, NUREG/CR-2928, (Dec. 1982).

[72] S. M. Gehl, in: *Proc. ANS Topical Mtg. on Reactor Safety Aspects of Fuel Behavior*, Aug. 2-6, 1981, Sun Valley ID (American Nuclear Society, LaGrange Park, IL, 1981) Vol. 2, p. 2-354.

[73] S. W. Tam, P. E. Blackburn, and C. E. Johnson, in: *Proc. Int. Mtg. on Thermal Nuclear Reactor Safety*, Chicago, IL, Aug. 29 - Sept. 2, 1982, pp. 101-110.

[74] H. Kleyklamp, J. Nucl. Mater. **131**, 221 (1985).

[75] P. Hofman and J. Spino, J. Nucl. Mater. **127**, 205 (1985).

[76] American Nuclear Society, Report of the Special Committee on Source Terms (September 1984).

[77] P. E. Blackburn and C. E. Johnson, Light water fission data assessment, ANL-82-42, 1982.

[78] A. W. Cronenberg and D. J. Osetek, J. Nucl. Mater. **149**, 252 (1987).

[79] A. W. Cronenberg and D. J. Osetek, in: *American Chemical Society Severe Accident Chemistry Symp.*, Anaheim, CA, Sept. 8 - 12, 1986.

[80] A. D. Appelhans and J. A. Turnbull, NUREG/CR-2298, U.S. Nuclear Regulatory Commission, (1981).

[81] J. A. Turnbull and C. A. Friskney, J. Nucl. Mater. **79**, 184 (1979).

[82] M. O. Tucker and R. J. White, J. Nucl. Mater. **98**, 157 (1981).

[83] R. C. Birtcher, J. W. Richardson, and M. H. Mueller, J. Nucl. Mater. **230**, 158 (1996).

[84] R. Birtcher and J. W. Richardson, Argonne National Laboratory, private communication, 1996.

[85] A. Barbu, M. Bibole, R. L. H. an S. Bouffard, and J. Ramillon, J. Nucl. Mater. **165**, 217 (1989).

[86] S. Klaümunzer, C. Li, and G. Schumacher, Appl. Phys. Lett. **51**, 97 (1987).

[87] A. S. Argon, Acta metal. **27**, 47 (1979).

[88] A. H. Cottrell, *The Mechanical Properties of Matter* (John Wiley, New York, NY, 1964).

[89] X. Chen, R. Birtcher, and S. E. Donnelly, Mater. Res. Symp. Proc. **540**, 331 (1999), (figure replicated with permission of the authors).

[90] H. V. Swygenhoven, L. M. Stals, and G. Knuyt, J. Nucl. Mater. **118**, 125 (1983).

[91] J. Rest, J. Nucl. Mater. **325**, 107 (2004).

[92] H. Matzke, J. Nucl. Mater. **189**, 141 (1992).

[93] J. Rest, J. Nucl. Mater. **325**, 107 (2004).

[94] L. E. Willertz and P. G. Shewmon, Met. Trans. **1**, 2217 (1970).

[95] M. E. Gulden, J. Nucl. Mater. **23**, 30 (1967).

[96] J. T. A. Roberts, in: *Symp. Plastic Deformation of Ceramics*, Pennsylvania State University, 1974.

[97] J. Rest, "A generalized hard-sphere model for the viscosity of binary alloys that undergo an irradiation induced crystalline-amorphous transformation", submitted to the J. Nucl. Mater. (March, 2007).

[98] R. C. Birtcher, C. W. Allen, L. E. Rehn, and G. L. Hofman, J. Nucl. Mater. **152**, 73 (1988).

[99] S. Klaümunzer, Rad. Effect Defect Solid **110**, 79 (1989).

[100] G. S. Grest and M. H. Cohen, in *Advances in Chemical Physics*, edited by I. Prigogoine and S. A. Price (John Wiley and Sons, New York, NY, 1981), p. 469.

[101] G. Adam and J. H. Gibbs, J. Chem. Phys. **43**, 139 (1965).

Nuclear Engineering Division
Argonne National Laboratory
9700 South Cass Avenue, Bldg. 208
Argonne, IL 60439-4842

www.anl.gov

UChicago ▶ Argonne LLC

A U.S. Department of Energy laboratory
managed by UChicago Argonne, LLC